TECHNISCHE UNIVERSITÄT DRESDEN

MAX-PLANCK-GESELLSCHAFT

Three Aspects of Photoionization in Ultrashort Pulses

DISSERTATION

zur Erlangung des akademischen Grades
Doctor rerum naturalium (Dr. rer. nat.)

vorgelegt
der Fakultät Mathematik und Naturwissenschaften
der Technischen Universität Dresden

von

Sajad Azizi

geboren im Khuzestan, Iran

Max-Planck-Institut für Physik komplexer Systeme

Dresden, October, 2023

Gutacher:

1. Prof. Dr. Jan-Michael Rost
2. Prof. Dr. Roland Ketzmerick
3. Prof. Dr. Agapi Emmanouilidou

Eingereicht am 10.05.2023
Verteidigt am 19.10.2023

To my parents

Declaration / Versicherung

Erklärung:

Hiermit versichere ich daß ich die vorliegende Arbeit ohne unzulässige Hilfe Dritter und ohne Nutzung anderer als der angegebenen Hilfsmittel habe angefertigt. Die aus fremden Quellen direkt oder indirekt ubernommene Gedanken sind als solche kenntlich gemacht. Die Arbeit wurde weder im Inland noch im Ausland in einer ähnlicher Form einer anderen Prüfungsbehörde vorgelegt.

Die Arbeit wurde am Max-Planck-Institut für Physik komplexer Systeme in der Abteilung "Endliche Systeme" angefertigt und von Prof. Dr. Jan-Michael Rost und Prof. Dr. Ulf Saalmann betreut.

Ich erkenne die Promotionsordnung der Fakultät Mathematik und Naturwissenschaften der Technischen Universität Dresden vom 23.02.2011 an.

Datum	Unterschrift

Acknowledgements

First and foremost, I would like to express my heartiest gratitude to Prof. Dr. Jan-Michael Rost for putting his trust in me and giving me the necessary freedom to work the way I wanted, and Prof. Dr. Ulf Saalmann for his invaluable help, encouragement, and all he has taught me. Their insightful remarks, enthusiasm, and broad interests in physics are always inspiring. I appreciate everything I learned from them, which will definitely be with me through my research career.

Without the help from the IT department of our institute, a lot of the calculations presented in this thesis would not have been possible. Anyone in this institute who frequently ran the 'slurmtop' command has probably noticed that I was one of those users, who occupied a lot of the computational resources. Needless to say, various challenges appeared while preparing, and running these calculations. The IT department, and especially Hubert Scherrer–Paulus, always provided help in these situations. Thank you!

A special thank goes to Jonathan Dubois. I can recall that the first time we met, it went back to my first talk in the group seminar, where you asked me a question, and that question triggered our collaboration. I learned many things from you, especially during the Corona lockdown, which we mostly discussed via email. Without you, some parts of this thesis, particularly chapter 4, would not have appeared here. I also owe thanks to Panagiotis Giannakeas for answering my tons of questions about quantum scattering, your office door was always open to me, and you explained every single one of my questions with patience and in detail.

On a more personal note, I want to thank Soumi Dutta, and Aileen Durst for, one after another, having been great office mates. Thanks that all of you were really nice to me even though I was mostly quiet and reticent.

Many of my friends at the institute made my time in Dresden pleasant and memorable so in no particular order, Sid, Juan, Reza, Farhad, Ali, Sara, Benjamin, Hamed, Sebastian, Maryam, and Sajal. A special thanks to Abotaleb Amiri. I'm happy you were around, and it was definitely comforting to get together every now and then.

Finally, I would like to thank my parents and family for their unconditional love and emotional support all these years.

Abstract

With the rapid development of laser technology, it is nowadays possible to produce intense few-cycle pulses for larger wavelengths from microwave to visible range and attosecond pulses for shorter wavelengths from ultraviolet to the X-ray range. When an atom or molecule is irradiated by such intense laser pulses, it can undergo various ionization processes, resulting in an ion plus one or more free electrons. Typically, kinetic-energy spectra for the liberated electrons are measured. A suitable combination of ultrashort pulses with highly accurate delays between them allows for a "detailed look" into fundamental processes.

Apart from well-known processes, like single-photon ionization, i.e., the photoeffect, the short duration may trigger new processes like non-adiabatic photoionization (NAPI) that is driven by fast changes in the pulse envelope. It is interesting to see whether this process is sensitive to ultrashort laser pulse shaping. It will be shown how NAPI can be controlled by means of phase details of the ionizing radiation using ultrashort laser pulse shaping. A catalyzing state, which should be quasi-resonance with respect to the initial state, will be introduced. Such a state allows for coherent control of NAPI by modeling the phase details of the pulse.

Even for strong laser pulses time-dependent perturbation theory might be helpful, in particular, in cases where the laser frequency is large than the electron binding energy. In this case, several ATI peaks occur with the 0th peak, caused by NAPI, being an addition. High-order perturbation thereby helps to understand the dependence on the driving pulses, being it shaped pulses for the 0th peak or strong pulses resulting in interference stabilization for the 1st peak.

A natural question that arises with the availability of ultrashort is the measurement of times in particular of the photoionization time delay upon single-photon ionization. This has been studied mainly for atoms and attributed to the Wigner-Smith scattering time delay. In anisotropic potentials as in molecules, the relation of the two time delays is more involved. We discuss this relation in detail for model potentials.

Kurzfassung

Durch die rasante Entwicklung der Lasertechnologie ist es heute möglich, intensive Pulse mit wenigen Zyklen für größere Wellenlängen vom Mikrowellen- bis zum sichtbaren Bereich und Attosekundenpulse für kürzere Wellenlängen vom Ultraviolett- bis zum Röntgenbereich zu erzeugen. Wird ein Atom oder Molekül mit solch intensiven Laserpulsen bestrahlt, kann es verschiedene Ionisierungsprozesse durchlaufen, bei denen ein Ion und ein oder mehrere freie Elektronen entstehen. Typischerweise werden die kinetischen Energiespektren der freigesetzten Elektronen gemessen. Eine geeignete Kombination ultrakurzer Pulse mit hochpräzisen Verzögerungen zwischen den Pulsen ermöglicht einen "detaillierten Blick" auf grundlegende Prozesse.

Abgesehen von bekannten Prozessen wie der Ein-Photonen-Ionisation, d.h. dem Photoeffekt, kann die kurze Dauer neue Prozesse wie die nicht-adiabatische Photoionisation (NAPI) auslösen, die durch schnelle Änderungen der Pulshülle angetrieben wird. Es ist interessant zu sehen, ob dieser Prozess empfindlich auf die Formung ultrakurzer Laserpulse reagiert. Es wird gezeigt, wie NAPI durch Phasendetails der ionisierenden Strahlung mittels ultrakurzer Laserpulsformung gesteuert werden kann. Es wird ein katalysierender Zustand eingeführt, der in Bezug auf den Ausgangszustand quasi-resonant sein sollte. Ein solcher Zustand ermöglicht die kohärente Kontrolle von NAPI durch Modellierung der Phasendetails des Pulses.

Selbst für starke Laserpulse kann die zeitabhängige Störungstheorie hilfreich sein, insbesondere in Fällen, in denen die Laserfrequenz größer ist als die Bindungsenergie der Elektronen. In diesem Fall treten mehrere ATI-Peaks auf, wobei der nullte Peak, der durch NAPI verursacht wird, eine Ergänzung darstellt. Die Störung hoher Ordnung hilft dabei, die Abhängigkeit von den treibenden Pulsen zu verstehen, seien es geformte Pulse für den nullten Peak oder starke Pulse, die zu einer Stabilisierung der Interferenz für den ersten Peak führen.

Eine natürliche Frage, die sich mit der Verfügbarkeit ultrakurzer Pulse stellt, ist die Messung von Zeiten, insbesondere der Zeitverzögerung der Photoionisation bei der Einzelphotonenionisation. Diese wurde hauptsächlich für Atome untersucht und auf die Wigner-Smith-Streuung zurückgeführt. Bei anisotropen Potentialen wie in Molekülen ist die Beziehung zwischen den beiden Zeitverzögerungen komplizierter. Wir diskutieren diese Beziehung im Detail für Modellpotentiale.

Contents

Abbreviations

TDSE	Time–Dependent Schrödinger Equation
TDPT	Time–Dependent Perturbation Theory
XUV	eXtreme UltraViolet
FWHM	Full Width Half Maximum
NAPI	non–adiabatic Photo–ionization
SVEA	Slowly Varying Envelope Approximation
SAE	Single–Active–Electron
ATI	Above Threshold Ionization
FDM	Finite Difference Method
SFI	Strong Field Ionization
RABBITT	Reconstruction of Attosecond Beating By Interference of Two–photon Transitions
CC	Coherent Control
TOF	Time–Of–Flight
PED	Photoelectron Energy Distribution
JNM	Johnson Numerov Method
KH	Kramers–Henneberger

Common Symbols

$\mathcal{E}_0$	Electric Field Strength
ω	Central Laser Frequency
$\mathcal{A}_0$	Vector Potential Strength ($\mathcal{E}_0/\omega$)
$\mathcal{A}_c$	Critical Vector Potential Strength
I	Laser Intensity
I_c	Critical Laser Intensity
I_0	Ionization Potential
U_p	Pondermotive Energy
ϵ	Laser Polarization
τ	Time Delay
e	Electron Charge
h	Planck's Constant
$\hbar$	$h/2\pi$
μ	Electron Mass
c	Speed of light

Chapter 1

Introduction

"In science one tries to tell people, in such a way as to be understood by everyone, something that no one ever knew before. But in poetry, it's the exact opposite."

– *Paul Dirac*

1.1 Preface

In 2018, Gérard Mourou and Donna Strickland were awarded half of the Nobel Prize in Physics for their groundbreaking work on generating high-intensity, ultra-short optical pulses [1, 2]. The intensity of these pulses is so high that it allows for multi-photon processes [3], with a particular form resulting in above-threshold ionization (ATI) peaks [4, 5]. In recent decades, techniques for generating pulses have been improved that allow for the generation of ultrashort pulses at the extreme-ultraviolet (XUV) by means of high-harmonic generation (HHG) [6].

Another route for ultrashort in XUV is free-electron lasers (FEL) [7, 8]. Short-duration pulse has two implications that are considered in this thesis. (1) In interaction with atoms and molecules, it triggers a new ionization process. (2) It allows for the measurement of duration on this time scale, thereby allowing for the study of electron dynamics in atoms and molecules in real-time [9].

The experimental progress in shaping laser pulses will be an important aspect of the thesis. Tailored laser pulses used in coherent control (CC) schemes have led to the discovery of new phenomena in the coupling of light to matter [10]. These phenomena have been uncovered through the use of shaped laser pulses. Quantum coherent control was not realistic until the early 1990s, when ultrashort pulse shaping techniques became practical, and the coherent control of quantum phenomena finally became a reality [11]. For these pulses, phase manipulation using a seeded FEL is possible [7]. In this thesis, we will use it in a new context.

One of the ionization processes that exclusively rely on short pulses is non-adiabatic photoionization (NAPI) [12, 13]. It occurs if the photoelectron cannot follow the fast change of the pulse envelope. It only depends on the envelope of the short ionization pulse but not on the phase details of the pulse [14]. Therefore, it is difficult to control NAPI in the experiment. In chapter 3, we put emphasis on how to coherently control this process using ultrashort pulse shaping. In section 3.3.2, by shaping the spectrotemporal content of XUV pulses, one can render NAPI to phase details of an ionizing pulse in a resonance condition [15].

One may consider NAPI as the zeroth ATI-peak, which is a low-energy peak right above the threshold. This peak is different from the “traditional” ATI peaks, which will be done with time-dependent perturbation theory (TDPT) [16, 17, 18]. Hereby, it turns out that TDPT is a promising method in the ultrashort regime that shows useful applications. Not only can we utilize the 2nd-order perturbation theory to describe the 0th ATI-peak, a process involving the absorption of one photon followed by the emission of another photon, but we

can also account for the stabilization in single-photon ionization [19, 20]. The onset of the stabilization, one of the most surprising phenomena with strong fields, can be investigated using 3rd-order TDPT which is a destructive interference between the first and third-order.

The most natural application of ultrashort pulses is to measure times, in particular upon single-photon ionization. It is well known from fundamental principles in quantum theory that time is not a direct observable quantity [21, 22]. The study of attosecond photoionization time delays is an active area of research with applications in a wide range of fields, some of which were reviewed by Patel and Michielssen in 2021 [23] and by Kheifets in 2023 [24].

Photoionization time delay of molecules represents a much richer process, as compared to atomic ionization, involving a strong angular dependence due to the anisotropic nature of molecular scattering potentials. However, it has received less attention so far, presumably because of the associated experimental and theoretical complexity. The first fully theoretical study of three-dimensional photoionization delay was made by Hockett *et al.* in 2016 [25] that was mapped in the molecular frame and showed the dependence of the emission delay on the electron kinetic energy, the molecular orientation with respect to the light polarization, and molecular symmetry. The experimental measurement also has been made in the group of Wörner in 2016 for N_2O and H_2O molecules [26].

The Wigner-Smith time delay [27, 28] is a scattering process. In the case of spherical potentials there is a connection between the scattering time delay, Wigner-Smith, and the photoionization time delay, since we have selection rules and channels have well-behaved time delays. This is different in molecular systems with anisotropic potentials. In Chapter 5 we discuss this non-trivial connection between scattering time delay and photoionization time delay in molecular systems.

Time delay is a quantity sensitive to the calculation of bound and continuum states. In this thesis, we perform the renormalized Numerov method [29], which is a very accurate numerical method. By modifying precise boundary conditions in this method, we can calculate time delays with high accuracy.

1.2 Thesis outline

The thesis is structured into six chapters: chapter 1 provides an introduction, in chapter 2 we introduce strong field ionization along with basic concepts and present the non-relativistic time-dependent Schrödinger equation for modeling atoms in laser fields, and in chapter 6, the thesis will be rounded off with a short summary of the findings presented, along with some concluding remarks and an outlook on open questions and potential future work. The

remaining chapters which cover three aspects of photoionization are organized as follows:

- **Chapter 3**
  Non-adiabatic photoionization occurs if the light pulse changes fast as compared to the electronic states it couples to. Its occurrence depends on the envelope of the ionizing pulse. We study this process using ultrashort laser pulse shaping, where we introduce a catalyzing state whose presence renders non-adiabatic ionization sensitive to phase details of the tailored pulses in order to enhance ionization and eventually paves the way for experiments for coherent control of this process.

- **Chapter 4**
  In this chapter, we investigate *time-dependent perturbation theory* in ultrashort pulses, where we develop new applications of this method. For example, using second-order perturbation theory, we provide a formula for non-adiabatic photoionization, which depends on the square of the pulse envelope. Furthermore, third-order perturbation theory is taken into account, in order to study interference stabilization, for which we provide an expression for the critical field strength.

- **Chapter 5**
  Time delay is a hot topic that is discussed and measured primarily for atoms. However, this is more complicated in molecules since it depends on the molecular orientation with respect to light polarization and molecular symmetry. This chapter considers this topic from two perspectives: a scattering theory and a wavepacket approach, in which we discuss the theoretical results of angle and energy-resolved time delays in the photoionization of molecules in this rich attosecond phenomenon.

Throughout this thesis, we used atomic units in short 'a.u.', unless specifically stated otherwise, see Appendix F.

Chapter 2

Fundamental Concepts

2.1 Preface

Strong field physics is a field of physics that studies the behavior of matter and radiation in extremely strong electromagnetic fields [30]. These fields are typically so intense that they cause significant deviations from the behavior of matter and radiation in weak fields. The field of laser-matter interaction is one of the most active areas of research within strong field physics. Laser-matter interaction refers to the interaction between high-intensity laser beams and various types of matter, including gases, solids [31], and plasmas [32]. It has applications in ultrafast science, which involves studying chemical and physical processes that occur on extremely short timescales. This has potential applications in fields such as materials science [33], chemistry [34], and biology [35, 36].

This chapter introduces fundamental concepts in strong field physics, which will be used and referred to throughout the thesis. Furthermore, introductions to the more specialized sub-fields for which new results are presented in chapters 3 to 5 can be found at the start of the respective chapters.

The chapter is structured as follows. In section 2.2, we start a 'journey' from weak field to strong field ionization and introduce the related phenomena. In section 2.3, we review the basic equations used throughout the thesis. In section 2.4, we have an introduction to pulse shaping and the way to shape pulses and provide some pulses that are used in this thesis. Lastly, we conclude this chapter in section 2.5.

2.2 Introduction to strong field ionization

Strong field ionization (SFI) is a physical phenomenon that occurs when an atom or molecule is subjected to an intense electromagnetic field, typically in the form of a laser pulse. Under such conditions, the electric field of the laser can become strong enough to ionize the atom or molecule, stripping one or more electrons from the system. SFI is a crucial process in many areas of physics, such as high harmonic generation, attosecond science, and laser-induced breakdown spectroscopy.

2.2.1 From the photoelectric effect to strong-field ionization

Photoionization is a process in which an atom or molecule absorbs a photon of sufficient energy to remove an electron from the atom or molecule, resulting in the formation of a positively charged ion and a free electron, multiple ionization processes are illustrated in Fig. 2.1.

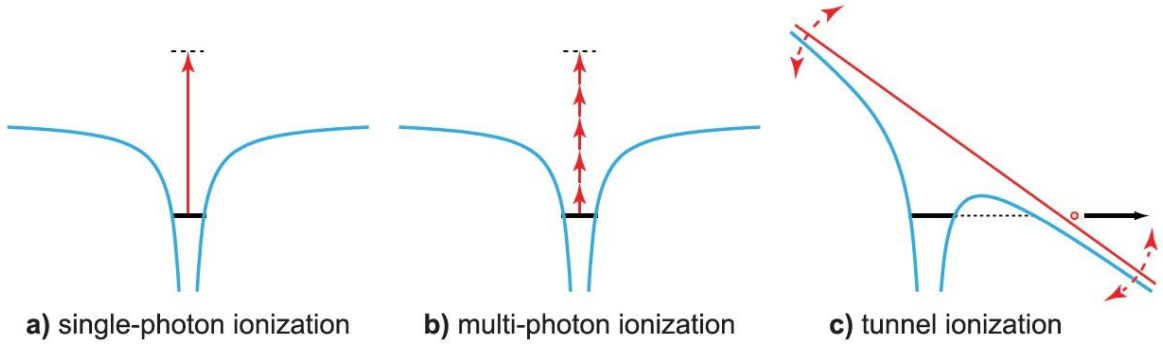

Figure 2.1: Basic ionization processes in atoms, the blue line is the potential, and the black line indicates the ground state energy, where the electron initially is. (a) In single-photon ionization, the atom is ionized through the absorption of a single-photon, the red line implies that one photon energy is sufficient to ionize the electron. (b) If the laser intensity is high enough, multiple photons (red line) can be absorbed simultaneously, leading to ionization even if the individual photons' energy is insufficient. (c) In tunnel ionization, the laser light can be considered as a classical field that is strong enough to bend the Coulomb potential of the atom, such that a tunnel barrier is created, and the electron may tunnel out. The dashed arrow indicates the barrier can oscillate as the field oscillates. The graphic is taken from [37]

.

The most basic ionization process that exists even in the most straightforward bound electronic system, a hydrogen atom, is single-photon ionization, see Fig. 2.1a. A single photon can remove an electron from its initial bound state into the continuum. Single-photon ionization is also the mechanism underlying the photoelectric effect [38].

In 1905, Einstein published [38] his work on the photoelectric effect and the light quantum hypothesis, which gave rise to a reformation in the field of light-matter interaction. The photoelectric effect that Einstein described is marked by the following three features of photoelectric emission [39] (i) For a given atom, there exists a certain minimum frequency of incident radiation below which no photoelectrons can be emitted. (ii) For a given atom and frequency of incident radiation, the rate at which photoelectrons are ejected is proportional to the intensity of the incident light. (iii) Above the threshold frequency, the maximum kinetic energy of the emitted photoelectron is independent of the intensity of the incident light and is described by $E_{kin} = \hbar\omega - I_p$ where I_p is the ionization potential or work function. This framework was able to account for diverse unsolved experimental results of that time.

With the advent of lasers, particularly high-intensity lasers, these "laws" were no longer

applicable and broke down, even though they are still valid for weak lasers. The reason was that Einstein's photoelectric was based on the assumption that a single photon is absorbed. However, as theoretically postulated by Maria Göpper in 1931 [40] and experimentally verified in the 1960s [41, 42], an atom can be ionized by absorbing two photons. With the rise of even more intense lasers, this concept was found to be more general, with multiphoton bridging the energy gap from the binding energy to the continuum, see Fig. 2.1b. Regarding the above-mentioned three features to describe photoionization, these have to be modified, for instance, even below the minimum frequency, multiphoton can provide the energy for the electron release if the intensity of the incident laser is sufficiently high. Moreover, In the perturbation regime, the ionization rate becomes proportional to I^n, where n is the number of absorbed photons and laser intensity I [43]. This can be considered that Einstein's single-photon ionization is a special case with $n = 1$.

The photoelectron spectrum in strong-field ionization becomes more complicated [4, 44] than one might expect and requires more words to fully refine the above features. From the photoelectron spectrum, one can expect the maximum kinetic energy $E_{kin} = n\hbar\omega - I_p$, where n is the minimum number of photons needed to overcome the ionization potential I_p. However, it was observed that far more photons could be observed in the ionization process than are required to overcome the ionization potential. Consequently, photoelectrons can achieve a higher maximal kinetic energy than expected [4]. This effect is known as "above-threshold ionization" (ATI), and it appears as several peaks separated by photon energy $\hbar\omega$ in the photoelectron spectrum and had been seen in experimental observations [5].

Still, there is one observation that does not entirely fit into this picture: as laser intensity, I, increases, peaks at higher energies appear, nonetheless, the lower-order peaks are reduced and finally suppressed [45, 5]. The reason for this peak suppression was later found to be that the energies of the atomic states are stark-shifted in the presence of a laser field [46, 47].

There can be two sorts of stark shifts, AC Stark shift and dynamic Stark shift. Both are related to the interaction between an atom or molecule and an external electromagnetic field. However, there are some differences between them. The AC Stark shift, also known as the Autler-Townes effect [48], is a shift in the energy levels of an atom or molecule that occurs when it is exposed to an intense laser field. The shift is caused by the coupling of different energy levels by the external field, which results in the splitting of the original energy levels into new energy levels. This effect is usually observed when the frequency of the external field is resonant with one of the atomic or molecular transition frequencies [49]. On the other hand, the dynamic Stark shift is a time-dependent shift in the energy levels of an atom or molecule that occurs when it is exposed to a laser field. The laser field can induce transitions between

different energy levels of the atom or molecule, causing shifts in the energies of these levels. The resulting energy shifts are known as the dynamic Stark shifts [50, 51]. In other words, the dynamic Stark shift describes the changes in the energy levels of an atom or molecule in response to a varying electric field.

Back to the observation that does not fit into the picture. The lowest bound states' AC Stark shifts are negligibly small for low laser frequency. On the contrary, the level shift due to the dynamic stark effect of the Rydberg and continuum states are essentially given by the electron ponderomotive energy

$$U_p = \frac{\mathcal{E}_0^2}{4\omega^2}, \tag{2.1}$$

the cycle-averaged kinetic energy of the electron's quiver motion in the laser field [52, 53], where $\mathcal{E}_0$ is the field strength and ω the angular frequency of the laser field. In light of this, the kinetic energy of the photoelectrons is expressed by

$$E_{kin} = n\hbar\omega - I_p - U_p, \tag{2.2}$$

where n is the number of absorbed photons. Yet, the shift of the atomic state was not observed in the early experiments due to the long pulses [45, 47, 54]. In the long pulse regime, the duration of the ionizing radiation is long compared to the time it takes a photoelectron to leave the interaction volume. A photoelectron is produced in an intense field at kinetic energy $E_{kin} = n\hbar\omega - I_p - U_p$. Upon leaving the focus, the ponderomotive energy of the newly created photoelectron in the optical field at the same location is also U_p. Thus for long pulses, the electron converts the ponderomotive energy into kinetic energy as it exits from the interaction volume, just compensating for the decrease in its initial kinetic energy due to the raised ionization potential, and the peaks appeared at $E_{kin} = n\hbar\omega - I_p$. After all, leaving the suppression of the lowest order peaks the only conspicuous feature hinting at the Stark shift. If the pulse duration of the ionizing radiation is short compared to the time for the photoionized electron to escape the interaction volume, there is no time for the photoelectron to accelerate before the pulse leaves [55, 56]. Therefore, only when the pulses became shorter the peaks in the ATI spectrum did shift by U_p.

As for the last point, it is worth mentioning that, although not the focus of this thesis, when the ponderomotive energy U_p is much larger than the ionization potential, ionization occurs by the tunneling mechanism [57], i.e., the electron tunnels through the barrier formed by the atomic potential and the laser electric field, provided that the field is of low frequency [45], see Fig. 2.1c. In this case, the regular structure of ATI peaks disappears [58, 59].

2.3 Non-relativistic time-dependent Hamiltonian

To theoretically describe laser-matter interaction in the non-relativistic regime, we consider the time-dependent Schrödinger equation (TDSE). Note that in this thesis, we utilize the single-active-electron (SAE) approximation, where the core and other electrons are frozen in a system, and instead, an effective potential is engaged. If the system is not subjected to any external field, its field-free Hamiltonian reads [60]

$$\hat{H}_0 = \frac{\hat{\vec{p}}^2}{2\mu} + V(\vec{r}), \tag{2.3}$$

where μ, $\vec{r}$, and $\vec{p}$ are the mass, coordinate, and momentum of electron, respectively. The potential $V(\vec{r})$ can have a spherical or anisotropic form. In the position space $\hat{\vec{p}} = -\mathrm{i}\hbar\vec{\nabla}$, and $\hat{\vec{r}}\,|\vec{r}\rangle = \vec{r}\,|\vec{r}\rangle$, the wavefunctions are given by $\psi(\vec{r}) = \langle\vec{r}|\psi\rangle$. We assume that energy eigenstates $|j\rangle$ of $\hat{H}_0$, which are both bound and continuum states, satisfying the time-independent Schrödinger equation

$$\hat{H}_0\psi_j(\vec{r}) = E_j\psi_j(\vec{r}), \tag{2.4}$$

where $\langle\vec{r}|j\rangle = \psi_j(\vec{r})$.

In the presence of an external field, the Hamiltonian becomes

$$\hat{H}(\vec{r},t) = \frac{1}{2\mu}\left[\hat{\vec{p}} + e\vec{A}(\vec{r},t)\right]^2 - e\Phi(\vec{r},t) + V(\vec{r}), \tag{2.5}$$

where $\vec{A}(\vec{r},t)$ and $\Phi(\vec{r},t)$ are the vector and scalar potential, respectively, of the external field, and $-e$ is the electron charge, e taken to be positive. According to classical electrodynamics, the electric field $\vec{F}(\vec{r},t)$ and the magnetic field $\vec{B}(\vec{r},t)$ can be expressed in terms of a scalar potential $\Phi(\vec{r},t)$ and a vector potential $\vec{A}(\vec{r},t)$ as

$$\begin{aligned} \vec{F}(\vec{r},t) &= -\vec{\nabla}\Phi(\vec{r},t) - \frac{\partial\vec{A}(\vec{r},t)}{\partial t}, \\ \vec{B}(\vec{r},t) &= \vec{\nabla}\times\vec{A}(\vec{r},t), \end{aligned} \tag{2.6}$$

and are invariant under the gauge transformations

$$\begin{aligned} \Phi'(\vec{r},t) &= \Phi(\vec{r},t) - \frac{\partial\chi(\vec{r},t)}{\partial t}, \\ \vec{A}'(\vec{r},t) &= \vec{A}(\vec{r},t) + \vec{\nabla}\chi(\vec{r},t), \end{aligned} \tag{2.7}$$

where χ is an arbitrary function of $\vec{r}$ and t.

2.3.1 Dipole approximation and choice of gauges

At this point, we make a definite choice of gauge, namely the Coulomb (or radiation) gauge, for which $\Phi(\vec{r},t)=0$ and $\vec{A}(\vec{r},t)$ satisfies the transversal condition $\vec{\nabla}\cdot\vec{A}(\vec{r},t)=0$. The vector potential $\vec{A}(\vec{r},t)$ satisfies the following wave equation, which comes from Maxwell's laws

$$\nabla^2\vec{A}(\vec{r},t)-\frac{1}{c^2}\frac{\partial^2\vec{A}(\vec{r},t)}{\partial t^2}=0, \tag{2.8}$$

where c is the light speed. For the description of the laser fields, we may use a vector potential of the form

$$\vec{A}(\vec{r},t)=\hat{\epsilon}\mathcal{A}_0 f(t)\frac{1}{2}\left[\mathrm{e}^{\mathrm{i}\vec{k}\cdot\vec{r}-\mathrm{i}\omega t}+\mathrm{e}^{-\mathrm{i}\vec{k}\cdot\vec{r}+\mathrm{i}\omega t}\right], \tag{2.9}$$

which is the solution of Eq. (2.8). Such a solution describes an $\hat{\epsilon}$ polarized laser pulse propagating, with the wave vector $\vec{k}$ where $|\vec{k}|=\frac{2\pi}{\lambda}$, the carrier frequency ω, the field strength $\mathcal{A}_0$, and the time-dependent envelope $f(t)$. For $|\vec{r}|$ of typical atomic dimensions (a few Ångströms) and λ of typical optical wavelength (a few hundred nanometers), $\vec{k}\cdot\vec{r}\ll 1$ so that over the extent of an atom, the vector potential is spatially uniform, $\vec{A}(\vec{r},t)\backsimeq\vec{A}(t)$. This is the so-called "dipole approximation". This procedure is justified by arguing that the wavelength is considerably larger than the atomic length scale, which holds under usual experimental conditions. As a result, by using the approximation $\mathrm{e}^{\pm\mathrm{i}\vec{k}\cdot\vec{r}}\approx 1$, the vector potential becomes

$$\vec{A}(t)=\hat{\epsilon}\mathcal{A}_0 f(t)\cos(\omega t). \tag{2.10}$$

The magnetic field is then given by

$$\begin{aligned}\vec{F}(t)&=-\frac{\partial\vec{A}(t)}{\partial t},\\ \vec{B}(t)&=0,\end{aligned} \tag{2.11}$$

which implies that any effect induced by the magnetic field in the dipole approximation is neglected. In this approximation, there are several ways to express TDSE

$$\hat{H}(\vec{r},t)\Psi(\vec{r},t)=\mathrm{i}\hbar\frac{\partial\Psi(\vec{r},t)}{\partial t}. \tag{2.12}$$

where the Hamiltonian now in the dipole approximation is given by

$$\hat{H}(\vec{r},t)=\hat{H}_0+\frac{e}{\mu}\vec{A}\cdot\vec{p}+\frac{e^2}{2\mu}\vec{A}^2 \tag{2.13}$$

and $\hat{H}_0$ is defined in Eq. (2.3). We define a unitary operator $\hat{R}$ such that $\Psi'(\vec{r},t)=\hat{R}\Psi(\vec{r},t)$ to simplify the form of the electron-field interaction. Then we have

$$\hat{H}'(\vec{r},t)\Psi'(\vec{r},t)=\mathrm{i}\hbar\frac{\partial\Psi'(\vec{r},t)}{\partial t}, \tag{2.14}$$

where

$$\hat{H}' = \hat{R}\hat{H}\hat{R}^\dagger + \mathrm{i}\hbar\frac{\partial\hat{R}}{\partial t}\hat{R}^\dagger. \tag{2.15}$$

We now choose $\hat{R} = \exp\left(-\mathrm{i}e\chi\left(\vec{r},t\right)\right)$. As a way to eliminate the last term in Eq. (2.13), we may choose $\chi = e/2\mu\int_{-\infty}^{t}\vec{A}^2(t')\mathrm{d}t'$, thus the Hamiltonian in Eq. (2.13) becomes

$$\hat{H}'(\vec{r},t) = \hat{H}_0 + \frac{e}{\mu}\vec{A}(t)\cdot\vec{p}. \tag{2.16}$$

This gauge is also known as the *velocity gauge* because the velocity $\vec{v} = \frac{\vec{p}}{\mu}$ appears in Eq. (2.16). The second important gauge we need to know for the interaction between electrons and electromagnetic fields is the *length gauge* resulting from the transformation $\chi = -\vec{A}\cdot\vec{r}$ thus we get

$$\hat{H}'(\vec{r},t) = \hat{H}_0 + e\vec{F}(t)\cdot\vec{r}, \tag{2.17}$$

where $\hat{H}_0$ is given by Eq. (2.3). The length gauge is only defined within the dipole approximation. If the dipole approximation fails, one needs to be very careful in specifying what exactly means as the length gauge [61]. By definition, all gauges are equivalent in the sense that the results do not depend on the chosen gauge.

The TDSE in the dipole approximation therefore becomes

$$\boxed{\mathrm{i}\hbar\frac{\partial\Psi(\vec{r},t)}{\partial t} = \left(\hat{H}_0 + \hat{V}(t)\right)\Psi(\vec{r},t),} \tag{2.18}$$

where $\hat{V}(t)$ is the interaction potential, which becomes $\hat{V}(t) = \frac{e}{\mu}\vec{A}(t)\cdot\vec{p}$ in velocity gauge and $\hat{V}(t) = e\vec{F}(t)\cdot\vec{r}$ in length gauge. We mostly use the velocity gauge in this thesis because it converges faster [50], though, as a convergence check, we solved the TDSE for some selected cases in the length gauge that obtained essentially identical results. Throughout the thesis, the time-*in*dependent Schrödinger equation (TISE) is solved numerically by employing the Numerov method, see Appendix A.

As a matter of fact, our theoretical studies presented in this thesis are all restricted within the dipole approximation. However, in some situations, it may break down, which leads to non-dipole effects, the interested reader is referred to Refs. [62, 63].

2.3.2 Interaction of an electron with a classical field

Assuming that the vector potential has a form of Eq. (2.10), and this field is turned on at the initial time $t = t_0$, further assume that the initial state of the atom is $|i\rangle$ where $\hat{H}_0|i\rangle = E_i|i\rangle$. We expand the wavepacket $|\Psi(\vec{r},t)\rangle$ in terms of the complete set of uncoupled atomic states $|\psi_j(\vec{r})\rangle$ for times $t > 0$ as

$$|\Psi(\vec{r},t)\rangle = \sum_j a_j(t)\,|\psi_j(\vec{r})\rangle\,, \tag{2.19}$$

where the time-dependent amplitudes, $a_j(t)$, satisfy the normalization condition of $\sum_j |a_j(t)|^2 = 1$. Note that we may consider a "sufficiently large box" in our simulation, then states $|\psi_j(\vec{r})\rangle$ include both bound and continuum.

Substituting Eq. (2.19) into Eq. (2.18) and multiplying from the left by $\langle\psi_k(\vec{r})|$ yields the set of the coupled first-order differential equation for the amplitudes as

$$\dot{a}_k(t) = \frac{\mathrm{i}}{\hbar}\sum_j \left(E_j\delta_{jk} + V_{jk}\right) a_j(t), \tag{2.20}$$

where

$$V_{jk}(t) = \langle j|\,\hat{V}(t)\,|k\rangle = \begin{cases} \langle j|\,\vec{r}\cdot\vec{F}(t)\,|k\rangle & \text{length gauge,} \\ \langle j|\,\vec{p}\cdot\vec{A}(t)\,|k\rangle & \text{velocity gauge.} \end{cases} \tag{2.21}$$

This is the basic set of coupled differential equations that must be solved, subject to the initial condition $a_i(0) = 1$, i.e., only the state $|i\rangle$ being initially populated, in order to obtain the probability of finding $|j\rangle$ as a function of t. Here we define the matrix-element

$$d_{jk} = \begin{cases} \langle j|\,\vec{r}\cdot\vec{\epsilon}|k\rangle & \text{length gauge,} \\ \langle j|\,\vec{p}\cdot\vec{\epsilon}|k\rangle & \text{velocity gauge.} \end{cases} \tag{2.22}$$

Notice that the dipole elements between the two gauges are related through

$$\langle j|\,\vec{p}\,|k\rangle = \mathrm{i}\frac{\mu}{\hbar}\left(E_j - E_k\right)\langle j|\,\vec{r}\,|k\rangle\,, \tag{2.23}$$

where this relation is obtained using $[\hat{H}, \hat{r}] = -\mathrm{i}\frac{\hbar}{\mu}\hat{p}$, this relationship works well when the eigenenergies and eigenstates are accurately calculated.

Equation (2.20) can be solved numerically by using Taylor expansion of the exponential matrix $H_{jk} = E_j\delta_{jk} + V_{jk}$, which is given by

$$a_j(t+\delta t) = \sum_k \left[\mathrm{e}^{-\frac{\mathrm{i}}{\hbar}\mathbf{H}\,\delta t}\right]_{jk} a_k(t) = a_j(t) - \frac{\mathrm{i}\delta t}{\hbar}\sum_k H_{jk}a_k(t) - \frac{(\delta t)^2}{2\hbar^2}\sum_k H_{jk}\sum_l H_{kl}a_l(t) + \ldots \tag{2.24}$$

that is a matrix-vector multiplication, and δt, which is the time step, can be set accordingly. Since the finite Taylor expansion is not unitary, we need $\delta t \to 0$ for the series to converge, i.e., $\sum_j |a_j(t)|^2 = 1$.

Finally, the probability for the electron to make a transition from state $|i\rangle$ to state $|j\rangle$ in time t is given by

$$P_{i\to j}(t) = |a_j(t)|^2. \tag{2.25}$$

The general definition for determining the photoelectron spectrum as $t \to \infty$ is with a delta function. Then, because of numerics and the discretization of the energy, we need a Gaussian

distribution which is given by

$$p(E) = \frac{1}{\sqrt{2\pi\delta E}} \sum_j |a_j(t \to \infty)|^2 \ \exp\left[-\left(\frac{E - E_j}{\delta E}\right)^2\right], \tag{2.26}$$

where δE is a positive and small number in the order of the distance between eigenvalues. Moreover, the ionization probability can be defined as follows

$$P_{\text{ion}} = \int \mathrm{d}E \, p(E), \tag{2.27}$$

where $p(E)$ is the electron spectrum and defined in Eq. (2.26).

The vector potential we have introduced in this section might have different shapes, and in the following, we investigate this pulse shaping.

2.4 Ultrashort laser pulse shaping

Ultrashort pulse shaping is the process of controlling the intensity and phase of ultrashort light pulses to create a specific desired pulse shape [64, 65, 66, 67, 68]. Ultrashort laser pulses can be shaped in a variety of ways to optimize their properties for specific applications, including pulse compression [69], pulse shaping [70], phase control [71], and polarization control [72]. Pulse shaping, which we use in this thesis, involves manipulating the pulse waveform that is typically done by passing the pulses through a spatial light modulator, which is a device that can rapidly change the phase and amplitude of light. This can be used to create specific pulse shapes, such as Gaussian, flat-top, or square pulses, or to tailor the pulse spectrum to a specific application. Pulse shaping is used in many fields, including laser physics, nonlinear optics [73, 74], and spectroscopy [75] to study the dynamics of matter and energy on an ultrashort timescale. In essence, ultrashort pulse shaping is a way of controlling the shape of light pulses that are very short in duration. The ultrashort pulse duration allows access to the real-time motion of the electron at their natural timescale, the attosecond, using pump-probe techniques [70].

We consider the vector potential $\vec{A}(t) = A(t)\vec{\mathrm{e}}_x$ is given by [70]

$$A(t) = \mathrm{Re}\, \underline{A}(t), \tag{2.28}$$

where $\mathrm{Re}\, \underline{A}(t)$ denotes the real part of the complex vector potential. The vector potential can be modified with a proper filter acting in the frequency domain. Thus the pulse is Fourier transformed, filtered, and back-transformed to yield a new pulse which is given by

$$\underline{A}(t) = \mathcal{F}^{-1}\left[\mathcal{F}\left[I(t)\right](\omega')\mathrm{e}^{-\mathrm{i}\varphi(\omega'-\omega)}\right](t), \tag{2.29}$$

where $I(\omega) = \mathcal{F}\left[I(t)\right](\omega)$ is the spectral intensity profile and can have various pulse shapes, see Ref. [76], here, we choose the Gaussian profile, and the filter, $\mathrm{e}^{-\mathrm{i}\varphi(\omega'-\omega)}$, is chosen accordingly. Hence, the complex vector potential is given by

$$\underline{A}(t) = \underline{\mathcal{A}}_0 \mathcal{F}^{-1}\left[\exp\left(-\frac{(\omega'-\omega)^2}{2\Delta\omega^2} - \mathrm{i}\varphi(\omega'-\omega)\right)\right](t) = \mathcal{F}^{-1}\left[\underline{\tilde{A}}(\omega')\right](t), \tag{2.30}$$

where $\underline{\mathcal{A}}_0 = \mathcal{A}_0\mathcal{N}$ ensures the proper amplitude of the vector potential with $\mathcal{N} \equiv T/\sqrt{8\pi \ln 2}$, and $\mathcal{F}^{-1}$ denotes the inverse Fourier transform which is defined in Eq. (2.31). The width of the inverse Fourier transform of the laser pulse is $\Delta\omega' = 2\sqrt{\ln 2}/T$. The frequency of the fast oscillating part of the laser pulse is ω. The laser pulse duration is given by T. These parameters, i.e., T, $\mathcal{A}_0$, and ω, are the fundamental parameters of a general pulse.

The Fourier transform and the inverse Fourier transform of the signals are defined as

$$\begin{aligned}
\mathcal{F}[u(t)](\omega') &= \frac{1}{\sqrt{2\pi}} \int_{-\infty}^{\infty} \mathrm{d}t \ \exp(\mathrm{i}\omega' t) u(t), \\
\mathcal{F}^{-1}[\tilde{u}(\omega')](t) &= \frac{1}{\sqrt{2\pi}} \int_{-\infty}^{\infty} \mathrm{d}\omega' \ \exp(-\mathrm{i}\omega' t) \tilde{u}(\omega').
\end{aligned} \tag{2.31}$$

We choose this formula, Eq. (2.30), for shaping the laser pulse as it has two advantages (i) In the experiment, "arbitrary" pulses are created by modifying only the spectral phase [77], and we can model these pulses by Eq. (2.30), (ii) pulse energy is kept constant. Figure 2.2 shows this process clearly.

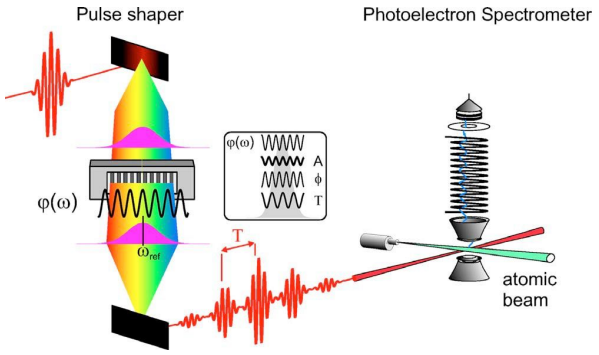

Figure 2.2: Experimental setup for shaping a sinusoidal pulse, see subsection 2.4.2, in which the spectral phase is modified in order to generate an ultrashort pulse as the same in Eq. (2.30). The graph is taken from [77].

The Fourier transform of the vector potential is given by

$$\tilde{A}(\omega') = \mathcal{F}[A(t)](\omega') = \mathcal{F}[\mathrm{Re}\,\mathcal{F}^{-1}[\underline{\tilde{A}}(\omega')](t)](\omega'). \tag{2.32}$$

Since $A(t)$ is purely real, one has $\tilde{A}^*(\omega') = \tilde{A}(-\omega')$. The quantity $\tilde{A}(\omega')$ is real if and only if the imaginary part of $\underline{\tilde{A}}(\omega)$ is odd, i.e., $\mathrm{Im}\,\underline{\tilde{A}}(\omega') = -\,\mathrm{Im}\,\underline{\tilde{A}}(-\omega')$, where Im denotes the imaginary part. Therefore, we can write

$$\tilde{A}(\omega') = \frac{1}{2}\left[\underline{\tilde{A}}(\omega') + \underline{\tilde{A}}^*(-\omega')\right], \tag{2.33}$$

where $\underline{\tilde{A}}(\omega)$ is defined in Eq. (2.30).

In order to define the general vector potential in terms of the pulse envelope, $f(t)$, and phase details of the pulse, $\Phi(t)$, we use the analytic potential defined as

$$A_\mathrm{a}(t) = A(t) + \mathrm{i}\mathcal{H}\left[A(t)\right], \tag{2.34}$$

where $\mathcal{H}$ denotes the Hilbert transform defined as

$$\mathcal{H}\left[u(t)\right] = \frac{1}{\pi}\int_{-\infty}^{\infty} \mathrm{d}\tau\, \frac{u(\tau)}{t-\tau} = \left(\frac{1}{\pi t} * u(t)\right)(t), \tag{2.35}$$

with $\cdot * \cdot$ the convolution product. The analytic vector potential is a complex signal which embeds the main properties of the laser field. Any analytic signal can be written in polar coordinates

$$A_\mathrm{a}(t) = f(t)\exp\left[\mathrm{i}\theta(t)\right], \tag{2.36}$$

where $f(t) = |A_\mathrm{a}(t)|$ is the instantaneous laser envelope, $\theta(t)$ is the instantaneous phase and $\omega(t) = \mathrm{d}\theta(t)/\mathrm{d}t$ is the instantaneous laser frequency. The vector potential of the laser pulse is given by the real part of the analytic vector potential $A(t) = \mathrm{Re}\,A_\mathrm{a}(t)$.

We consider the time-dependent vector potential defined from Eq. (2.30). The Fourier transform of the complex vector potential $\underline{\tilde{A}}(\omega')$ is a function of $\omega' - \omega$. Using the Fourier transform properties of translation, Eq. (2.30) can be written as

$$\underline{A}(t) = \underline{\mathcal{A}}_0 \exp\left(-\mathrm{i}\omega t\right)\mathcal{F}^{-1}\left[\exp\left(-\frac{\omega'^2}{2\Delta\omega'^2} - \mathrm{i}\varphi(\omega')\right)\right](t). \tag{2.37}$$

As a consequence, using $A(t) = \mathrm{Re}\,\underline{A}(t)$, a general expression of the vector potential $A(t)$ is given by

$$\boxed{A(t) = \underline{\mathcal{A}}_0 f(t)\cos\left[\omega t + \Phi(t)\right]}, \tag{2.38}$$

where the instantaneous laser envelope is $f(t)$, the instantaneous phase is $\omega t + \Phi(t)$ and the instantaneous frequency is $\omega + \partial\Phi(t)/\partial t$. The laser envelope and time-dependent term of the instantaneous frequency are given by

$$f(t)\exp\left[i\Phi(t)\right] = \Delta\omega' \exp\left[-\frac{\Delta\omega'^2 t^2}{2}\right] * \mathcal{F}^{-1}\Big[\exp\left[-\mathrm{i}\varphi(\omega')\right]\Big](t). \tag{2.39}$$

We notice that if $\varphi(\omega') = -\varphi(-\omega')$, $(\exp[-\mathrm{i}\varphi(\omega')])^* = \exp[-\mathrm{i}\varphi(-\omega')]$. In this case, i.e., if $\varphi(\omega') = -\varphi(-\omega')$, the inverse Fourier transform of $\exp[-\mathrm{i}\varphi(\omega')]$ is purely real, and as a consequence $\Phi(t) = 0$ or $\Phi(t) = \pi$. In this case, the vector potential reads exactly $A(t) = f(t)\cos(\omega t)$.

Following are some examples of laser pulses that we employ throughout this thesis.

2.4.1 Fourier-limited pulse: Gaussian envelope

For the Fourier-limited pulse, i.e., $\varphi(\omega' - \omega) = \text{const.}$, the time-dependent and Fourier transforms of the vector potential are given by

$$\begin{aligned}
\tilde{\underline{A}}(\omega') &= \underline{\mathcal{A}}_0 \exp\left[-\frac{(\omega'-\omega)^2}{2\Delta\omega'^2}\right], \\
\tilde{A}(\omega') &= \frac{\mathcal{A}_0}{2}\left[\exp\left(-\frac{(\omega'-\omega)^2}{2\Delta\omega'^2}\right) + \exp\left(-\frac{(\omega'+\omega)^2}{2\Delta\omega'^2}\right)\right], \\
\underline{A}(t) &= \mathcal{F}\left[\tilde{A}(\omega')\right](t) = \underline{\mathcal{A}}_0 \Delta\omega' \exp\left[-\frac{\Delta\omega'^2 t^2}{2} - \mathrm{i}\omega t\right].
\end{aligned} \tag{2.40}$$

Therefore the Fourier-limited pulse with a Gaussian envelope is given by

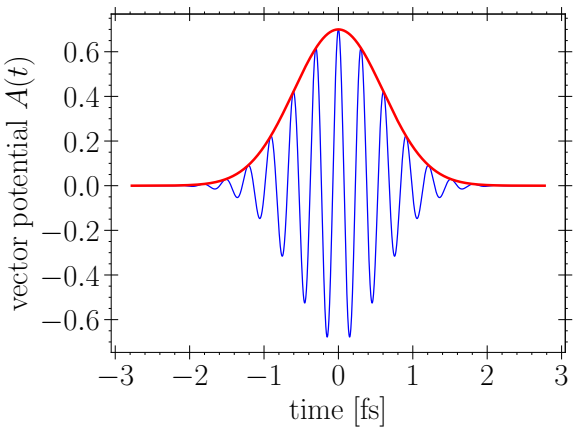

Figure 2.3: An example of a Fourier-limited pulse with the Gaussian envelope for the pulse duration $T = 1$ fs, the carrier frequency $\omega = 0.5$ a.u., and the field strength of $\mathcal{A}_0 = 0.7$ a.u.. The envelope (red line) is obtained using the Hilbert transform in Eq. (2.35).

$$A(t) = \mathcal{A}_0 \exp\left(-2\ln 2 t^2/T^2\right)\cos(\omega t). \tag{2.41}$$

In some cases, the envelope also is expressed as $\exp\left(-t^2/T'^2\right)$, where $T' = T/\sqrt{2\ln 2}$. The duration of the pulse is controlled by T. How strong the intensity of the pulse also is fixed

by the field strength $\mathcal{A}_0$, and the central frequency of the pulse is defined as ω. Figure 2.3 shows a Gaussian shape pulse as an example.

2.4.2 Modulated pulse: sinusoidal phase modulation

A sinusoidal laser pulse is a type of laser pulse whose intensity varies sinusoidally over time. Sinusoidal laser pulses can be created using a technique in which passing a laser pulse through a device that can modulate its intensity with a sinusoidal pattern, see Fig. 2.2. This pulse is routinely investigated in coherent control experiments [78, 79, 80, 77] because the use of sinusoidal laser pulses in coherent control experiments allows for precise control over the properties of the laser pulse, which can lead to the manipulation of quantum systems in a variety of ways, for example, these pulses can be used to generate pulse sequences with specific temporal profiles. These pulse sequences can be used in coherent control experiments to implement various control strategies, such as population transfer.

This pulse can be generated by choosing a modulated pulse with $\varphi(\omega'-\omega) = a\sin[\omega'\tau+\phi]$, the vector potential in the frequency domain is then given by

$$\underline{\tilde{A}}(\omega') = \underline{\mathcal{A}}_0 \exp\left[-\frac{(\omega'-\omega)^2}{2\Delta\omega'^2} - \mathrm{i}a\sin\left[\omega'\tau+\phi\right]\right] \tag{2.42}$$

Fourier transform of the vector potential

$$\underline{A}(t) = \frac{\tilde{A}_0}{2}\mathcal{F}\left[\underline{\tilde{A}}(\omega') + \underline{\tilde{A}}(-\omega')\right] \tag{2.43}$$

Using Eq. (2.39)

$$\begin{aligned}\underline{A}(t) &= \frac{\underline{\mathcal{A}}_0}{2}\mathcal{F}\left[\mathrm{e}^{-[\omega'-\omega]^2\frac{T^2}{8\ln 2}}\right](t) * \mathcal{F}\left[\mathrm{e}^{-\mathrm{i}a\sin(\omega'\tau+\phi)}\right](t) \\ &= \mathcal{A}_0\mathrm{e}^{-2\ln 2\ t^2/T^2}\mathrm{e}^{\mathrm{i}\omega t} * \mathcal{F}\left[\mathrm{e}^{-\mathrm{i}a\sin(\omega'\tau+\phi)}\right](t)\end{aligned} \tag{2.44}$$

Making use of the Jacobi-Anger expansion $\mathrm{e}^{-\mathrm{i}a\sin(\omega'\tau+\phi)} = \sum_{k=-\infty}^{\infty} J_k(a)\mathrm{e}^{-\mathrm{i}k(\omega'\tau+\phi)}$, where $J_k(a)$ describes the Bessel function of the first kind and order k. To obtain its Fourier transform

$$\mathcal{F}\left[\mathrm{e}^{-\mathrm{i}a\sin(\omega'\tau+\phi)}\right](t) = \sum_{k=-\infty}^{\infty} J_k(a)\mathrm{e}^{-\mathrm{i}k\phi}\delta(k\tau-t) \tag{2.45}$$

By means of the convolution integration as $(f*g)(t) = \int_{-\infty}^{\infty} dt' f(t')g(t-t')$, and $\int_{-\infty}^{\infty} dt f(t)\delta(t-a) = f(a)$, we end up with

$$A(t) = \mathcal{A}_0 \sum_{k=-\infty}^{\infty} J_k(a)\ \mathrm{e}^{-2\ln 2\ [t-k\tau]^2/T^2}\cos\Big(\omega[t-k\tau]-k\phi\Big). \tag{2.46}$$

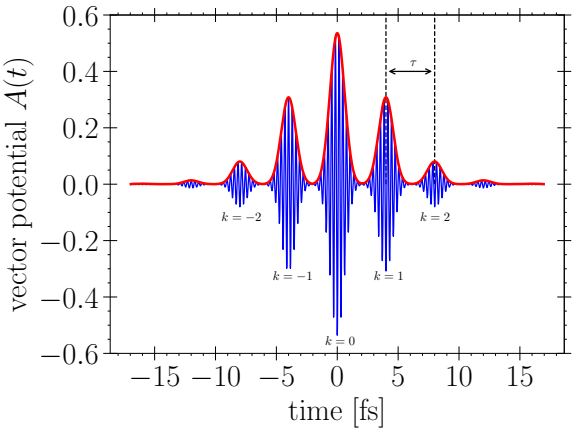

Figure 2.4: An example of the sinusoidal pulse Eq.(2.46) along with its envelope (red line), which obtained using the Hilbert Transform, Eq. (2.35), for the fundamental pulse parameters of Fig. 2.3 and modulated parameters of $a = 1, \tau = 4T, \phi = 0$.

How strongly the original Gaussian pulse is distributed over separate pulses in the train is controlled by a, The amplitude of the phase oscillation in Eq. (2.42). As an example, for $a = 1$, which results in a train with essentially 9 pulses mark in Fig. 2.4, since $J_{k=-4,\cdots,4}(1)$ are only significant in values. The delay between the pulses is fixed by τ. The modulation phase ϕ introduces a difference ϕ in the carrier-envelope phase of adjacent pulse members of the train, as one can see in Eq. (2.46). Figure 2.4 shows a sinusoidal pulse example.

For the limit of $\tau = 0$ we have

$$A(t) = \mathcal{A}_0 \mathrm{e}^{-2\ln 2\ t^2/T^2} \cos(\omega t) \sum_{k=-\infty}^{\infty} J_k(a) \mathrm{e}^{-\mathrm{i}k\phi}, \tag{2.47}$$

using the Jacobi-Anger identity $\mathrm{e}^{-\mathrm{i}a\sin(\phi)} = \sum_{k=-\infty}^{\infty} J_k(a)\mathrm{e}^{-\mathrm{i}k\phi}$, it becomes a Gaussian pulse as

$$A(t) = \mathcal{A}_0 \mathrm{e}^{-2\ln 2\ t^2/T^2} \cos\Big(\omega t + a\sin(\phi)\Big) \tag{2.48}$$

2.5 Summary

To conclude the chapter, we had an introduction to strong filed ionization in which we introduced the related phenomena and the basic formula which is used and referred to throughout the thesis. In addition, the pulse shaping is reviewed and formulated, and we introduced the pulses we used in this thesis, namely, the Gaussian envelope and sinusoidal pulse.

Chapter 3

Controlling Non-adiabatic Photoionization with Ultrashort Pulses

3.1 Preface

In recent years new phenomena in coupling of light to matter have been uncovered through tailored laser fields, where the emphasis has shifted from a typical coherent-control scenario by a shaped laser pulse [81] to two-color pulses and/or different time-dependent polarizations [82, 83, 84]. Coherent control of multi-photon transitions in the optical strong-field regime by shaped pulses has been demonstrated [78, 85] aided by Stark shifts which modify multi-photon processes [86]. Along another thrust, ever shorter pulses with nominal carrier frequencies in the extreme-ultraviolet (XUV) regime have been pursued, either generated by high-harmonic sources [87, 88] or by free-electron lasers [89, 90], which can produce quite intense pulses. For those pulses, phase manipulation is also possible [91]. Surprisingly, using the longitudinal coherence within the waveform of light wave-packets, produced by individual relativistic electrons, it is even possible with synchrotrons to shape pulses on the attosecond time-scale (duration and separation) with XUV carrier frequencies [92].

For the regime of ultra-short intense pulses, non-adiabatic photo-ionization (NAPI) has been demonstrated [12, 13, 14], typically for weakly-bound systems $E_0 \ll \omega$, with the electron's binding energy E_0 and the photon frequency ω. The characteristic of NAPI is a peak of the ionization yield just above the ionization threshold. The physics behind NAPI is a time-scale hierarchy such that the photo-electron cannot follow the fast change of the pulse envelope (therefore non-adiabatic photo-ionization).

In the following, we will investigate if NAPI can be influenced and steered by a tailored pulse form, where we put emphasis on the question how this is possible in the first place, rather than asking and interpreting effects of specifically shaped pulses.

This chapter is organized as follows: In section 3.2, we have an introduction to this process and, with the help of intuitive and mathematical pictures. In section 3.3, NAPI is investigated with tailored laser pulses in which we introduce a catalyzing state, whose presence renders NAPI sensitive to phase-details of tailored pulses. Since a catalyzing state is generally easy to create, this opens a perspective for coherent control of ultra-fast ionization. Finally, we summarize this chapter in section 3.4.

3.2 Introduction to non-adiabatic ionization

Non-adiabatic ionization refers to the process of ionization that occurs when the time scale of the ionizing process is too fast for the electron to follow the motion of the parent ion, and the system undergoes the fast-changing of energy as a function of time. Here we analyze this process in two pictures: intuitive and mathematical pictures.

3.2.1 Intuitive picture

Consider the sketch in Fig. 3.1 as an intuitive picture of this process. Here we have a bound state and continuum states. The thick red line is the electron occupation. There is also a strong field along with its envelope. The strong field causes a Stark shift in that state (the ground state). It implies that the energy of the ground state becomes time-dependent, indicating a rapid change in energy which makes a transition from the ground state to continuum states, called a "non-adiabatic" transition. If the energy of this state changes slowly, the electron will stay in this state adiabatically all the time. The adiabatic

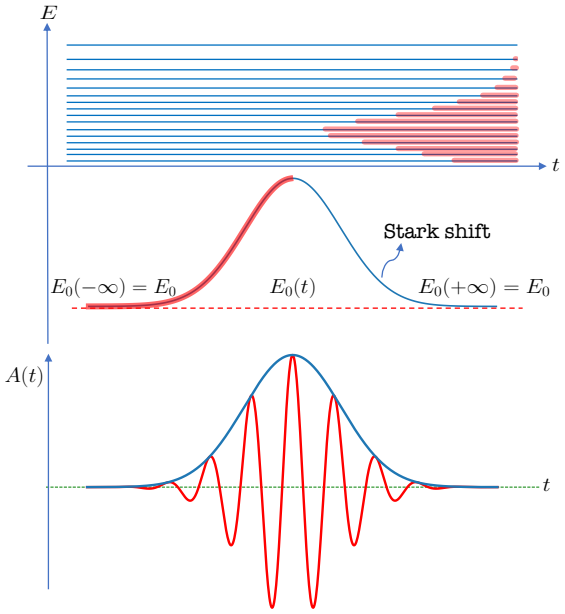

Figure 3.1: Sketch of the intuitive picture of the non-adiabatic transition process

process means that the state changes slowly. One can also have a large Stark shift, but if the state changes slowly, the eigenstate barely changes its character. As a result, if the state's character is slowly changing, it has time to adapt to the new situation and will remain there.

For the high-frequency pulse, the coupling with the higher state is weak (the matrix element is small), and accordingly, the Stark shift is weak, and the ground state is not significantly affected by the variation in time. For that reason, there is no non-adiabatic process. Consequently, there are two probable reasons for no state changes: (i) the field is not strong enough, or (ii) the coupling is not strong enough.

An examination of the mathematical explanation in the Kramers-Henneberger (KH) frame [93, 94] supports this intuitive picture of NAPI.

3.2.2 Mathematical picture

The formation of the KH atom is described in the literature [93, 94, 95]. Following in the footsteps of these works, we consider a one-electron atom with an effective atomic potential $V(\vec{r})$ that is subjected to a linearly polarized laser field $F(t)$. We merge the origin of our reference frame with the atomic electron oscillating in the field. This is accomplished by using the unitary transformation operator $\hat{R} = \exp\left\{\mathrm{i}\int \mathrm{d}t\, \vec{A}(t)\cdot\vec{p}\right\}$ in Eq. (2.15), where $\vec{A}(t)$ is the vector potential defined in Eq. (2.10). By this transformation, we transform the initial velocity gauge Hamiltonian to the so-called *Kramers-Henneberger gauge*, where the Hamiltonian in this frame is given by [13]

$$\hat{H} = \frac{\vec{p}^{\,2}}{2\mu} + V\left(\vec{r} + x_\omega(t)\vec{e}_x\right), \tag{3.1}$$

where x_ω is the classical quiver position in a linearly polarized laser field along x. The laser field in terms of the quiver amplitude $F(t) = -\frac{\mathrm{d}^2 x_\omega}{\mathrm{d}t^2}$ where $x_\omega(t) = f(t)\cos(\omega t)$ and the pulse envelop $f(t) = \alpha_0\, \mathrm{e}^{-4\ln 2 t^2/T^2}$. For the pulse to remain in the non-relativistic domain, it is characterized by the maximum field strength $F(0) = \mathcal{E}_0$, which leads to the prefactor α_0 given by

$$\alpha_0 = \frac{\mathcal{E}_0}{\omega^2}\frac{1}{1 + 8\ln 2/(T\omega)^2}. \tag{3.2}$$

We can construct the Hamiltonian in terms of Fourier components of the oscillating potential as

$$H = \frac{\vec{p}^{\,2}}{2\mu} + \sum_n V_n(\vec{r}, t)\, \mathrm{e}^{\mathrm{i}n\omega t}, \tag{3.3}$$

where $V_n(\vec{r}, t)$ are *single-cycle averaged* Fourier components of the potential in Eq. (3.1) given by

$$V_n(\vec{r}, t) = \int_{t-\frac{\pi}{\omega}}^{t+\frac{\pi}{\omega}} \mathrm{d}t'\; V\left(\vec{r} + f(t)\cos(\omega t')\vec{e}_x\right) \mathrm{e}^{\mathrm{i}n\omega t'}. \tag{3.4}$$

The oscillating potential in Eq. (3.1) consists of two parts of the fast-oscillating field, $\cos(\omega t)$, and the slowly-varying envelope, $f(t)$. Equation (3.4) is an average over the fast-oscillating part.

The expression in Eq. (3.3) becomes useful if we consider a few terms. Here we only focus on the 0th-order term because H_0 is responsible for non-adiabatic transition and changes with the envelope. The 0th-order term is provided by

$$H_0(t) = -\frac{\hbar^2}{2\mu}\nabla^2 + V_0(\vec{r}, t), \tag{3.5}$$

where $V_0(\vec{r}, t)$ is the *cycle-averaged* potential.

Figure 3.2 is depicted to understand the cycle-averaged potential. It shows an envelope and the cycle-averaged potential for different times marked on the envelope. Since the potential changes in time, the instantaneous ground state does as well, which may imply changes in shape and corresponding energy. The latter may be interpreted as a Stark shift. We performed the imaginary time propagation method to obtain the time-dependent ground state.

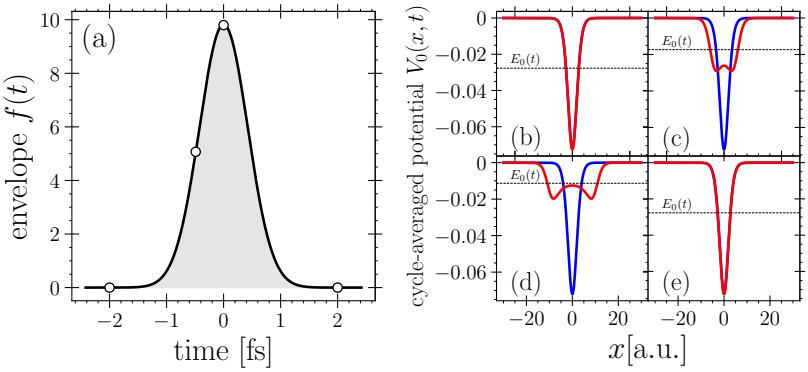

Figure 3.2: Envelope (a) and the cycle-averaged potential V_0 (b-e) along with its ground state E_0 for some selected time on the envelope respectively. The pulse parameters are of the field strength $\mathcal{E}_0 = 1$ a.u., the carrier frequency $\omega = 0.314$ a.u. and the pulse duration of $T = 1$ fs. The blue curve denotes the atomic potential, and the red curve denotes the cycle-averaged potential for different times.

We have the potential V_0, which changes slowly over time and depends on changing the envelope. Here, we use the adiabatic approximation [22] to calculate the transition matrix.

Begin with the eigenvalue equation

$$H(t)\,|n;t\rangle = E_n(t)\,|n;t\rangle\,, \tag{3.6}$$

where $|n;t\rangle$ and $E_n(t)$ are the instantaneous eigenstate and eigenenergy respectively. Here we used the Sakurai notation [22]. The general solution for the Schrödinger equation $\mathrm{i}\hbar\,\partial_t\,|\psi(t)\rangle = H(t)\,|\psi(t)\rangle$ is given by

$$|\psi(t)\rangle = \sum_n c_n(t)\,|n;t\rangle\,\mathrm{e}^{\mathrm{i}\theta_n(t)}, \tag{3.7}$$

where

$$\theta_n(t) = \frac{1}{\hbar}\int_{-\infty}^{t} E_n(t')\mathrm{d}t'. \tag{3.8}$$

Inserting Eq. (3.7) into the TDSE, we obtain

$$\sum_n \mathrm{e}^{\mathrm{i}\theta_n(t)}\left[\dot{c}_n(t)\,|n;t\rangle + c_n(t)\partial_t\,|n;t\rangle\right] = 0. \tag{3.9}$$

Taking inner product of $\langle m;t|$ from left leads to

$$\dot{c}_m(t) = -\sum_n c_n(t) \mathrm{e}^{\mathrm{i}[\theta_n(t)-\theta_m(t)]} \langle m;t| \partial_t |n;t\rangle , \tag{3.10}$$

where $\langle m;t| \partial_t |n;t\rangle$ is the transition matrix. To make this the general case, we take the time derivative of both sides of Eq. (3.6), then we have

$$\langle m;t| \partial_t |n;t\rangle = \frac{\langle m;t| \partial_t H(t) |n;t\rangle}{E_n(t) - E_m(t)}. \tag{3.11}$$

The Hamiltonian in Eq. (3.11) may be replaced with $H_0(t)$. As a result, in order to have non-adiabatic ionization, in the first place, the eigenstate has to be changing quickly. This change is quantified in an overlap with two eigenstates. How large is this change, left-hand side in Eq. (3.11), is given by the ratio at the right-hand side. The ratio is large under the following two conditions:

- the time-derivative of the cycle-averaged potential has to be large
- the energy differences have to be small

These two conditions explain the intuitive picture of NAPI in the sketch in Fig. 3.1. The ground state is denoted by $m = 0$, and the continuum states by n. As a result, if n is small, just above the threshold, the energy differences are small, and this condition, along with the fast-changing envelope, explain the non-adiabatic peak, which is why most of the occupation goes to the low-energy continuum.

To conclude this section, we reviewed NAPI and provided two intuitive and mathematical pictures to explain this process and connect these two pictures. In the following section, we will consider this process with tailored laser pulses and try to reveal an exciting property to control NAPI.

3.3 Non-adiabatic ionization with tailored laser pulses

To be specific, we work with a pulse form which is routinely used in coherent control experiments [78, 96, 79]. It is generated in the frequency domain by a modulation of the spectral phase in the vector potential, as considered in Chapter 2

$$A(\omega') = \mathcal{N} \frac{\mathcal{E}_0}{\omega} \mathrm{e}^{-[\omega'-\omega]^2 T^2/8\ln 2} \mathrm{e}^{\mathrm{i}\varphi(\omega')} \tag{3.12}$$

of a pulse with peak field strength $\mathcal{E}_0$, carrier frequency ω and full-width-at-half-maximum duration T. Hereby $\mathcal{N} \equiv T/2\sqrt{2\pi \ln 2}$ ensures the proper amplitude of the corresponding

pulse. The phase in Eq. (3.12) is defined as $\varphi(\omega') = a\sin(\omega'\tau + \phi)$. The role of three control parameters a, τ and ϕ, which determine the spectral phase in Eq. (3.12), is more intuitive for the pulse expressed in the time domain, as given below in Eq. (3.14).

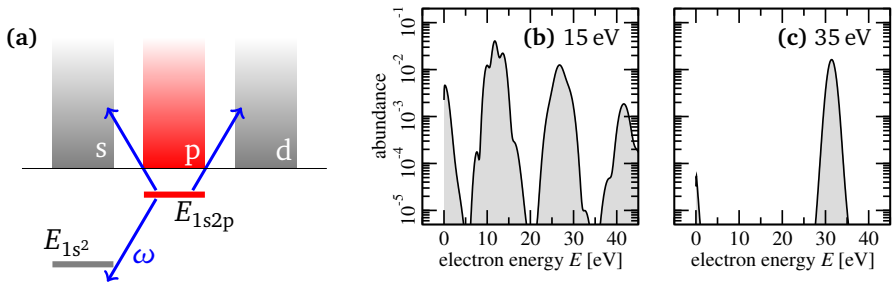

Figure 3.3: **(a)** Sketch of the physical system with the relevant states. **(b, c)** Photo-electron spectra in logarithmic scale from short intense pulses (I=10^{16}W/cm^2, T=1 fs) at two photon frequencies ω.

We do not aim at a specific control target, e. g., maximizing or minimizing the population of a specific state. Rather, we want to identify situations where the NAPI spectrum depends sensitively on pulse details, in particular the modulation phase ϕ. We will see that this requires another discrete state to be closely coupled, which acts as a "catalyzer" to evoke controllability of NAPI. To this end, we study ionization from the excited 1s2p state of Helium. Changing the photon frequency ω, non-resonant as well as resonant situations are realized by coupling to a deeper-lying bound state as indicated by the sketch in Fig. 3.3a. A resonant coupling can strongly enhance the Stark shift and thereby drive non-adiabatic ionization. We determine the electron dynamics in a single active-electron description.

The Helium atom is treated in the single-active-electron approximation. The following effective potential [97]

$$V(r) = -\frac{1 + \mathrm{e}^{-\alpha r}}{r} \tag{3.13}$$

with $\alpha = 2.1325$ has been used. It provides a good approximation for the energies of the relevant states of Helium, namely $E_{1s^2} = -24.59\,\mathrm{eV}$ and $E_{1s2p} = -3.48\,\mathrm{eV}$ (with the values $E_{1s^2} = -24.59\,\mathrm{eV}$ and $E_{1s2p} = -3.37\,\mathrm{eV}$ from accurate two-electron calculations [98]).

3.3.1 Ionization by single Gaussian pulses

To set the stage and put NAPI into perspective, we show the photo-electron spectra for single Gaussian pulses, Eq. (2.41), for two different photon frequencies ω in Fig. 3.3b,c. For

the smaller one ($\omega = 15\,\mathrm{eV}$) one can distinguish four peaks corresponding to the absorption of $j = 0 \ldots 3$ photons within the energy range shown. For future reference and for facilitating to address the features in the electron spectrum, we define energy intervals ΔE_j about these peaks with $\Delta E_j = \{E \,|\, -\omega/2 < E - E_j < \omega/2\}$ with $E_j \equiv E_0 + j\omega$ reached by a photon energy $j\omega$ from the initial state at E_0. Note, that the final electron states can carry different angular momentum ℓ in this few-photon scenario, see the sketch in Fig. 3.3a.

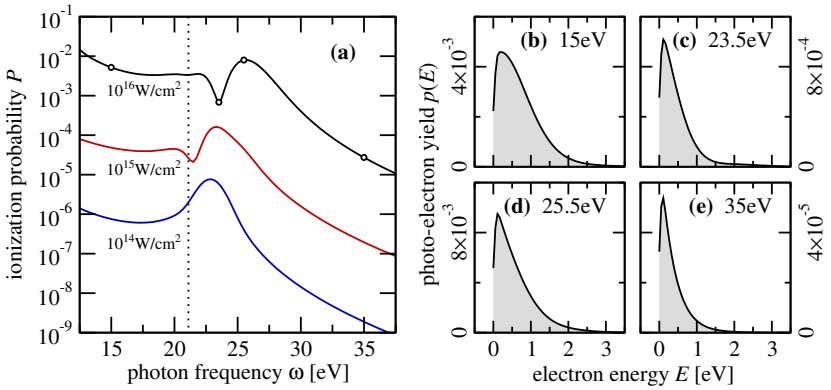

Figure 3.4: **(a)** Ionization probability for the non-adiabatic channel as a function of the photon frequency ω for a Gaussian pulse with duration T=1 fs and various intensities specified in the graph. The dotted line marks the transition energy between the $1s^2$ and 1s2p state, cf. Fig. 3.3. **(b–e)** Photo-electron spectra for selected frequencies specified in the graphs and marked in panel (a) with circles.

The NAPI channels correspond to "zero-photon absorption", which refers to the observation of an amplified ionization at low-energy electrons in the interval ΔE_0, with $E > 0$, forming the first peak in the spectra of Fig. 3.3b. In fact, this peak is the result of a two-photon Raman-like process which excites the low-energy continuum close to the initial state in a combination of photon absorption and emission. The next peak around E_1 is the biggest one and corresponds to single-photon ionization into $\ell = 0, 2$ continua. It is structured through dynamic interference[50]. Also clearly visible on the logarithmic scale are the peaks in the intervals ΔE_2 and ΔE_3, respectively. At the higher photon energy of $\omega = 35\,\mathrm{eV}$, the light-matter interaction is basically perturbative such that only the (standard) single-photon ionization peak E_1 survives, even on the logarithmic scale.

With Fig. 3.4 we explore the total NAPI probability P, as defined in Eq. (3.16), for continuum electrons with p-character (angular momentum ℓ=1) for an ultra-short (T=1 fs) Gaussian pulse as a function of ω for three different laser intensities. The p-state probabilities dominate since the NAPI process is an effective zero-photon process with a (small) admixture

of an even number of photons. Hence, optical selection rules do not permit ℓ=0, 2 final states to be reached from our initial p-state, and the allowed final f-state channel (ℓ=3) is much weaker than the final p-state channel.

Outside resonances, photo-ionization yields typically decrease with increasing frequency, for large ω proportional to $\omega^{-7/2}$ [99], which is also the case here. However, in the frequency range displayed, the spectrum is dominated by a resonance-like peak between 20 and 25 eV. For increasing intensity, it shifts slightly to larger ω and develops a preceding dip. This structure is due to the resonance with the $1s^2$–1s2p electron transition located (for weak fields) at $E_{1s2p} - E_{1s^2} \approx 21.1\,\mathrm{eV}$. Despite the strong variation of the yield around frequencies close to the resonance, the corresponding NAPI spectra (Fig. 3.4b–e) have remarkably similar and structure-less shapes inside and outside the resonance region, albeit on very different scales.

3.3.2 Sensitivity of non-adiabatic photoionization to the modulation phase

One might infer from the quite similar shapes of the NAPI spectra in Figs. 3.4b–e that it is very difficult to coherently control NAPI with standard shaped pulses. Yet, as it will turn out, a pulse train with a modulated spectral phase, routinely used in experimental realizations of pulse shaping in the frequency domain [78, 96, 79] can achieve controllability of NAPI. The pulse train is obtained from a Fourier transform $A(t) = \mathcal{F}[A(+\omega') + A^*(-\omega')]/2$ with $A(\omega')$ given in Eq. (3.12) and reads [70]

$$A(t) = \frac{\mathcal{E}_0}{\omega} \sum_k J_k(a)\, \mathrm{e}^{-2\ln 2[t-k\tau]^2/T^2} \cos\left(\omega[t-k\tau] - k\phi\right), \tag{3.14}$$

with J_k denoting Bessel functions. How strongly the original Gaussian pulse is distributed over separate pulses in the train is controlled by a, the amplitude of the phase oscillation in Eq. (3.12). We will choose a=1, which results in a train with essentially 9 pulses, since $J_{0\ldots4}(1) \approx \{0.765, 0.440, 0.115, 0.020, 0.002\}$. The delay between the pulses is fixed by τ. The modulation phase ϕ introduces a difference ϕ in the carrier-envelope phase of adjacent pulse members of the train, see Eq. (3.14), which will become important later on.

Firstly, we take a look at the ionization probability with this pulse train as we did in Fig. 3.4a for single Gaussian pulses. Figure 3.5a shows the probability $\overline{P}$ as a function of ω for the same three intensities I. Note that the separation $\tau = 4\,\mathrm{fs}$ together with the duration $T = 1\,\mathrm{fs}$ of the individual pulses in the train ensures that they do not overlap in time. The bar indicates that we have averaged the spectra over the modulation phase ϕ,

$$\overline{p}(E) = \frac{1}{2\pi} \int \mathrm{d}\phi\, p_\phi(E)\,, \tag{3.15}$$

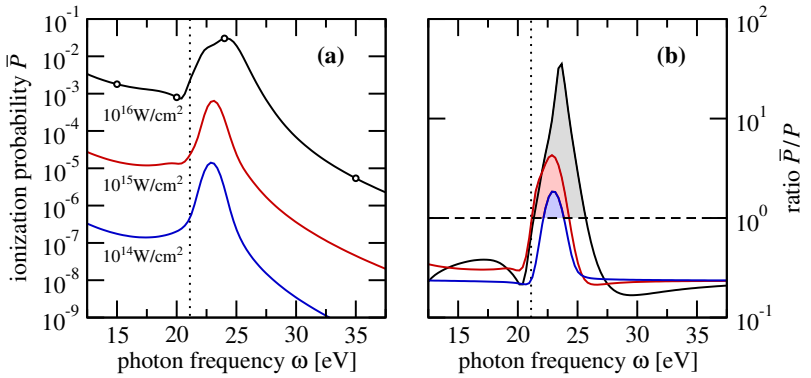

Figure 3.5: **(a)** Same as Fig. 3.4a but for a pulse train, given by Eq. (3.14), with a=1, τ=4 fs. The curves are averages over the phase parameter ϕ. **(b)** Ratios of the probabilities from panel (a) and Fig. 3.4a as a function of the photon frequency ω. The shadings mark the enhancement region.

with $\overline{P}$ being the integral over $\overline{p}(E)$. The corresponding non-adiabatic ionization probability are obtained from the integration

$$P = \int_0^{E_{1/2}} \mathrm{d}E\, p(E) \tag{3.16}$$

with the upper integration limit $E_{1/2} = E_0 + \omega/2$. Despite the different shapes compared to

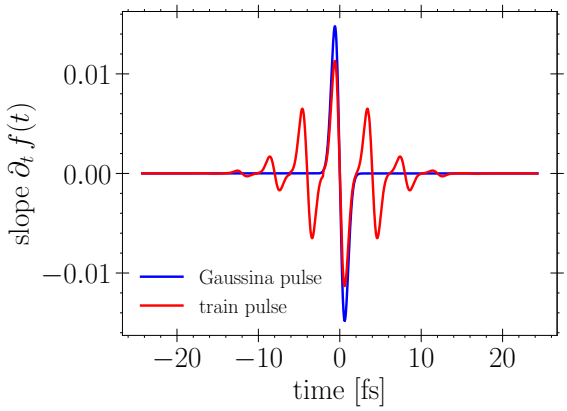

Figure 3.6: Time derivative of pulse envelope for the Gaussian pulse (blue line), and the sinusoidal pulse (red line).

the single-pulse yields in Fig. 3.4a, the qualitative behavior is the same: a monotonic decrease interrupted by a peak in the vicinity of $\omega \approx E_{1s2p} - E_{1s^2}$. Interestingly, the total yield can be *considerably* larger than for the Gaussian pulse, as apparent from Fig. 3.5b, which shows the ratio of the yields from Fig. 3.5a and Fig. 3.4a. Since NAPI is enhanced by large derivatives of

the pulse envelope [14], it is surprising that a longer pulse, with smaller slopes in the overall envelope, can induce an order-of-magnitude larger ionization probability at $I = 10^{16}\mathrm{W/cm^2}$. As shown in Fig. 3.6, the time derivative of the envelope for a single Gaussian pulse is larger than the pulse train.

The enhancement for all three intensities is visualized by shaded areas in Fig. 3.5b.

In contrast, outside the resonance region, for frequencies $\omega \lesssim 20\,\mathrm{eV}$ or $\omega \gtrsim 27\,\mathrm{eV}$, the ionization probability is strongly suppressed as expected for a stretched pulse.

Secondly, we want to assess how strongly the photo-electron spectra depend on the phase parameter ϕ, since a strong sensitivity could represent a knob for controlling NAPI. In order

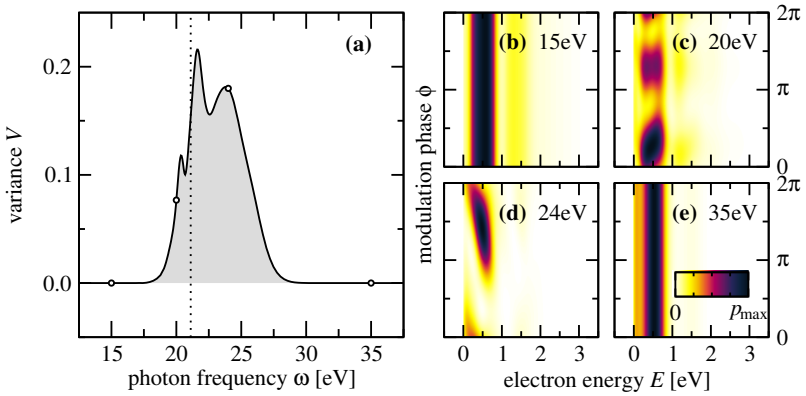

Figure 3.7: **(a)** Variance of the photo-electron spectra with respect to the modulation phase ϕ, defined in Eq. (3.17), for pulse trains according to Eq. (3.14) with $I{=}10^{16}\mathrm{W/cm^2}$, $a{=}1$, $\tau{=}4\,\mathrm{fs}$ as a function of the photon frequency ω. **(b–e)** Representative photo-electron spectra $p_\phi(E)$ as a function of ϕ for selected photon frequencies, marked with circles in Figs. 3.5a and 3.7a, with the color scale for the electron yield normalized to the maximal yield.

to quantify this sensitivity, we compute the variance of the spectra with respect to the modulation phase ϕ, defined as

$$V^2 = \frac{1}{\overline{P}^2} \int \mathrm{d}E \int \mathrm{d}\phi \left[p_\phi(E) - \overline{p}(E)\right]^2 \tag{3.17}$$

with $\overline{p}(E)$ from (3.15) above, and show it in Fig. 3.7a. As already seen for the probability, the region around the resonance sticks out and shows a noticeable variance. Below and above the resonance frequency, however, one sees the behavior characteristic for NAPI, namely that the ionization is determined by the envelope of the pulse only [14], but not by any carrier-oscillation features. In order to visualize this dependence, we show representative photo-electron spectra from different regions appearing in Fig. 3.5a in parallel to Fig. 3.7b–e now, however, as a function of electron excess energy and modulation phase ϕ. While for

a single Gaussian pulse, the photo-electron spectra are not affected by the resonance, the situation is quite different for the spectra generated with the pulse train: Here, the shape of the spectra varies strongly around the resonance for different ϕ.

3.3.3 The role of the catalyzing state

Having established that NAPI can be coherently controlled, at least in the presence of a catalyzing state which can be energetically very far away (here at an energetic distance of ω), we will elucidate the origin of the sensitivity of NAPI on ϕ in the vicinity of the resonance, in the pulse train.

In order to analyze the role of the catalyzing state, we build a dressed-state matrix

$$H_{jj'}(\mathcal{E}_0,\omega) = [E_j + n_j\omega]\delta_{jj'} + \frac{\mathcal{E}_0/\omega}{2} d_{j\ell_j j'\ell_{j'}}, \tag{3.18}$$

that has a block-diagonal shape, whereby the 5 blocks are defined by the "photon numbers" $n_j = \{+1,+1,0,-1,-1\}$ and the angular momenta $\ell_j = \{0,2,1,0,2\}$. To understand the details of the dressed-state calculation, the reader refers to the supplementary material in Ref. [100]. Field strength $\mathcal{E}_0$ and photon energy ω are parameters here. Field-free eigenenergies E_j and the coupling-matrix elements $d_{j\ell_j j'\ell_{j'}}$ are calculated as described in subsection 2.3.2.

The eigenstates V_{jk} from diagonalization of the matrix (3.18)

$$\sum_{j'} H_{jj'}(\mathcal{E}_0,\omega)V_{j'k}(\mathcal{E}_0,\omega) = V_{jk}(\mathcal{E}_0,\omega)E_k(\mathcal{E}_0,\omega) \tag{3.19}$$

are used to calculate by means of a angular-momentum projection operator $P^{[\ell]}_{jj'} \equiv \delta_{\ell\ell_j}\delta_{jj'}$ weights $w_k = \sum_{jj'} V_{jk}P^{[1]}_{jj'}V_{j'k}$ and therewith, according to

$$p(E) = \frac{1}{\sqrt{\pi}\delta E}\sum_{j}^{(\ell=1)} w_j \mathrm{e}^{-[E-E_{j\ell_j}]^2/\delta E^2}, \tag{3.20}$$

the density of states (DOS) shown in Fig. 3.8.

To this end, and using the dressed-state analyses, we show in Fig. 3.8 how energies of p-state (ℓ=1) electrons get "deformed", i. e. Stark shifted and hybridized, due to the coupling to s- and d-states. The color code of the hybridized density of states (DOS) marks the strength of their p-character at energy E (for a specific ω). The color-coded DOS also nicely illustrates the hybridization of angular momentum character of the DOS near the avoided crossings: Along an adiabatic trace which bends strongly near the avoided crossing, the character of the electron density changes, from dominant s-character through the $1s^2 + \omega$ dressed state (with a finite slope due to ω) to the 1s2p state with dominant p-character given by a horizontal line

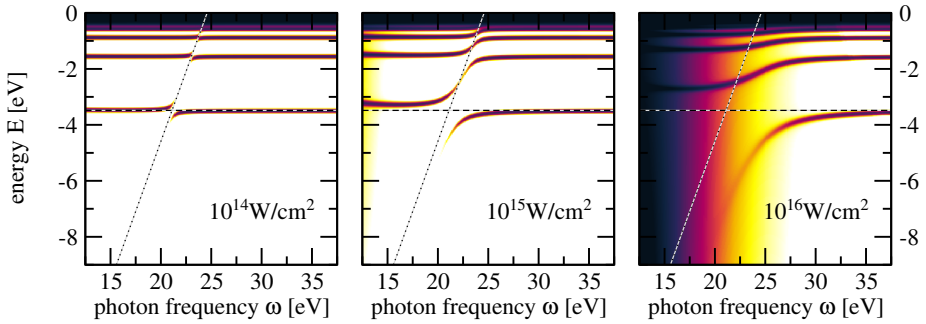

Figure 3.8: Density of states with p-character (ℓ=1) in logarithmic scale from a dressed-state diagonalization, as a function of the photon frequency ω for three laser intensities. The dashed horizontal line marks the energy E_{1s2p}, and the dotted sloping line marks the energy $E_{1s^2}+\omega$. They cross at resonance.

at energy E_{1s2p} which the electron density trace approaches towards large frequencies from below (and towards small frequencies from above). Note that the background density is also hybridized, most clearly visible from the area-filling color shades in Fig. 3.8.

At resonance $E_{1s2p} = E_{1s^2} + \omega$ the 1s2p-state shows an Autler-Townes splitting [48], i. e., structures below and above the field-free energy of $E_{1s2p} = -3.48\,\text{eV}$ (dashed line). The latter is crossed by the dressed state with field-free energy $E_{1s^2} + \omega$ (also shown with a dashed line). Note that the actual field-dressed states are shifted and have their interaction-caused avoided crossing at higher photon energies than the field-free states. This results in peaks consistently blue shifted with respect to the $\omega = E_{1s2p} - E_{1s^2}$ resonance energy of 21.1 eV in Figs. 3.4a – 3.7a. This blue shift is another signature of non-adiabatic ionization, which is in fact a virtual two-photon process: Whereas the coupling from the initial state to the catalyzing state ("1st photon") is symmetric around the resonance condition, the transition from the catalyzing state to the continuum ("2nd photon") is not. This can be illustrated in 2nd-order perturbation theory.

3.3.4 Second-order perturbation theory

In order to understand the optimal frequency in Fig. 3.4, we can take advantage of the 2nd-order perturbation theory. In chapter 4, we will widely examine the second-order perturbation theory. An exact expression is also provided for the Gaussian pulse that is given by

$$a^{[2]}(E_j) = -\frac{1}{8\hbar^2}\,\mathcal{A}_0^2\,\pi\,T^2 \sum_k d_{jk} d_{k0}\, \mathrm{e}^{-(\delta_\zeta^2+\delta_\sigma^2)} \left(1 + \mathrm{i}\,\mathrm{erfi}\Big(\frac{\delta_\sigma - \delta_\zeta}{\sqrt{2}}\Big)\right). \tag{3.21}$$

where $\delta_\sigma = (\omega_{jk} + \sigma\omega)T/2$ and $\delta_\zeta = (\omega_{k0} + \zeta\omega)T/2$ are the detuning variables, and $\sigma, \zeta = \pm 1$, can be "up" or "down." Function $\mathrm{erfi}(z) = -\mathrm{i}\,\mathrm{erf}(\mathrm{i}\,z)$ is the imaginary error function.

For maximizing the transition probability to the continuum, the imaginary part of Eq. (3.21) has to be zero. In other words, the argument of the imaginary error function, erfi, has to be zero which leads to

$$\delta_\sigma - \delta_\zeta = 0. \tag{3.22}$$

In the case of the zero-photon, we have two pathways "up-down" and "down-up", as shown

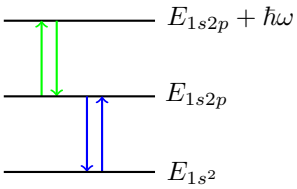

Figure 3.9: the two-photon process pathways that reach net zero-photon energy level.

in the sketch in Fig. 3.9. The dominant pathway is down-up since this path's matrix element is large. Therefore, from Eq. (3.22) we obtain the optimal frequency

$$\omega = \frac{E_{1s2p} - 2E_{1s^2}}{2} = \omega_{\mathrm{re}} + E_{1s2p}/2 \sim 23\mathrm{eV}, \tag{3.23}$$

where ω_{re} is the resonance frequency. Here we suppose that the zero-photon spectrum peaks close to zero, which is true when the intensity is low. This shifts to the higher energy for large intensity, and the maximum ionization probability shifts to the higher frequency. This also works for the case of two-photon ionization, while it peaks around $E_0 + \hbar\omega$. Therefore the maximum ionization probability happens at the resonance frequency $\omega = \frac{2E_{1s2p} - 2E_{1s^2}}{2} = \omega_{\mathrm{re}} = 21.1\mathrm{eV}$.

3.3.5 Pulse optimization

So far we considered NAPI in the presence of the catalyzing state, which becomes dependent on the phase details of the laser pulse. Another question then arises whether we can find a pulse that provides the maximum ionization probability in the presence of this state. For this matter, we take advantage of the optimization methods.

Laser pulse optimization is a process of finding the best parameters for a laser pulse to achieve a desired effect, such as maximum ionization probability. Various algorithms were used in ultra-fast laser systems for active feedback optimization of laser parameters or laser-matter interactions [101, 102]. Here we employ the Gaussian process and use a package

named M-Loop [103, 104], to optimize pulse parameters in the presence of the catalyzing state.

We found that the optimized pulse for this process in the presence of the catalyzing state is the temporal Airy pulse [70], which is the cubic term of the frequency phase expansion, i.e., $\varphi(\omega')$ in Eq. (3.12) is defined by

$$\varphi(\omega') = \alpha\,(\omega' - \omega)^3\,\frac{T^3}{3!(2\ln 2)^{\frac{3}{2}}}, \tag{3.24}$$

where α denotes "airy parameter". The corresponding pulse in the time domain (see Appendix D) is given by

$$A(t) = \mathcal{A}_\alpha\,\mathrm{e}^{(\frac{2}{9\alpha})^{2/3}\left(\frac{2/3\tau - t}{\Delta\tau}\right)}\,\mathrm{Ai}\left(\frac{\tau - t}{\Delta\tau}\right)\cos(\omega t), \tag{3.25}$$

where Ai describes the Airy function, and the field strength $\mathcal{A}_\alpha = \mathcal{A}_0\sqrt{4\pi}\,\tau$. Equation (3.25) shows that the temporal pulse shape exponentially decay and the Airy function is shifted by $\tau = \left(\frac{2}{9\alpha}\right)^{1/3} T/\sqrt{8\ln 2}$ and stretched by $\Delta\tau = \left(\frac{9\alpha}{2}\right)^{1/3} T/\sqrt{8\ln 2}$. Figure 3.10 shows the pulse for the airy parameter with different signs that it has a long tail and depends on the sign of the airy parameter.

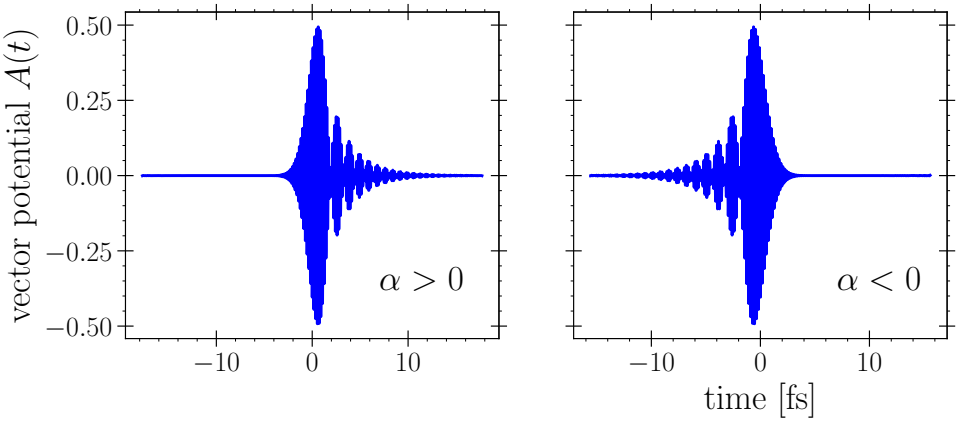

Figure 3.10: Temporal Airy pulse Eq. (3.25) with pulse parameters of pulse duration $T = 1\,\mathrm{fs}$, carrier frequency $\omega = 23.13\,\mathrm{eV}$, intensity $I = 10^{16}\,\mathrm{W/cm^2}$, and airy parameters $\alpha = \pm 0.6$.

The electron spectrum of NAPI driven by the temporal Airy pulse is depicted in Fig. 3.11. The non-adiabatic electron spectrum, the left panel in Fig. 3.11, for the negative sign of airy parameters is 8 times larger than the positive sign of the airy parameter, which is substantial for NAPI. Moreover, the electron spectrum for both positive and negative airy parameters is larger than the system driven by a Gaussian pulse with $\alpha = 0$. In the right panel of Fig. 3.11, the ionization probability is shown as a function of the airy parameter. The ionization

probability for the negative value of the airy parameter is larger than the positive value, and for the Gaussian pulse has the lowest value.

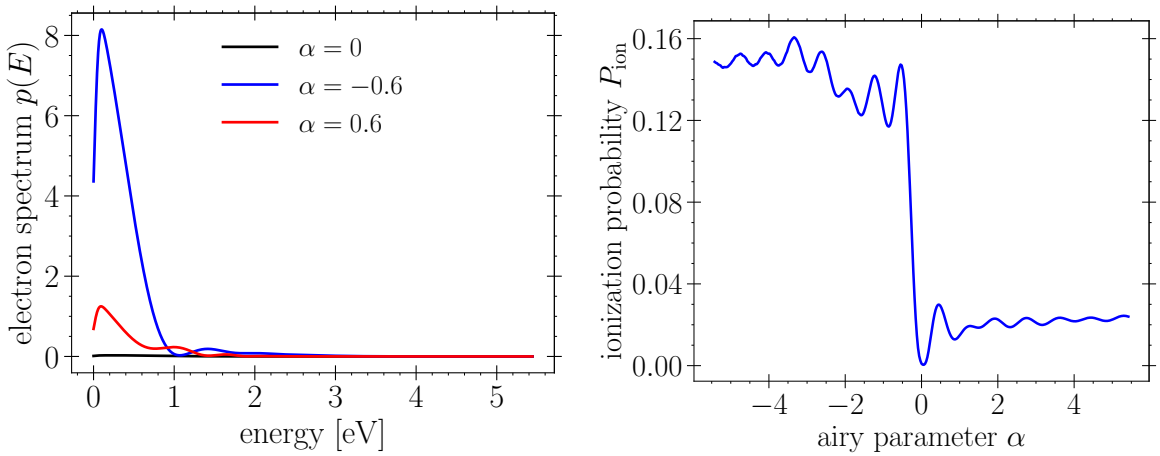

Figure 3.11: Left panel: Photoelectron spectrum driven by the temporal Airy pulse describes in Fig. 3.10 for different airy parameters $\alpha = \pm 0.6$, and 0. Airy parameter $\alpha = 0$ corresponds to a Gaussian pulse. Right panel: Ionization probability as a function of the airy parameter in which the system that is subjected to a Gaussian pulse in the presence of the catalyzing state has a minimum ionization.

To sum up, the temporal airy pulse for NAPI has a maximum ionization probability in the presence of the catalyzing state. In this pulse, there is only one parameter to tune, and the negative value of this parameter results in a large ionization probability. Since these temporal pulses are accessible in the experiment, and thanks to ultrashort pulses, which are now possible in the experiment [105, 9], NAPI can be experimentally measured in the near future.

3.4 Summary

We have investigated how non-adiabatic photo-ionization (NAPI) induced by ultra-short XUV pulses, can be influenced through specific pulse forms to exert coherent control as well-known for standard photo-ionization. We have demonstrated that a spectral-phase modulated pulse train, where individual pulses k in the train have different carrier-envelope phases $k\phi$, can achieve control *provided* an additional catalyzing state is available. A state qualifies as catalyzing if it forms a resonance with the initial state $E_0 - E_{\text{cat}} \approx \omega$. Since this kind of pulse trains is routinely used to shape longer optical pulses in the frequency domain and since

pulse shaping has also been demonstrated for XUV pulses recently, we expect that controlling NAPI will be possible experimentally in the future.

Moreover, while illustrated here with the quantitative example of Helium, the control scheme should be applicable to other targets as well, in particular as it relies on a resonant situation which usually dominates over other (e. g. multi-electron effects) in the vicinity of the resonant energy.

Chapter 4

Time-dependent Perturbation Theory for Ultrashort Pulses

4.1 Preface

Since analytical quantum solutions for a driven system are scarce, perturbation theory is a promising technique for providing insight. Time-dependent perturbation theory (TDPT) determines the effect of small, time-varying perturbations on a system described by a time-independent Hamiltonian. It is a tool for analyzing how a quantum mechanical system changes with time and provides a way to estimate the transition probabilities between different quantum states. It was developed by Born, Heisenberg, and Jordan in 1926 [16], later employed by Dirac for studying multiphoton processes [17, 18]. Dirac's time-dependent perturbation theory has served as a basis for perturbative solutions of the TDSE in different systems, such as quantum scattering [106, 22], quantum field theory [107, 108] and multiphoton processes [109, 110]. Despite being widely used, certain aspects remain difficult, for instance, the diverging terms that are related to "secular" and "normalization" terms (see Ref. [111] and references therein), where numerous attempts have been made to cope with these terms, including those with the renormalization group [112] or exponential functions [113]. The divergence of TDPT is also investigated in laser-induced atomic, and molecular transitions [114, 115], and still, diverging terms remain an open question.

The essence of the theory of multiphoton processes lies in the perturbation theory of one form or another. Perturbation theory has been utilized for the interaction of an atom with laser fields and examined for long laser pulses [116, 110], even for higher orders of TDPT [109]. With the advent of ultrashort laser pulses, atomic or molecular systems can be strongly perturbed [117], and the strong field ionization phenomenon has received attention, such as atomic stabilization [118], dynamic interference [50, 119], and non-adiabatic ionization [14, 15]. This chapter addressed TDPT for ultrashort pulses, and we show that it can be utilized to explain these phenomena in the frequency domain, thereby providing a multiphoton picture. We found that TDPT in ultrashort pulses can be an alternative technique to the time-propagating the Schrödinger equation. In TDPT, orders only depend on the fundamental pulse parameters, which are the parameters of the Fourier limited pulse; see section 2.4. The full-width-at-half-maximum (FWHM) duration acts as a parameter to control convergence. Furthermore, in the limit of slowly varying envelope approximation [120, 121], we found an explicit analytic expression for the non-adiabatic ionization, where it depends on the Fourier transform of the square envelope. Finally, atomic stabilization is explained in the frequency domain using third-order TDPT, and an expression for the critical field is provided.

This chapter is structured as follows. In Sec. 4.2, we give an overview of TDPT and describe how it can be used for ultrashort pulses in which we find that the TDPT's orders are

independent of pulse shaping parameters. Section 4.3, as the first application, second-order TDPT was considered in which we provide a model expression for non-adiabatic ionization that depends on the square of the pulse envelope. As the second application, the atomic stabilization is explained in the frequency domain using third-order TDPT, and we derive the critical field in Section 4.4. Lastly, in section 4.5, we conclude this chapter.

4.2 Introduction to time-dependent perturbation theory

Perturbation theory can be formulated directly in terms of the time evolution operator, see Dyson [122] and Feynman [123], which is considered in this chapter. Although, It can be equivalently formulated using operators form [124]. Knowing that our quantum system is in a specific state at time t_0, the goal is to determine its state at a later time t, which is related through the time-evolution operator $U(t, t_0)$. The problem is to determine the operator $U(t, t_0)$, where $\psi(t) = U(t, t_0)\psi(t_0)$, as exactly as possible. Here we start with the Schröndinger "picture." This operator is defined by integral equation [125]

$$U(t, t_0) = \mathbb{I} - \frac{\mathrm{i}}{\hbar}\int_{t_0}^{t} \mathrm{d}t' H(t')U(t', t_0), \tag{4.1}$$

or by the Schrödinger equation

$$\mathrm{i}\hbar\frac{\partial U(t, t_0)}{\partial t} = H(t)U(t, t_0), \tag{4.2}$$

with the boundary condition $U(t_0, t_0) = \mathbb{I}$. Since $H(t)$ is Hermitian, $U(t, t_0)$ is unitary. Consider the Hamiltonian in Eq. (2.16) given by $\hat{H}(t) = \hat{H}_0 + \hat{V}(t)$, where all time-dependent variables enter the potential $V(t)$, and $\hat{H}_0$ is the Hamiltonian of a Schrödinger equation whose solution is known. As in our case, $\hat{H}_0$ is computed numerically. It is useful to decompose the unitary operator as $U(t, t_0) = U^{[0]}(t, t_0)U_I(t, t_0)$, where $U^{[0]}(t, t_0)$ is the evolution operator corresponding to $\hat{H}_0$:

$$\mathrm{i}\hbar\frac{\partial U^{[0]}(t, t_0)}{\partial t} = H_0 U^{[0]}(t, t_0), \quad U^{[0]}(t_0, t_0) = \mathbb{I}. \tag{4.3}$$

The solution is known as $U^{[0]}(t, t_0) = \mathrm{e}^{-\mathrm{i}H_0(t-t_0)/\hbar}$, then U will be determined if

$$U_I(t, t_0) \equiv U^{[0]\,\dagger}(t, t_0)U(t, t_0) = \mathrm{e}^{\mathrm{i}H_0(t-t_0)/\hbar}U(t, t_0), \tag{4.4}$$

where $U_I(t, t_0)$ is the evolution operator for the states in the "interaction picture", derived from the Schrödinger picture by unitary transformation $U^{[0]\,\dagger}(t, t_0)$. With this definition, $U_I(t, t_0)$ may be defined through

$$\mathrm{i}\hbar\frac{\partial U_I(t, t_0)}{\partial t} = V_I(t)U_I(t, t_0), \tag{4.5}$$

where

$$V_I(t) \equiv U^{[0]}(t_0, t)V(t)U^{[0]}(t, t_0). \tag{4.6}$$

Integrating this equation from t_0 to t, we obtain

$$U_I(t, t_0) = U_I(t_0, t_0) - \frac{\mathrm{i}}{\hbar}\int_{t_0}^{t} \mathrm{d}t' V_I(t')U_I(t', t_0). \tag{4.7}$$

This result provides a "self-consistent" equation for $U_I(t, t_0)$, i.e., if we take this expression and substitute $U_I(t', t_0)$ in the integrand, we obtain

$$U_I(t, t_0) = \sum_{n=0}^{\infty}\left(-\frac{\mathrm{i}}{\hbar}\right)^n \int_{t_0}^{t} \mathrm{d}t_1 \cdots \int_{t_0}^{t_{n-1}} \mathrm{d}t_n V_I(t_1)V_I(t_2)\cdots V_I(t_n), \tag{4.8}$$

where the term corresponding to $n = 0$ is $\mathbb{I}$. From this result, with the aid of Eq. (4.4), and Eq. (4.6) we get the following expansion for U:

$$U(t, t_0) = \sum_{n=0}^{\infty} U^{[n]}(t, t_0), \tag{4.9}$$

where

$$\begin{aligned} U^{[n]} = (-\mathrm{i}/\hbar)^n \int\limits_{t>t_n>\cdots>t_0} \mathrm{d}t_n \mathrm{d}t_{n-1}\cdots\ \mathrm{d}t_1\ U^{[0]}(t, t_n)V(t_n)U^{[0]}(t_n, t_{n-1}) \\ \times\cdots\ U^{[0]}(t_2, t_1)V(t_1)U^{[0]}(t_1, t_0), \end{aligned} \tag{4.10}$$

where $U^{[0]}$ represents the zero-order approximation, and $U^{[1]}, U^{[2]}, \ldots$ are the corrections of order $1, 2, \ldots$ to that approximation. In practice, the calculation of these corrections becomes increasingly complicated with higher orders, and one usually takes only the lowest-order corrections.

We assume the eigenvalue problem of $H_0 \left|j\right\rangle = E_j \left|j\right\rangle$ to be solved, where the $\left|j\right\rangle$ are a complete set of eigenvectors of H_0 with corresponding eigenvalues E_j. Thus we define $\omega_{jk} = (E_j - E_k)/\hbar$ which is the "Bohr frequency" relative to the transition $k \to j$.

If at the initial time t_0 the system is in the state $\left|i\right\rangle$, the system will be in a final state j with the probability amplitude $a_j(t)$ given by

$$a_j(t) = \left\langle j\right| U(t, t_0) \left|i\right\rangle = \sum_n \left\langle j\right| U^{[n]}(t, t_0) \left|i\right\rangle, \tag{4.11}$$

or more explicitly,

$$\begin{aligned} a_j(t) = \delta_{ji} &- \frac{\mathrm{i}}{\hbar}\int_{t_0}^{t} \mathrm{d}t' \left\langle j\right| V(t') \left|i\right\rangle \mathrm{e}^{\mathrm{i}\omega_{ji}t} \\ &- \frac{1}{\hbar^2}\int_{t_0}^{t} \mathrm{d}t' \int_{t_0}^{t'} \mathrm{d}t'' \sum_k \left\langle j\right| V(t') \left|k\right\rangle \left\langle k\right| V(t'') \left|i\right\rangle \mathrm{e}^{\mathrm{i}\omega_{jk}t' + \mathrm{i}\omega_{ki}t''} + \cdots. \end{aligned} \tag{4.12}$$

Therefore, the expansion of the probability amplitude into a power series is given by

$$a_j(t) = \sum_n a_j^{[n]}(t), \tag{4.13}$$

where $a_j^{[0]}(t) = \delta_{ji}$ is the initial condition. The time-dependent amplitude, $a_j(t)$, satisfies the normalization condition of $\sum_j |a_j(t)|^2 = 1$. Moreover, we can define the matrix element in the velocity gauge as

$$V_{jk}(t) \equiv \langle j| V(t) |k\rangle = d_{jk} A(t), \tag{4.14}$$

where d_{kl} is the dipole matrix element in the velocity gauge, and $A(t)$ is the vector potential, see also Eq. (2.22). Assuming that an atom is in the initial state before the laser field is turned on, i.e., $t_0 \to -\infty$, the probability amplitude at time $t > t_0$ can be obtained using the following relation

$$\boxed{a_j^{[n]}(t) = -\frac{\mathrm{i}}{\hbar} \sum_k d_{jk} \int_{-\infty}^{t} \mathrm{d}t' A(t') \mathrm{e}^{\mathrm{i}\omega_{jk}t'} a_k^{[n-1]}(t').} \tag{4.15}$$

Equation (4.15) is solved numerically using the finite difference method, Appendix E.

Since we are interested in finding the electron in its final state with E_j at $t \to \infty$, therefore

$$a^{[n]}(E_j) \equiv a_j^{[n]}(t \to \infty) = -\frac{\mathrm{i}}{\hbar} \sum_k d_{jk} \int_{-\infty}^{\infty} \mathrm{d}t\, A(t) \mathrm{e}^{\mathrm{i}\omega_{jk}t} a_k^{[n-1]}(t). \tag{4.16}$$

Henceforth, $a^{[n]}(E_j) = a_j^{[n]}(t \to \infty)$ is denoted to be the probability amplitude of finding the particle in the state j. In the case of degeneracy or different angular momentum, another index can appear beside index j.

As an example, we consider the first-order TDPT with initial condition $a_i(-\infty) = 1$ and $a_j(-\infty) = 0$ for all $j \neq i$, which describes single-photon ionization:

$$a^{[1]}(E_j) = -\frac{\mathrm{i}}{\hbar} d_{ji} \int_{-\infty}^{\infty} \mathrm{d}t' A(t') \mathrm{e}^{\mathrm{i}\omega_{ji}t'} = -\frac{\mathrm{i}}{\hbar} d_{ji}\, \mathcal{F}\left[A(t)\right](\omega_{ji})\,. \tag{4.17}$$

Equation (4.17) signifies that the single-photon ionization is the Fourier transform Eq. (2.31) of the pulse, here $\mathcal{F}$ indicates the Fourier transform. This implies that the shorter pulse in the time domain, the wider the spectrum in the energy domain.

In the case that the laser pulse has a Gaussian envelope Eq. (2.41), the probability of transition from initial state $|i\rangle$ to final state $|j\rangle$ is given by

$$P_{i\to j} = \left|a^{[n]}(E_j)\right|^2 = \left| -\frac{\mathrm{i}}{2\hbar} \mathcal{A}_0 T \sqrt{\frac{\pi}{2\ln 2}}\, d_{ji} \sum_{\pm} \mathrm{e}^{-(\omega_{ji} \pm \omega)^2 \frac{T^2}{8\ln 2}} \right|^2, \tag{4.18}$$

where $\mathcal{A}_0$ is central pulse strength, T is the pulse duration, and $\cos(\omega t) = 1/2 \sum_{\pm} \mathrm{e}^{\pm \mathrm{i}\omega t}$.

In perturbation theory, the behavior of pathways is similar to a binary tree, and the number of pathways is proportional to 2^n, where n is the perturbation order. Here in 1st-order PT, we have two pathways: the final energy reaches $E_0 + \hbar\omega$ or $E_0 - \hbar\omega$, as can be seen in the sketch in Fig. 4.1.

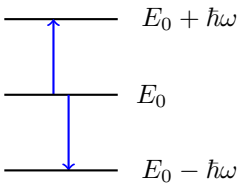

Figure 4.1: Single-photon ionization pathways

We keep the term with "$-$" sign in Eq. (4.18), and since $E_j - E_i > 0$, therefore $\omega_{ji} + \omega$ is very large and $\mathrm{e}^{-(\omega_{ji}+\omega)^2 T^2/8\ln 2}$ is exponentially suppressed. As a result, the term with the "$+$" sign is neglected. For an initial condition in the ground state, all states are occupied around $E_0 + \hbar\omega$, so the single-photon spectra has a peak around this energy.

In some situations, the first-order TDPT is not applicable, because its use relies on the following two conditions

- the laser carrier frequency (ω) is high enough to overcome the gap between the initial state and the ionization threshold. As an example, If the ground state is the initial state, the gap is the ionization potential I_p.
- the shift of the atomic state, ponderomotive energy Eq. (2.1), has to be negligible in comparison with the maximum kinetic energy, i.e., $E_{\mathrm{kin,max}} = \hbar\omega - I_p$ then

$$U_p = \frac{\mathcal{E}_0^2}{4\omega^2} \ll E_{\mathrm{kin,max}} \Rightarrow \mathcal{E}_0 \ll 2\sqrt{\omega(\hbar\omega - I_p)}, \tag{4.19}$$

  this ensures that the atomic state has no Stark shift. Here $\mathcal{E}_0$ is the electric field strength.

With the advent of intense laser pulses, particularly high-intensity laser, the first-order TDPT is no longer applicable and breaks down. Furthermore, the electron spectrum gets more complicated in this regime [4, 44, 50, 119]. This signifies that the photoelectron spectra need to be modified by contributing higher orders of TDPT.

4.2.1 Higher order time-dependent perturbation theory

In high-order perturbation theory, the perturbation is treated to a higher order of approximation, which means that more terms in the series of corrections are included. This results in

a more accurate description of the system's behavior under the perturbation but also makes the calculations more complex and computationally intensive. We numerically solved the series in Eq. (4.15), see Appendix E, and investigated the photoelectron spectra at the end of the pulse. We continued adding more orders until no significant changes in the final result were observed in the spectrum we wished to compare to the TDSE solution.

Figure 4.2 shows comparisons between the electron spectrum obtained from TDSE solution and Eq. (4.16) for various intensities of the three-dimensional hydrogen atom solution driven by a Gaussian envelope pulse. Higher intensity, makes convergence more difficult, resulting in a significantly higher order of the TDPT. The deviation from the maximum energy

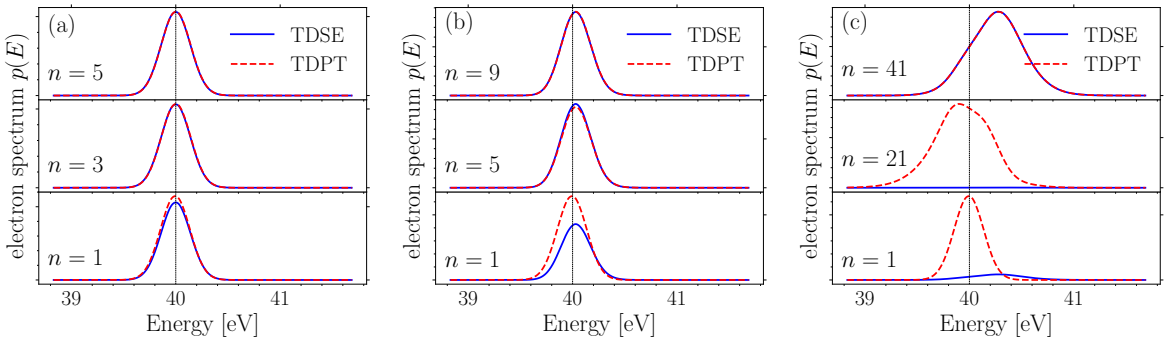

Figure 4.2: Single-photon photoelectron spectra, which is defined in Eq. (2.26), for $1s$ hydrogen exposed to a 5 fs pulse with a carrier frequency of $\omega = 53.6\,\text{eV}$ for different intensities, compared with TDSE for different perturbation order n. (a) For intensity $I = 10^{15}\,\text{W/cm}^2$, TDPT requires 5 orders, (b) for $I = 10^{16}\,\text{W/cm}^2$, requires 9 orders, and (c) for $I = 10^{17}\,\text{W/cm}^2$, requires 41 orders to get converged.

of $E_0 + \hbar\omega$ which is depicted as a vertical line at $E = 40\,\text{eV}$ in Fig. 4.2 at higher intensity is known as the dynamic interference [50]. As the intensity increases, the spectra get wider, which can be explained by the fact that higher orders of TDPT become dominant at higher intensities. Since each order of TDPT is proportional to the Fourier transform of the pulse envelope to the power of that order $\mathcal{F}[f^n(t)]$, higher orders are wider in spectra. More on this in Sections 4.3 and 4.4.

A sequence of events can sometimes be expected to settle into a pattern. The pattern may, for instance, be convergence in the classical sense to a fixed value. If there is a reliable reference, then we compare the outcomes with that reference, but in most cases, such a reference does not exist. Therefore, a quantity that ensures the series converges is needed.

This quantity can be defined as

$$\mathrm{Pr}_n = \sum_j |a^{[n]}(E_j)|^2, \tag{4.20}$$

which is the so-called "convergence in probability", see Van der Vaart 1998 [126]. The basic idea behind this is that as the sequence progresses, the probability of an "unusual" outcome decreases. Consequently, if this quantity reaches zero for large n,

$$\lim_{n \to N} \mathrm{Pr}_n \sim 0, \tag{4.21}$$

the series get converged, i.e., no more correction term is needed. If this condition is fulfilled, the TDPT converges to a finite value.

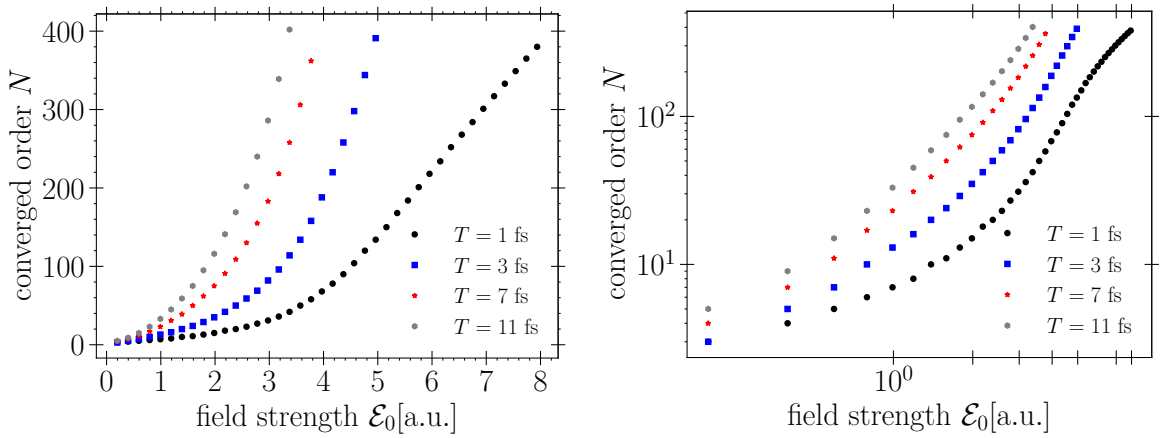

Figure 4.3: Converged order N for $1s$ hydrogen exposed to the Gaussian pulse for different durations T with the carrier frequency $\omega = 54$ eV as a function of electric field strength. Left panel: linear scale. Right panel: logarithmic scale.

In certain instances, the expansion of the time evolution operator (perturbation orders) in terms of matrix elements in a particular basis set may not necessarily converge [111]. Many efforts were made to deal with diverging terms [112, 113, 114, 115]. However, in ultrashort laser pulses, another parameter plays an important role, which is a feature of the pulse envelope. We found that the full-width-at-half-maximum (FWHM) duration T can act as a parameter that controls the divergence of TDPT orders. For very short pulses, TDPT is converged fast and can cover higher intensities, see Fig. 4.3. On the contrary, as expected, the diverging terms become dominant in the long pulse regime, and TDPT diveres rapidly.

In order to calculate the converged order, N, we monitor the quantity in Eq. (4.20) for

each order. When this quantity for an order n_*, reaches a threshold, $\mathrm{Pr}_{n_*} < \epsilon$, we record the converged order N, where $\epsilon \sim 10^{-6}$.

Ultrashort pulses are extremely brief bursts of electromagnetic radiation, typically in the form of light, that last for just a few femtoseconds or even attoseconds. These ultrashort pulses have revolutionized the field of ultrafast science, allowing researchers to study phenomena that occur on incredibly short timescales [9]. With the accessibility of ultrashort pulses in experiments, TDPT gets more attention and can be used as an alternative solution for TDSE. As shown in Fig. 4.3, in the attosecond regime, it is possible to reach a very high intensity that is accessible in experiments at the moment, without any diverging in TDPT terms.

With advanced experimental techniques, pulse shaping is accessible in the ultrashort regime [65, 66, 78, 79, 80, 77], accordingly, more parameters that control the pulse are involved. These parameters may play a role in the divergence or convergence of TDPT. In the next section, we address this point.

4.2.2 Perturbation theory in shaped short laser pulse

For the Gaussian envelope pulse, the convergence of TDPT strongly depends on the fundamental parameters, i.e., intensity I, carrier frequency ω, and the FWHM duration T. Moreover, we can form a pulse with a complicated shape by changing the modulated phase in its definition in the frequency domain. Thus, these pulses are controlled by some extra parameters. In this subsection, we wish to know the effect of modulated phase parameters on the convergence of TDPT.

As discussed in Chapter 2, the general pulse definition is given by

$$A(\omega') = \mathcal{N}\mathcal{A}_0 \mathrm{e}^{-(\omega'-\omega)^2 T^2/4}\ \mathrm{e}^{\mathrm{i}\varphi(\omega')}, \tag{4.22}$$

where $\varphi(\omega')$ represents the modulated spectral phase and $\mathcal{N} \equiv T/\sqrt{4\pi}$. Assume that the modulated phase has the form $\varphi(\omega') = a\sin(\tau\omega' + \phi)$ and is controlled by three parameters: a, τ, and ϕ (see Fig. 2.4). By setting $a = 1$ and $\phi = 0$, we examine the parameter τ, which fixes the time delay between the sub-pulses. To contemplate perturbation order and phase parameters, we define a cost function, which is a quantity that measures the difference between the predicted output and actual output of a model, and the goal is to minimize the cost function with an exact reference, as

$$\mathrm{C}_n(\tau) = \frac{\int \mathrm{d}E\ \left[p_{\mathrm{ref}}(E,\tau) - p_n(E,\tau)\right]^2}{\int \mathrm{d}E\ \left[p_{\mathrm{ref}}(E,\tau)\right]^2}, \tag{4.23}$$

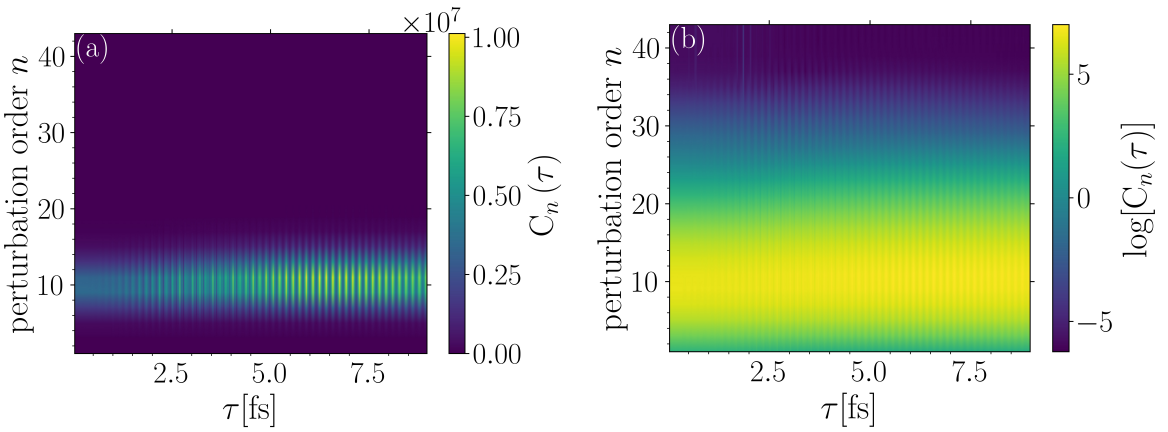

Figure 4.4: Cost function, $C_n(\tau)$ in Eq. (4.23), for $1s$ hydrogen atom for the pulse with sinusoidal modulated phase defined in Eq. (2.46) as a function of τ and the perturbation order n. (a) Linear scale and (b) logarithmic scale, with pulse parameters as $T = 3\,\text{fs}$, $\omega = 24.5\,\text{eV}$, and $I = 10^{16}\,\text{W/cm}^2$. The cost function increases as going to higher orders and finally converges at $n \approx 43$ for all values of τ.

where p_{ref} is the reference photoelectron spectra, which are calculated from the TDSE solution. Figure 4.4 is depicted the single-photon ionization of a three-dimensional hydrogen atom. As seen in Fig. 4.4, the number of orders required to converge is independent of the delay between sub-pulses, and this is surprising since by increasing τ, the pulse in the time domain gets stretched and becomes much longer than the Fourier-limited pulse (see Fig. 2.4). Still, it needs the same number of orders as for the Fourier-limited. The ripples in Fig. 4.4 are because of the period of the pulse that we have used. The reason is that the middle single Gaussian peak in this pulse train (see Fig. 2.4) is dominant. Therefore, if we, for example, intentionally remove the middle pulse train, the PT's order becomes dependent on pulse train parameters.

To sum up, the perturbation orders required for convergence depend only on the fundamental pulse parameters, i.e., T, $\mathcal{A}_0$, ω, and the pulse shaping parameters, namely, τ, does not affect the convergence of TDPT. In the following two sections, we introduce two applications of TDPT in the ultrashort regime, non-adiabatic ionization, and interference stabilization.

4.3 Application I: non-adiabatic ionization

In the high-intensity regime, second-order TDPT, which describes the two-photon ionization was used, particularly when an electron can be ionized with the help of two photons [40] that is experimentally verified [41, 42]. We found that in the ultrashort pulse regime, the second-order perturbation theory finds an application, known as the "non-adiabatic" transition, which happens due to the fast-changing of states. This transition, see Fig. 4.5, is mostly considered in the time domain, and it first appeared in Ref. [127] considering ATI peaks [4, 128] in the stabilization regime [129, 130], and was later studied in detail [12, 13] using the Siegert-state expansion for nonstationary systems [131]. In this section, we take advantage of TDPT to investigate this process in the energy domain.

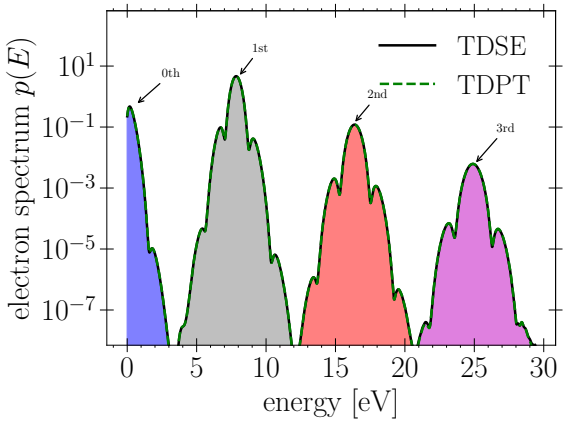

Figure 4.5: ATI peaks in the log scale of a 1D system that is defined in Eq. (4.37) for the Gaussian pulse with $T = 2\,\text{fs}$, $\omega = 0.314\,\text{a.u.}$, and $\mathcal{A}_0 = 1\,\text{a.u.}$

Figure 4.5 shows the electron spectrum Eq. (2.26) that are ATI peaks, of which the 0th ATI peak is the motivation of this section. We consider this process using perturbation theory and will provide a model in order to understand it. The rising and falling observed in the 1st, 2nd, etc. peaks are related to the stabilization [132] which will be discussed in the next section. Those in the 0th peak will be discussed in this section. It's worth mentioning that each ATI peak has an under-curve area that is distinct by different colors. The integral over the under-curve area with a specific energy range gives the ionization probability of that ATI peak.

Second-order PT contains eight pathways that are sketched in Fig. 4.6. It describes two-photon ionization, in which the pathway reaches net two-photon energy $E_0 + \hbar\omega$, and non-adiabatic ionization, in which pathways reach net energy E_0. The latter process is the

focus of this section.

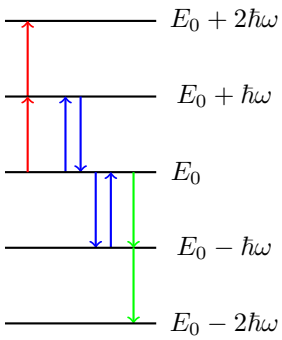

Figure 4.6: All possible pathways of the second-order PT. Red arrows end net two-photo ionization with final energy $E_0 + \hbar\omega$. Blue arrows end net final energy E_0. Green arrows do not participate in ionization because they are exponentially suppressed, as explained in Fig. 4.1.

Finding an electron in the final state $|j\rangle$ at time $t \to \infty$ for the general pulse Eq. (2.38), is derived in 2nd-order PT from Eq. (4.16) which reads

$$a^{[2]}(E_j) = -\frac{1}{\hbar^2}\sum_k d_{jk}d_{k0}\int_{-\infty}^{\infty} \mathrm{d}t\, A(t)\mathrm{e}^{\mathrm{i}\omega_{jk}t}\int_{-\infty}^{t} \mathrm{d}t'\, A(t')\mathrm{e}^{\mathrm{i}\omega_{k0}t'}, \tag{4.24}$$

where we assumed the initial state is the atom's ground state, i.e., $|i\rangle = |0\rangle$. If the laser pulse has the form $A(t) = \mathcal{A}_0\cos(\omega t)$, the transition probability in second order is given by

$$a^{[2]}(E_j) = -\frac{\mathrm{i}}{4\hbar^2}\mathcal{A}_0^2\sum_k d_{jk}d_{k0}\lim_{\epsilon\to 0^+}\left[\frac{\delta(\omega_{j0})+\delta(\omega_{j0}+2\omega)}{\omega_{k0}+\omega-\mathrm{i}\epsilon} + \frac{\delta(\omega_{j0})+\delta(\omega_{j0}-2\omega)}{\omega_{k0}-\omega-\mathrm{i}\epsilon}\right], \tag{4.25}$$

where we have used $\omega_{j0} = \omega_{jk} + \omega_{k0}$, and δ is the Dirac delta function. The second-order terms in the probability are maximal for $E_j = E_0$ and $E_j = E_0 \pm 2\omega$. The peaks for $E_j = E_0 \pm 2\omega$ correspond to two-photon absorption or two-photon emission. The peaks for $E_j = E_0$ correspond to one photon absorption and one photon emission. This is the so-called "*net zero-photon*" transition, short "*zero-photon*", transition in which the photon that has been first emitted or absorbed is given by the denominator $\omega_{k0} + \omega$ (resp. $\omega_{k0} - \omega$).

Solving integrations in Eq. (4.24) for a general pulse analytically is challenging. However, an exact solution exists for certain pulses, such as the Gaussian pulse. For simplification, we define two variables that can be interpreted as detuning

$$\delta_\zeta \equiv (\omega_{k0} + \zeta\omega)T/2, \quad \text{and} \quad \delta_\sigma \equiv (\omega_{jk} + \sigma\omega)T/2, \tag{4.26}$$

where ζ and σ can be "*up*" or "*down*", so that $\zeta, \sigma = \pm 1$.

Second-order TDPT for the Gaussian pulse is given by

$$\begin{aligned} a_j^{[2]}(t) = &-\frac{1}{16\hbar^2}\mathcal{A}_0^2\pi T^2\sum_k d_{jk}d_{k0}\mathrm{e}^{-\delta_\zeta^2-\delta_\sigma^2}\Big[1+\mathrm{erf}\left(t/T-\mathrm{i}\delta_\zeta\right)\Big] \\ &-\frac{1}{8\hbar^2}\mathcal{A}_0^2\sqrt{\pi}T\sum_k d_{jk}d_{k0}\mathrm{e}^{-\delta_\zeta^2-\delta_\sigma^2}\int_{-\infty}^{t}\mathrm{d}t'\mathrm{e}^{-\frac{1}{T^2}(t'-\mathrm{i}\delta_\sigma)^2}\,\mathrm{erf}\left(t'/T-\mathrm{i}\delta_\zeta\right). \end{aligned} \tag{4.27}$$

The integration in the second term does not have a close form, but it can be solved for $t\to\infty$. The solution[1] is given by

$$\int_{-\infty}^{\infty}\mathrm{d}t\,\exp\Big[-\frac{1}{T^2}(t-\mathrm{i}\delta_\sigma)^2\Big]\,\mathrm{erf}\left(\frac{t-\mathrm{i}\delta_\zeta}{T}\right)=\mathrm{i}\,T\sqrt{\pi}\,\mathrm{erfi}\left(\frac{\delta_\sigma-\delta_\zeta}{T\sqrt{2}}\right), \tag{4.28}$$

where here we use the fact that $\frac{\mathrm{d}}{\mathrm{d}z}\,\mathrm{erf}(z)=\frac{2}{\sqrt{\pi}}\mathrm{e}^{-z^2}$, and $\mathrm{erfi}(z)=-\mathrm{i}\,\mathrm{erf}(\mathrm{i}z)$ is the imaginary error function. Substituting the solution of Eq. (4.28) into Eq. (4.27), the two-photon occupation, is given by

$$a^{[2]}(E_j)=-\frac{1}{8\hbar^2}\mathcal{A}_0^2\pi T^2\sum_k d_{jk}d_{k0}\mathrm{e}^{-(\delta_\zeta^2+\delta_\sigma^2)}\left(1+\mathrm{i}\,\mathrm{erfi}\Big(\frac{\delta_\sigma-\delta_\zeta}{\sqrt{2}}\Big)\right). \tag{4.29}$$

Since the imaginary error function diverges rapidly which makes it difficult for numerical calculation, one can use the Dawson function $F(x)\equiv\frac{\sqrt{\pi}}{2}\mathrm{e}^{-x^2}\mathrm{erfi}(x)$. Then, the two-photon occupation becomes

$$a^{[2]}(E_j)=-\frac{1}{8\hbar^2}\mathcal{A}_0^2\pi T^2\sum_k d_{jk}d_{k0}\left(\mathrm{e}^{-(\delta_\zeta^2+\delta_\sigma^2)}+\mathrm{i}\,\frac{2}{\sqrt{\pi}}\,F\Big(\frac{\delta_\sigma-\delta_\zeta}{\sqrt{2}}\Big)\mathrm{e}^{-\frac{1}{2}(\delta_\zeta+\delta_\sigma)^2}\right), \tag{4.30}$$

which is more convenient for numerical calculation.

Equation (4.30) is an exact solution for a Gaussian pulse. Using the same strategies, an exact solution also can be obtained for a sinusoidal pulse[2], as defined in Eq. (2.46). However,

[1] Assume $\delta_\zeta>0$, $\delta_\sigma>0$, and $T>0$, then the integration can be solved as follows

$$\begin{aligned} &\int_{-\infty}^{\infty}\mathrm{d}t\,\exp\Big[-\frac{1}{T^2}(t-\mathrm{i}\delta_\sigma)^2\Big]\,\mathrm{erf}\left(\frac{t-\mathrm{i}\delta_\zeta}{T}\right) \\ &\quad=\int\left(\int_{-\infty}^{\infty}\frac{\partial}{\partial\delta_\zeta}\,\mathrm{erf}\left(\frac{t-\mathrm{i}\delta_\zeta}{T}\right)\exp\Big[-\frac{1}{T^2}(t-\mathrm{i}\delta_\sigma)^2\Big]\mathrm{d}t\right)\mathrm{d}\delta_\zeta \\ &\quad=\int\left(-\frac{2\mathrm{i}}{T\sqrt{\pi}}\,\frac{T\sqrt{\pi}}{\sqrt{2}}\exp\left[\frac{(\delta_\sigma-\delta_\zeta)^2}{2T^2}\right]\right)\mathrm{d}\delta_\zeta=\mathrm{i}T\sqrt{\pi}\,\mathrm{erfi}\left(\frac{\delta_\sigma-\delta_\zeta}{T\sqrt{2}}\right), \end{aligned}$$

[2] Second-photon occupation for the sinusoidal pulse defined in Eq. (2.46) is given by

$$\begin{aligned} a^{[2]}(E_j)=-\frac{1}{8}A_0^2T^2\pi\sum_k d_{jk}d_{k0}\sum_{l',l}\mathrm{J}_{l'}(a)\mathrm{J}_l(a)\,\mathrm{e}^{\mathrm{i}[l\omega_{k0}+l'\omega_{jk}]\tau-\mathrm{i}[l\zeta+l'\sigma]\phi} \\ \times\,\mathrm{e}^{-(\delta_\zeta^2+\delta_\sigma^2)/4}\left(1+\mathrm{i}\,\mathrm{erfi}\left(\frac{\delta_\sigma-\delta_\zeta}{2\sqrt{2}}+\mathrm{i}\frac{\tau[l-l']}{\sqrt{2}T}\right)\right). \end{aligned}$$

in most cases of pulse shaping, such an exact solution is not available. Hence, we utilize the technique of slowly-varying-envelope-approximation (SVEA) [120, 121] to derive a general solution.

4.3.1 Slowly varying envelope approximation

We consider a general form of the vector potential given by Eq. (2.38), in which $f(t)$ and $\exp[\mathrm{i}\Phi(t)]$ vary slowly compared to the laser frequency ω, i.e., $\partial^m f(t)/\partial t^m \ll \omega^m$ and $\partial^m \Phi(t)/\partial t^m \ll \omega^m$ for all integer m. In second-order perturbation theory given by Eq. (4.24), we make the approximation

$$\begin{aligned}\int_{-\infty}^{t} \mathrm{d}t' \, \exp\left(\mathrm{i}\omega_{k0}t'\right) A(t') &= \frac{1}{2}\sum_{\zeta=\pm1}\int_{-\infty}^{t} \mathrm{d}t' \, f(t') \exp\left[-\mathrm{i}\zeta\Phi(t')\right] \exp\left[\mathrm{i}\left(\omega_{k0}-\zeta\omega\right)t'\right], \\ &\approx -\frac{\mathrm{i}}{2} f(t) \sum_{\zeta=\pm1} \exp\left[-\mathrm{i}\zeta\Phi(t)\right] \frac{\exp(\mathrm{i}\omega_{k0}t)}{\omega_{k0}-\zeta\omega},\end{aligned} \tag{4.31}$$

where we have used the integration by parts and neglected terms of order $\partial^m f(t)/\partial t^m$ and $\partial^m \Phi(t)/\partial t^m$ for all m. The integer ζ corresponds to one photon absorption if $\zeta = +1$ and one photon emission if $\zeta = -1$. Substituting this equation into Eq. (4.24), one obtains

$$a^{[2]}(E_j) \approx \frac{\mathrm{i}}{4\hbar^2}\mathcal{A}_0^2 \sum_k d_{jk}d_{k0} \sum_{\substack{\zeta=\pm1 \\ \sigma=\pm1}} \frac{1}{\omega_{k0}-\zeta\omega} \int_{-\infty}^{\infty} \mathrm{d}t \; f^2(t) \mathrm{e}^{\mathrm{i}(\omega_{j0}-(\zeta+\sigma)\omega)t} \exp\left[-\mathrm{i}(\zeta+\sigma)\Phi(t)\right], \tag{4.32}$$

where we have used $\omega_{jk} + \omega_{k0} = \omega_{j0}$. Equation (4.32) can be written with the Fourier transform as

$$a^{[2]}(E_j) \approx \frac{\mathrm{i}}{4\hbar^2}\mathcal{A}_0^2 \sum_k d_{jk}d_{k0} \sum_{\substack{\zeta=\pm1 \\ \sigma=\pm1}} \frac{1}{\omega_{k0}-\zeta\omega} \mathcal{F}\Big[f^2(t)\mathrm{e}^{-\mathrm{i}(\zeta+\sigma)\Phi(t)}\Big]\Big(\omega_{j0}-(\zeta+\sigma)\omega\Big). \tag{4.33}$$

An electron in the ground state of the atom $|i\rangle = |0\rangle$ can only couple with states of energy larger than the energy of the ground state, i.e., $\omega_{k0} \geq 0$ for all k. If the atom is initially in its ground state, $|0\rangle = |E_0\rangle$ with energy E_0, the electron can only absorb one photon, and as a consequence, the only possible value for ζ is $\zeta = 1$. Therefore

$$a^{[2]}(E_j) \approx \frac{\mathrm{i}}{4\hbar^2}\mathcal{A}_0^2 \Big\{ \mathcal{F}\left[f^2(t)\right](E_j - E_0) + \mathcal{F}\left[f^2(t)e^{-2\mathrm{i}\Phi(t)}\right](E_j - E_0 - 2\omega) \Big\} \sum_k \frac{d_{jk}d_{k0}}{\omega_{k0}-\omega}, \tag{4.34}$$

where the first term is for $\sigma = +1$ and the second term is for $\sigma = -1$.

Equation (4.34) describes the two-photon amplitude for a general pulse. Now we can consider it for a Gaussian pulse with the envelope of $f(t) = \exp[-t^2/T^2]$, and $\Phi(t) = 0$ which is given by

$$a^{[2]}(E_j) \approx \frac{\mathrm{i}}{4\hbar^2}\sqrt{\frac{\pi}{2}}T\mathcal{A}_0^2\left\{\mathrm{e}^{-(E_j-E_0)^2T^2/8} + \mathrm{e}^{-(E_j-E_0-2\omega)^2T^2/8}\right\}\sum_k \frac{d_{jk}d_{k0}}{\omega_{k0}-\omega}. \tag{4.35}$$

If we compare Eq. (4.35) with the exact expression in Eq. (4.30), we immediately find out that the first term in Eq. (4.30) is missing. With the asymptotic behavior of the Dawson function, $F(x) \sim 1/2x$ in the second term of Eq. (4.30), we reach Eq. (4.35). The variable $\delta_\sigma = (\omega_{jk} + \sigma\omega)\,T/2$ does not show up in the denominator in Eq. (4.35) since we used SVEA in 1st-order PT, and we missed it as it comes from the 1st-order PT.

As long as the Fourier transform of the laser pulse and the Fourier transform of the laser pulse shifted by 2ω do not overlap, the term $\mathcal{F}[f(t)^2](\omega_{j0})\mathcal{F}[f(t)^2\exp[-2\mathrm{i}\Phi(t)]](\omega_{j0}-2\omega)$ is negligible. As a consequence, the photoelectron energy distribution (PED) $P(E)$ is given by

$$\begin{aligned} p(E_j) &\approx \left|a^{[1]}(E_j)\right|^2 + \left|a^{[2]}(E_j)\right|^2 \approx \frac{1}{\hbar^2}\left|\mathcal{A}_0\mathcal{F}\left[f(t)e^{-\mathrm{i}\Phi(t)}\right](E_j-E_0-\omega)d_{j0}\right|^2 \\ &+\frac{1}{16\hbar^4}\left\{\left|\mathcal{A}_0^2\mathcal{F}\left[f^2(t)e^{-2\mathrm{i}\Phi(t)}\right](E_j-E_0-2\omega)\right|^2 + \left|\mathcal{A}_0^2\mathcal{F}\left[f^2(t)\right](E_j-E_0)\right|^2\right\}\left|\sum_k \frac{d_{jk}d_{k0}}{E_k-E_0-\omega}\right|^2. \end{aligned} \tag{4.36}$$

The dominant term in the summation over k is the state of energy E_1, which corresponds to the intermediate single-photon absorption of energy $E_1 = E_0 + \hbar\omega$. The PEDs of the system will consist of three main parts, which correspond to the three main terms on the right side of the latter equation:

- The first term corresponds to the single-photon process. The electron absorbs one photon and ends in the final energy level $E_j \approx E_0 + \omega$ where ω is the central frequency of the fast-oscillating part. The PED corresponds to the Fourier transform of the laser pulse envelope $f(t)e^{-\mathrm{i}\Phi(t)}$ shifted by $E_0 + \omega$.

- The second term corresponds to the two-photon process. The electron absorbs one photon and goes to the intermediate energy level $E_1 = E_0 + \omega$, then absorbs a second photon and ends in the final energy level $E_j \approx E_0 + 2\omega$. The PED corresponds to the Fourier transform of the pulse envelope squared $f^2(t)\mathrm{e}^{-2\mathrm{i}\Phi(t)}$ centered around $E_0 + 2\omega$.

- The third term corresponds to the two-photon (or zero-photon) process. The electron absorbs one photon and goes to the intermediate energy level $E_1 = E_0 + \omega$, then emits a photon through stimulated emission and ends in the final energy level $E_j \approx E_0$. The

PED corresponds to the Fourier transform of the pulse envelope squared $f^2(t)$ centered around E_0.

It is worth mentioning that the two-photon PED, which is the Fourier transform of the square pulse envelope, has a slightly broader width than the single-photon PED, and higher orders are likewise affected by it. Equation (4.36) can be understood by looking at the schematic diagram depicted in Fig. 4.7.

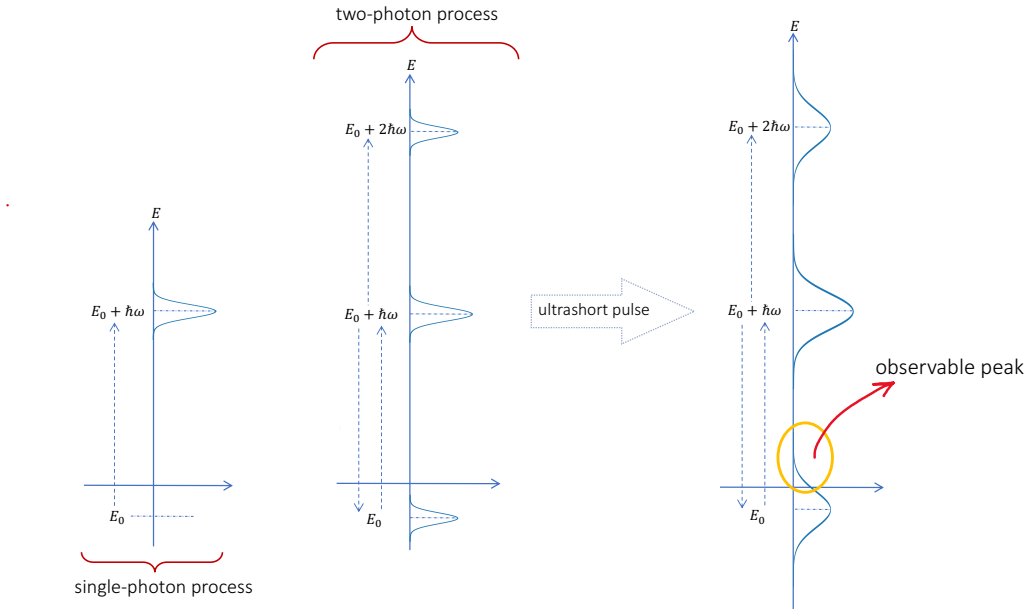

Figure 4.7: A diagram of the multiphoton process, in particular the single- and two-photon processes, is drawn. The vertical arrow indicates the energy, and the horizontal axis is the ionization threshold (zero energy). In the two-photon process, there are two pathways: (i) two-photon absorption and (ii) one-photon absorption and emission, which correspond to the zero-photon process for electrons interacting with a laser pulse. The spectrum is inclined to zero at low energies, $E \approx 0$, due to the tendency of the matrix element to zero, and as a result, an independent peak is observed in the calculation.

4.3.2 Zero-photon transition

The direct effect of ultrashort pulses observes in low energy in the sketch in Fig. 4.7 is considered to be zero-photon. Figure 4.8 reveals that by going to longer pulses, this low-energy effect disappears.

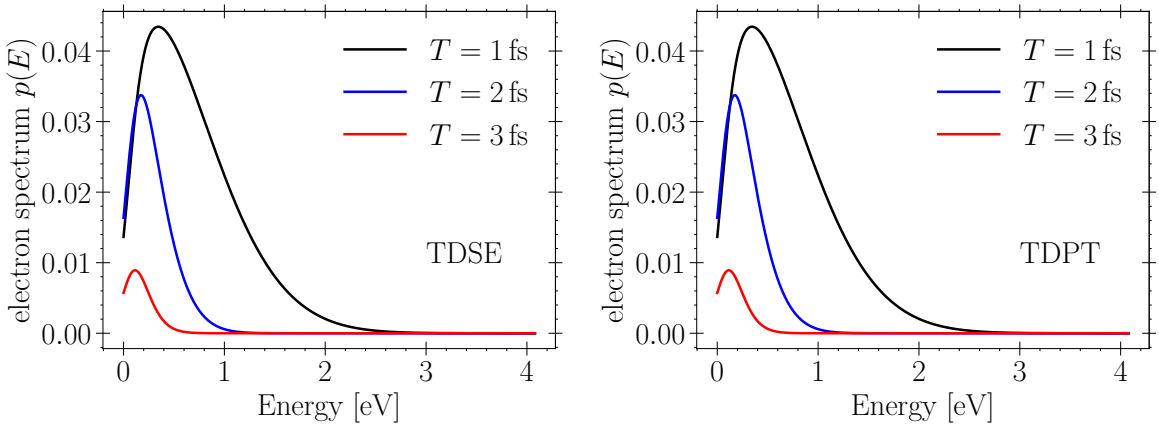

Figure 4.8: The net zero-photon photoelectron spectrum for a Gaussian pulse with different pulse duration $T = 1, 2$, and 3 fs, carrier frequency $\omega = 0.314$ a.u., and field strength $\mathcal{A}_0 = 0.5$ a.u. Left panel, the result is for TDSE and right panel for TDPT.

The zero-photon process exhibits certain characteristics, which we shall outline here. (1) It is a consequence of ultrashort pulses; therefore, in order to study this process, it is necessary to subject it to such pulses. (2) For this process, an initial state with low energy is of great importance. If the initial state is close to the threshold, the process is evident. Whereas if the initial state is deep, it is difficult to observe even if the pulse is strong or of short duration. (3) When an atom is subjected to a strong field, atomic states experience a shift, which is equivalent to the dynamic Stark shift. This gives rise to increasing the ionization in this process. The shift in atomic states is effective in this process if conditions (1) and (2) are already fulfilled.

The model system that we consider here is a one-dimensional system with the potential [132]

$$V(x) = -\frac{\exp\left[-a_1\sqrt{(x/a_1)^2 + a_2^2}\right]}{\sqrt{(x/a_1)^2 + a_3^2}}, \tag{4.37}$$

with $a_1 = 24.856, a_2 = 0.16093$, and $a_3 = 0.25225$, it supports one bound state of $E_0 = -0.0277$ a.u. This potential has a weak bound state, this property makes it suitable to investigate the zero-photon process.

Although Eq. (4.30) provides a solution for a Gaussian pulse, we are interested in finding a model for a general laser pulse and understanding the behavior of this process. For that matter, we use SVEA which is described in the section 4.3.1.

A model

The photoelectron peak that is observed at low energy is attributed, see Fig. 4.8, to non-adiabatic photo-ionization (NAPI). In the frequency domain, as shown in Fig. 4.7, this mechanism is a two-photon process with absorption and emission of one photon. The amplitude for this zero net photon process can be formulated in second-order time-dependent perturbation theory. Evaluated in SVEA is reads

$$a^{[2]}(E_j) \approx \frac{\mathrm{i}}{4\hbar^2}\mathcal{A}_0^2\, d_j^{[2]}\, \mathcal{F}\left[f^2(t)\right](E_j - E_0)\,, \tag{4.38}$$

which is proportional to the Fourier transform of the square of the pulse envelope, with the matrix-element

$$d_j^{[2]} = \sum_k d_{jk} d_{k0} \frac{2\omega_{k0}}{\omega_{k0}^2 - \omega^2}. \tag{4.39}$$

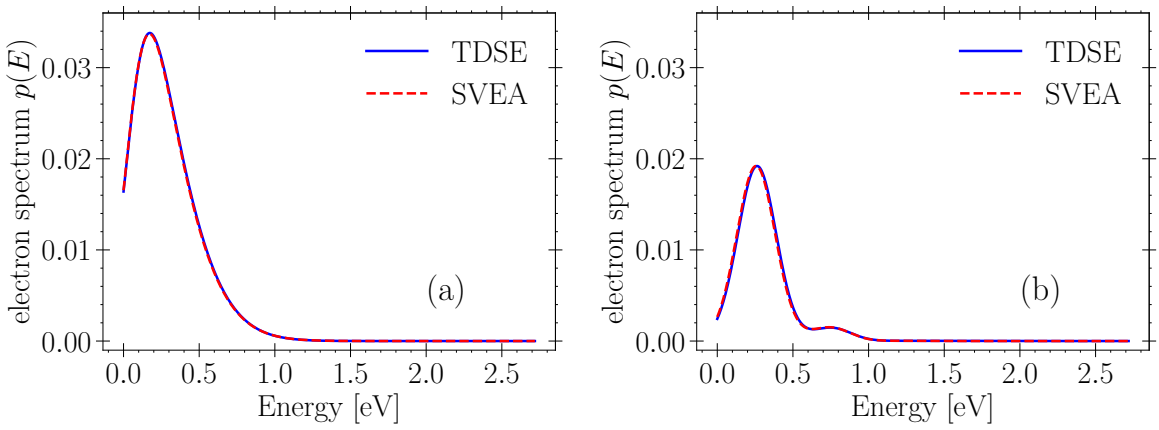

Figure 4.9: Photoelectron spectra for two different pulses, (a) a Gaussian pulse and (b) a pulse train defined in Eq. (2.46), with pulse parameters $\omega = 0.314\,\mathrm{a.u.}, T = 2\,\mathrm{fs}, \mathcal{A}_0 = 0.5\,\mathrm{a.u.}$ and the modulated spectral phase parameters $a = 1, \tau = 4T, \phi = 0$. Shown is the solution of TDSE (solid blue line) and the SVEA approximation in (Eq. (4.38), dashed red line).

Figure 4.9 shows a comparison between TDSE and Eq. (4.38) for two pulses, the Gaussian and sinusoidal pulse, Eq. (2.46). In the SVEA approximation Eq. (4.38), some prefactors are missing; therefore, we have to normalize the SVEA results to compare with the TDSE solution. The small peak in Fig. 4.9b is due to the interference between the sub-pulses and is controlled by τ. The sinusoidal pulse, Eq. (2.46), is depicted in Fig. 2.4. For $\tau = 4T = 8\,\mathrm{fs}$, and $a = 1$ sub-pulses are well separated and contain 9 sub-pulses, each of them has an intensity

proportional to the Bessel function $J_k(a)$ where $J_{0\ldots4}(1) \approx \{0.765, 0.440, 0.115, 0.020, 0.002\}$. The interference between the middle sub-pulses leads to raising and falling structures in the photoelectron spectrum. Since a part of the zero-photon spectrum appears in the continuum, we only can see a visible small peak in Fig. 4.9. However, in the case of the net two-photon ionization, we can observe many peaks in its spectrum, see Fig. 4.10.

In general, zero-photon ionization depends on the square of the pulse envelope. However, since $\zeta + \sigma = 0$, the factor $\mathrm{e}^{-\mathrm{i}(\zeta+\sigma)\Phi(t)}$ vanishes in Eq. (4.38), and as a result, this process is independent of the phase information of the laser pulse. Fig. 4.10 illustrates this

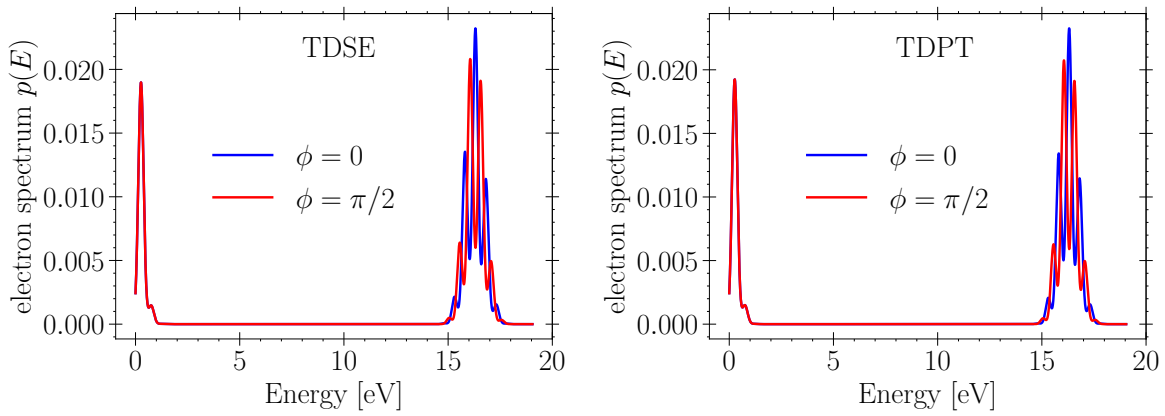

Figure 4.10: The zero- and two-photon photoelectron spectrum for the same model as in Fig. 4.9 for the sinusoidal pulse, Eq. (2.46), with pulse parameters of $\omega = 0.314\,\mathrm{a.u.}, T = 2\,\mathrm{fs}, \mathcal{A}_0 = 0.5\,\mathrm{a.u.}$ and the modulated spectral phase parameters of $a = 1$ and $\tau = 4T$ for $\phi = 0$ (blue line) and $\phi = \pi/2$ (red line). TDSE (left panel) and TDPT (right panel) produce the same result.

well, demonstrating how the two-photon ionization strongly depends on the pulse's phase, whereas the zero-photon ionization does not, as predicted from second-order TDPT. Here, the modulation phase ϕ is the relative phase between subpulses, see Chapter 3.

4.3.3 Zero-photon ionization probability

Zero-photon ionization is effectively a two-photon process, which is a new channel in the photoionization process. This new peak has a different trend for the ionization probability as a function of laser intensity in comparison with other multiphoton processes, as can be seen in Fig. 4.11. The ionization probability can be calculated by integrating the area under each photon peak at different intensities. Figure 4.5, shows the ATI peaks and the area under

each peak separated by different colors. Thus, the ionization probability in Fig. 4.11 for each photon corresponding to each peak in Fig. 4.5. Although the focus of this section is on net two-photon and zero-photon ionization, we also present the result for net single-photon ionization in order to better understand the mechanism.

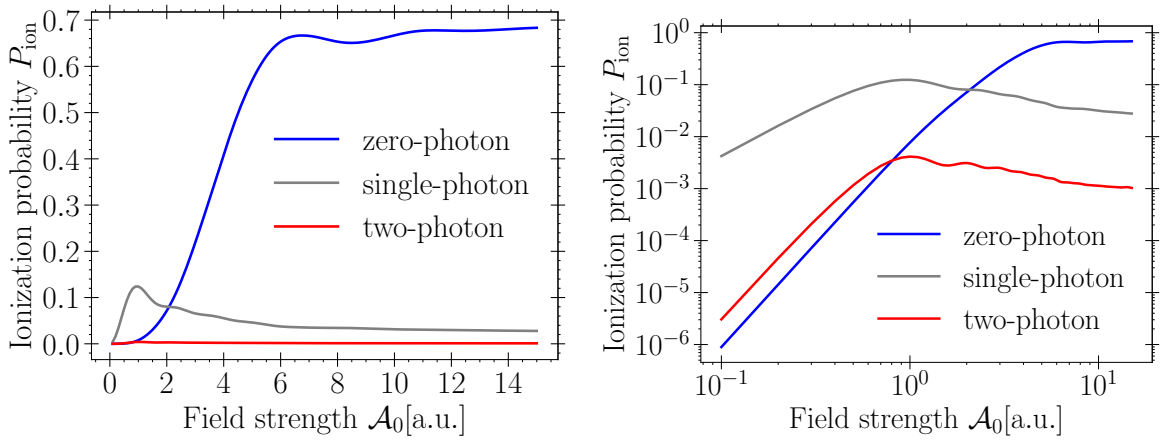

Figure 4.11: TDSE solutions of ionization probabilities for zero- (black line), single- (blue line), and two-photon (red line) transitions for a Gaussian pulse with carrier frequency $\omega = 0.314$ a.u. and pulse duration $T = 2$ fs are given as a function of field strength. the left panel is for linear scale and the right panel is for log scale. The model system is defined in Eq. (4.37).

In the low-intensity limit, the dominant term is the single-photon process, where the system can be described using 1st-order PT, and the ionization probability increases as $\mathcal{A}_0^2$, see Eq. (4.18). As shown in Fig. 4.11, single- and two-photon ionization after a certain point, also known as the critical field, starts to have a decreasing trend, while zero-photon ionization at that point starts to have an increasing trend.

The slowly varying envelop approximation reveals unique properties of the zero-photon ionization probability at high intensity. To this end, we restrict ourselves to the block of pathways that produces net zero-photon absorption.

Using the fact that higher-order pathways have a small matrix element and contribute less to the ionization probability we can restrict ourselves to the block in Fig. 4.12, and calculate the matrix element for every order which ends net zero-photon absorption. For instance, we can calculate the four-photon matrix element of one path, that is "up-down-up-down" or $E_0 \to E_k \to E_l \to E_m \to E_j$, where E_k, E_l, and E_m are intermediate states and E_j is the

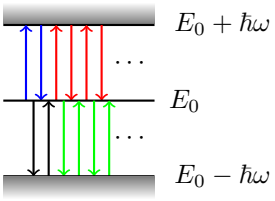

Figure 4.12: A possible block of pathways that reach the net zero-photon transition, two-photon (blue and black), and four-photon (red and green)

final state, as

$$d_j^{[4]} = \lim_{\epsilon\to 0^+} \sum_m \sum_l \frac{d_{jm} d_{ml} d_l^{[2]}}{(\omega_{m0} - \omega)(\omega_{l0} + \mathrm{i}\epsilon)}, \tag{4.40}$$

where $d_l^{[2]}$ is defined in Eq. (4.39). There is a singularity at $E_m = E_0 + \omega$ and at $E_l = E_0$ in the integral of intermediate states in Eq. (4.40). We keep one singularity and integrate over the other intermediate state with singularity $E_l = E_0$.

Using the Cauchy principle value and the fact that it has a principle value (PV), we have

$$\lim_{\epsilon\to 0^+} \int \mathrm{d}E \frac{g(E)}{E - E_0 + \mathrm{i}\epsilon} = \mathrm{PV}\left(\frac{g(E)}{E - E_0}\right) - \mathrm{i}\pi \int \mathrm{d}E\ \delta(E - E_0) g(E). \tag{4.41}$$

Ignoring the principle value [110] and using $\int \mathrm{d}x\ g(x)\delta(x - x_0) = g(x_0)$, the integration in Eq. (4.40) can be performed. The fourth-order matrix element becomes $d_j^{[4]} \approx \left(-\mathrm{i}\, d_0^{[2]}\right) d_j^{[2]}$, where $d_j^{[2]}$ is defined in Eq. (4.39). The six-photon matrix element can be obtained using the same technique. Thus, in general, the matrix element for every *even* order of PT is given by

$$d_j^{[n]} \approx d_j^{[2]} \left(-\mathrm{i}\, d_0^{[2]}\right)^{\frac{n-2}{2}} \quad \text{for} \quad n = 2, 4, 6, \cdots. \tag{4.42}$$

Using the fact that each *even* TDPT order is the Fourier transform of the squared pulse envelope to the power of that order, $\mathcal{F}[f^{2n}(t)](E - E_j)$, we can obtain the zero-photon probability amplitude by switching the Fourier transform to the integral form as

$$a^{[n]}(E_j) \approx \frac{\mathrm{i}}{\hbar^2} \left(-\frac{1}{2}\right)^n \mathcal{A}_0^n\, d_j^{[n]} \int_{-\infty}^{\infty} \mathrm{d}t\, f^{2n}(t)\, \mathrm{e}^{\mathrm{i}(E_j - E_0)t/\hbar}, \quad \text{for} \quad n = 2, 4, 6, \cdots \tag{4.43}$$

where $d_j^{[n]}$ is the corresponding matrix-element. By substituting Eq. (4.42) into Eq. (4.43), and with $n \to 2n + 2$, we can make sum the contributions for $n = 0, 1, 2, \cdots$, in form of an infinite geometry series, i.e., $\sum_{n=0}^{\infty} ar^n = a/(1 - r)$. Eventually, we achieve at

$$\boxed{a(E_j) = \sum_n a^{[n]}(E_j) \approx \frac{\mathrm{i}}{4\hbar^2}\, \mathcal{A}_0^2\, d_j^{[2]} \int_{-\infty}^{\infty} \mathrm{d}t\, \frac{f^2(t)\, \mathrm{e}^{\mathrm{i}(E_j - E_0)t/\hbar}}{1 - \mathrm{i}\, d_0^{[2]}\, f^2(t)\, \mathcal{A}_0^2/4}}. \tag{4.44}$$

For low intensity, higher matrix elements are negligible and Eq. (4.44) turns into Eq. (4.38), as expected.

In the case of high intensity, the PED is expressed by $p(E) = |a(E)|^2$ and the zero-photon ionization probability $P_{\text{ion}} = \int \mathrm{d}E\, p(E)$ for this limit tends to 1.

4.3.4 Oscillation in zero-photon transition

As ATI peaks are generated by an intense short pulse, they also get modulated as a result of interference of photoelectron emission in the rising and falling wing of the pulse [131, 133] also found in molecules [134, 135] and termed dynamic interference. Spatial interference, i.e. ionization from different positions of the oscillating potential [118], during the peak of the pulse can be interpreted as the onset of stabilization. The number of oscillations rises as going to higher intensity.

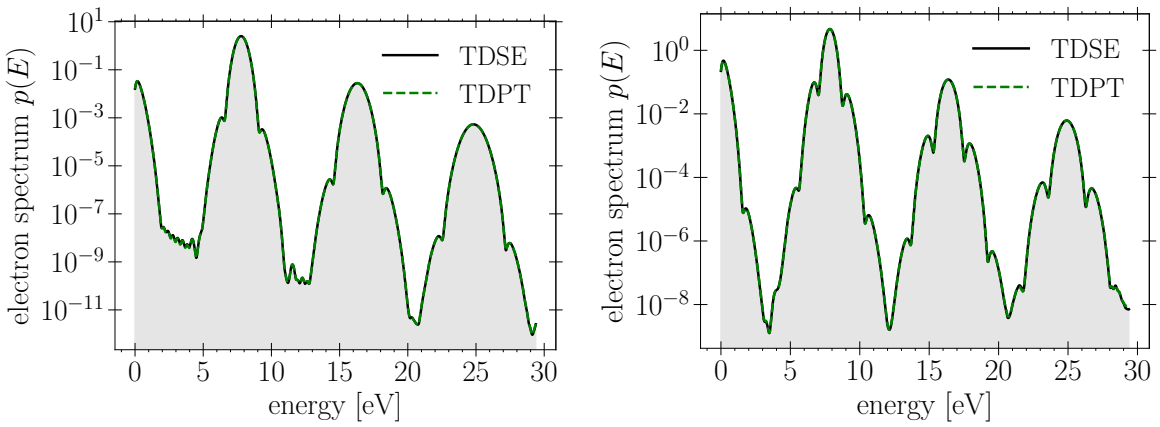

Figure 4.13: TDSE solution of the photoelectron spectra (ATI peaks) up to energies corresponding to 3-photon in logarithmic scale for a Gaussian envelope with a central frequency $\omega_0 = 0.314\,\text{a.u.}$, and a pulse duration $T = 2\,\text{fs}$ for two different field strengths (a) $\mathcal{A}_0 = 0.5\,\text{a.u.}$ and (b) $\mathcal{A}_0 = 1\,\text{a.u.}$. As can be seen, oscillations in ATI peaks grow at a higher intensity. These results are for a one-dimensional solution with the potential defined in Eq. (4.37).

Figure 4.13 shows ATI peaks up to energies corresponding to 3-photon. For high intensity, we can see the photoelectron spectrum, Eq. (2.26), of ATI peaks get modulated in the single-, 2-,3-, and 4-photon and also in the low energy peak, zero-photon ionization. We found that the reason for the oscillations in the zero-photon is similar to those in other peaks, namely, single- and two-photon processes.

To this end, two alternative paths were considered reaching net zero-photon ionization,

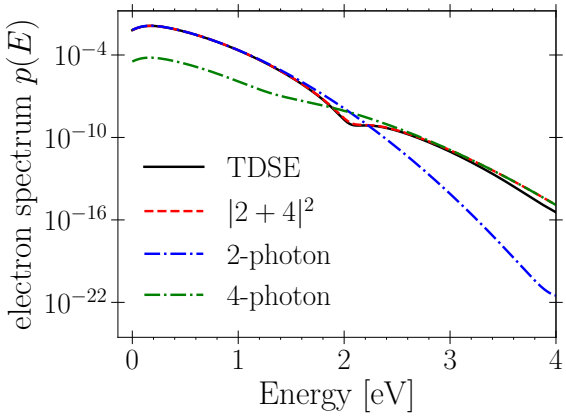

Figure 4.14: Photoelectron spectra of zero-photon transition in a logarithmic scale for the Gaussian envelope with a central frequency $\omega_0 = 0.314\,\text{a.u.}$, a pulse duration $T = 2\,\text{fs}$ and the field strength $\mathcal{A}_0 = 1\,\text{a.u.}$. The interference of two- and four-photon transitions (dashed red line) covers the small dip around $E \sim 2\,\text{eV}$ in the TDSE solution (solid black line). Here, the system is identical to that shown in Fig. 4.13.

each requiring a different number of photons. Two- and four-photon processes are taken into account in this. The outcome of their interference with one another is an oscillation in the spectrum, as shown in Fig. 4.14, which gives rise to so-called "interference stabilization" [19, 20]. These oscillations may lead to an increase in the ionization probability in the zero-photon ionization, and in the case of other ATI peaks, they may lead to a decrease in the ionization probability, see Fig. 4.11.

4.4 Application II: interference stabilization

Atomic stabilization is a strong-field effect in the short-wavelength regime. The ionization rate does not follow I^n, with n number of the absorbed photon, which is predicted by the perturbation theory, but shows a decreasing trend (possibly in an oscillatory manner) with increasing laser intensity I, see the right panel in Fig. 4.15. This expresses the fact that the ionization probability at the end of a laser pulse of fixed shape and duration does not approach unity as the peak intensity increases but either starts decreasing with the intensity (possibly in an oscillatory manner) or flattens out at a value smaller than unity [118]. This phenomenon typically requires the photon energy $\hbar\omega$ to be larger than the ionization potential I_p. It was first discovered by theoretical calculations [129, 130] and later confirmed by a few experiments performed on Rydberg atoms [136, 137, 138, 139]. The interested reader who

wishes to gain a deeper understanding is referred to Ref. [118]. It is also worth mentioning that these theoretical studies are in the dipole approximation, and the non-dipole terms do not destroy the stabilization effect [140].

The stabilization process has been explained in the time domain. However, we found that it can be understood by going to the frequency domain and taking advantage of the TDPT. In this domain, stabilization may be explained by the interference of different electron pathways that reach the same final energy.

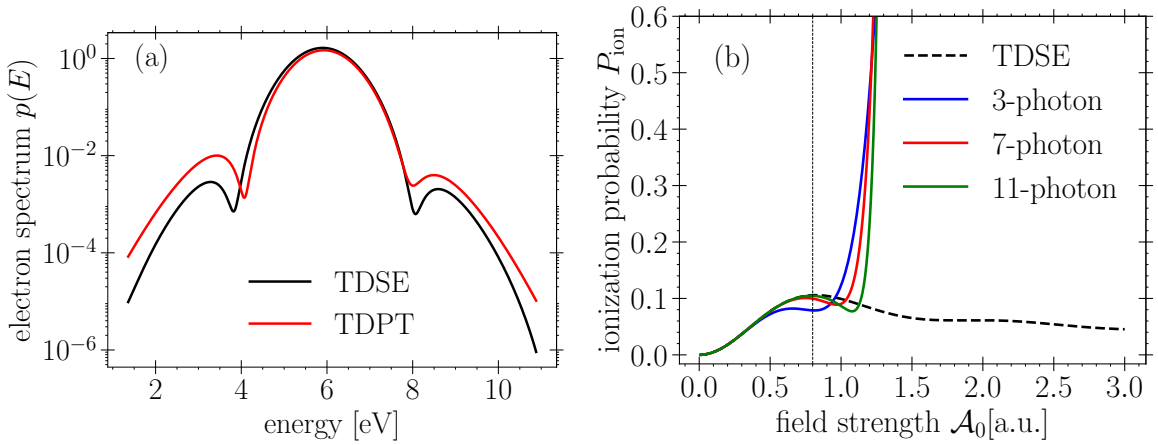

Figure 4.15: Atomic stabilization. (a) The photoelectron spectrum of photon ionization for a Gaussian pulse, Eq. (2.41) with parameters of the pulse duration of 1 fs, the central frequency of $\omega = 6.8\,\text{eV}$ and the field strength of $\mathcal{A}_0 = 0.6\,\text{a.u.}$. (b) A comparison between the results of 3rd-order PT and TDSE solutions for ionization as a function of field strength, with a critical field strength of $\mathcal{A}_c = 0.8\,\text{a.u.}$ where the ionization probability reaches the maximum value. The result of PT labeled "3-photon" implies the coherent summation of single-photon and three-photon contributions, which are obtained from 1st-order PT and 3rd-order PT, respectively. The other results are also obtained accordingly. The system is a 1D model with potential defined in Eq. (4.37).

The single-photon electron spectrum is generated by an intense short pulse, and it gets modulated as a result of interference of photo-electron emission in the rising and falling wing of the pulse. This interference effect appears in the electron spectrum as an oscillation pattern. Spatial interference, i.e., ionization from different parts of the pulse can be interpreted as the onset of stabilization. In the frequency domain, these oscillations in the single-photon spectrum start in the 3rd-order perturbation theory. As explained in sections 4.2, and 4.3.1, the single-photon ionization obtained from 1st-order PT is the Fourier transform of the pulse

envelope, and from 3rd-order PT, it is the Fourier transform of the cubic pulse envelope which is wider. The interference between the 1st- and 3rd-order PT leads to a dip in the rising and falling structure of the electron spectrum, see the left panel in Fig. 4.15.

The interference in the electron spectrum which appears for the first time in a coherent summation of 1st- and 3rd-order PT, is the beginning of the stabilization regime. Therefore, the 3rd-order PT is enough to predict the critical field strength, in which at that certain point the ionization probability inverse the trend and starts to decrease. The right panel in Fig. 4.15 shows the ionization probability for coherent summation of pathways from different orders of PT which reach net single-photon ionization. As can be seen, up to 3rd-order pathways are enough to predict the critical field strength $\mathcal{A}_c$. By adding more pathways from different orders of PT, the result approaches the ionization probability calculated from the TDSE solution.

Since the critical field strength does not depend on pulse duration, we can safely employ the SVEA approximation to predict it.

4.4.1 Third-order time-dependent perturbation theory

The number of pathways in 3rd-order PT, as explained in section 4.2, is $2^3 = 8$. Among these eight pathways, three end the net single-photon energy level, as shown in the sketch in Fig. 4.16.

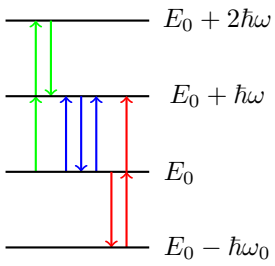

Figure 4.16: All possible three-photon process pathways that end net single-photon energy level.

In order to calculate 3rd-order PT, we take advantage of SVEA. Initiate by inserting the integral form of Eq. (4.32) into Eq. (4.16) for 3rd-order PT, we obtain

$$a^{[3]}(E_j) \approx \frac{\mathrm{i}}{4\hbar^3} \sum_{\zeta,\sigma,\eta=\pm1} \sum_{l,k} \frac{d_{jl} d_{lk} d_{k0}}{\omega_{k0} - \zeta\omega} \mathcal{A}_0^3 \int_{-\infty}^{\infty} \mathrm{d}t\, f(t)\, \mathrm{e}^{\mathrm{i}(\omega_{jl} - \eta\omega)t}\, \mathrm{e}^{-\mathrm{i}\eta\Phi(t)} \times \int_{-\infty}^{t} \mathrm{d}t'\; f^2(t')\, \mathrm{e}^{\mathrm{i}(\omega_{l0} - (\zeta+\sigma)\omega)t'}\, \mathrm{e}^{-\mathrm{i}(\zeta+\sigma)\Phi(t')}. \tag{4.45}$$

We assume that the envelope $f(t)$ and $e^{-\mathrm{i}\Phi(t)}$ vary slowly compared to the laser frequency, then we can make an approximation in the second integral in Eq. (4.45), and solve it as we did in Eq. (4.31). Therefore, the three-photon amplitude in SVEA for all possible pathways in Fig. 4.16 is given by

$$a^{[3]}(E_j) \approx -\frac{\mathrm{i}}{8\hbar^3}\,\mathcal{A}_0^3\,d_j^{[3]}\,\mathcal{F}\left[f^3(t)\mathrm{e}^{-\mathrm{i}\Phi(t)}\right](E_j - E_0 - \omega)\,, \tag{4.46}$$

where the matrix element

$$d_j^{[3]} = \sum_{lk} d_{jl}d_{lk}d_{k0}\left(\frac{1}{(\omega_{k0}-\omega)(\omega_{l0}-2\omega)} + \frac{1}{(\omega_{k0}-\omega)\omega_{l0}} + \frac{1}{(\omega_{k0}+\omega)\omega_{l0}}\right). \tag{4.47}$$

The first term in Eq. (4.47) corresponds to the "up-up-down" pathway, two-photon absorption, and one photon emission. The second term corresponds to the "up-down-up" pathway, and the last term corresponds to the "down-up-up" pathway.

As briefly mentioned in this section, we can study stabilization using three-photon pathways for single-photon ionization to understand this process's mechanism in the frequency domain.

4.4.2 Ionization probability and stabilization

Considering the whole pathway that reaches the net single-photon up to the three-photon, the photoelectron spectrum (PED) for single-photon ionization (SPI) using first- and third-order TDPT Eq. (4.46) and Eq. (4.17) for the Gaussian pulse is given by

$$\begin{aligned} p(E_j) &= |a^{[1]}(E_j) + a^{[3]}(E_j)|^2 \\ &\approx \frac{1}{4\hbar^2}\mathcal{A}_0^2\,|d_{j0}|^2\,T^2\,\pi\,\mathrm{e}^{-(\omega_{j0}-\omega)^2T^2/2} + \frac{1}{8^2\hbar^6}\mathcal{A}_0^6\,T^2\,\frac{\pi}{3}\,|d_j^{[3]}|^2\,\mathrm{e}^{-(\omega_{j0}-\omega)^2T^2/6} \\ &\quad + \frac{1}{8\hbar^4}\mathcal{A}_0^4\,d_{j0}d_j^{[3]}\,T^2\,\frac{\pi}{\sqrt{3}}\,\mathrm{e}^{-(\omega_{j0}-\omega)^2T^2/3}. \end{aligned} \tag{4.48}$$

We can calculate the ionization probability that is provided by

$$P_{\mathrm{ion}}(\mathcal{A}_0) = \int \mathrm{d}E\,p(E) \approx \mathcal{A}_0^2\,\mathrm{A} + \mathcal{A}_0^6\,\mathrm{B} + \mathcal{A}_0^4\,\mathrm{C}, \tag{4.49}$$

where A, B and C are independent of intensity and given by

$$\begin{aligned} \mathrm{A} &\equiv \frac{1}{2^2\hbar^2}\,T^2\,\pi\int \mathrm{d}E\,|d_{j0}|^2\,\mathrm{e}^{-(E-E_1)^2T^2/2}, \\ \mathrm{B} &\equiv \frac{1}{2^3\hbar^6}\,T^2\,\frac{\pi}{3}\int \mathrm{d}E\,|d_j^{[3]}|^2\,\mathrm{e}^{-(E-E_1)^2T^2/6}, \\ \mathrm{C} &\equiv \frac{1}{2^2\hbar^4}\,T^2\,\frac{\pi}{\sqrt{3}}\int \mathrm{d}E\,d_{j0}d_j^{[3]}\,\mathrm{e}^{-(E-E_1)^2T^2/3}. \end{aligned} \tag{4.50}$$

where $E_1 = E_0 + \hbar\omega$. The sign of these constants are $\mathrm{A}, \mathrm{B} > 0$, and $\mathrm{C} < 0$. The sign of C has to be negative to have interference, otherwise, the ionization probability is monotonically increasing.

For long pulses, $T \gg 1$, the matrix elements $d_j^{[3]}$ and d_{j0} in Eq. (4.50) do hardly change over the frequency range near $\omega = \omega_{j0}$, they can be taken out the integrals. Therefore, we can calculate integrals in Eq. (4.49) as

$$\mathrm{A} = \frac{1}{4\hbar^2} T\pi\sqrt{2\pi}|d_{E_1}|^2, \quad \mathrm{B} = \frac{1}{8^2\hbar^6} T\pi/3\sqrt{6\pi}|d_{E_1}^{[3]}|^2, \quad \mathrm{C} = \frac{1}{8\hbar^2} T\pi\sqrt{\pi} d_{E_1} d_{E_1}^{[3]}. \tag{4.51}$$

Since the sign of $\mathcal{A}_0$ does not matter, thus we may assume $\mathcal{A}_0 > 0$. With the help of Eq. (F.1), we finally get for Eq. (4.49)

$$P_{\mathrm{ion}}(I) \approx \mathrm{A}\, I + \mathrm{B}\, I^3 + \mathrm{C}\, I^2. \tag{4.52}$$

To achieve the critical field strength, we should maximize the ionization probability

$$\frac{\mathrm{d}P(I)}{\mathrm{d}I}\Big|_{I_\mathrm{c}} = \mathrm{A} + 3\,\mathrm{B}\, I_\mathrm{c}^2 + 2\,\mathrm{C}\, I_\mathrm{c} = 0. \quad I > 0 \tag{4.53}$$

Hence, the ionization probability reaches its maximum value at

$$I_\mathrm{c} = \sqrt{\frac{\mathrm{C}^2}{9\mathrm{B}^2} - \frac{\mathrm{A}}{3\mathrm{B}}} - \frac{\mathrm{C}}{3\mathrm{B}} \approx 2\,\frac{d_{E_1}}{d_{E_1}^{[3]}}, \tag{4.54}$$

independent of the pulse duration T.

To conclude this section, for laser amplitude $\mathcal{A}_0 < \mathcal{A}_\mathrm{c}$, the ionization probability increases as increasing laser amplitude as $\mathcal{A}_0^2$, see Eq. (4.18), and the dominant term is single photon absorption. For $\mathcal{A}_0 > \mathcal{A}_\mathrm{c}$ the single-photon ionization probability decreases, and the dominant term is the zero-photon process, see Fig. 4.11. This is the *stabilization regime*. In this regime, we expect higher-order corrections in the perturbation theory to contribute more to the photoelectron energy distribution. Therefore, I_c predicted from Eq. (4.54) is only an approximation.

When the third-order term becomes non-negligible, there are interferences between the three-photon and single-photon processes. When the fourth-order term becomes non-negligible, there is interference between the four-photon and two-photon processes (in particular in the zero-photon region). When these terms become non-negligible, we begin to see oscillations in the PED as a function of laser amplitude because Eq. (4.48) now has more terms that contribute of a higher order in $\mathcal{A}_0$, as shown in Fig. 4.13.

4.5 Summary

In the regime of ultrashort pulses, the pulse envelope plays a crucial role in the convergence of TDPT, in which the FWHM of the pulse. Furthermore, we observed that the TDPT is independent of phase modulation; as a result, for ultrashort pulses, the same TDPT order is required as for a Fourier-limited pulse. In addition, non-adiabatic ionization can be interpreted as a zero-photon process, which the second-order TDPT can describe. By considering the third-order TPDT, we identified the critical strength field and explained the interference stabilization in the frequency domain.

Despite the fact that perturbation theory is an old topic, one can still derive some interesting features in different regimes. A special emphasis should be placed on the ultrashort regime, which demonstrates some notable applications that contribute to understanding the strong field phenomenon in the frequency domain.

Chapter 5

Molecular Photoionization Time Delay

5.1 Preface

Time plays a peculiar role in quantum mechanics. It is considered as a crucial parameter in the dynamical evolution [141] other than as a quantum observable associated with a Hermitian operator. However, there are controversial questions connected with the definition of a time observable [142, 143, 144]. Time delay refers to a measure of the time it takes for a wavepacket to travel through an interaction region and interact with the system. Time delay can be estimated as the difference in arrival time at a given point in space compared to a reference arrival time which, by definition, corresponds to a situation with zero delay or, equivalently, zero advance [145]. Time delay is used to study quantum scattering, resonances [146, 147], and quantum chaos [148]. Early results on time delay were based on Kelvin's Principle of Stationary Phase [149, 150], often employed to derive the group velocity of a wavepacket [151]. Later, it was a kind of motivation for Eisenbud [152] and Wigner [27] to study the time delay in quantum-mechanical scattering wavepacket. The theory of time delay has been investigated in two concepts, in terms of displacement of the "center" of the wavepacket [152, 27, 153, 154, 155, 156]. Although this concept has different meanings for different authors, and in terms of an approach that was proposed by Smith [28] in which he defined it as the difference, for large r, between the time spent by particle within a sphere with radius r of scattering center and the same quantity without interaction [28, 157, 158, 159]. In addition, interest in the study of time delay stimulated experimentalists to measure the duration of quantum collisions [160, 161, 162].

"When does photoemission begin?" This is an editorial title of van der Hart [163], which accompanied the report by Schultze *et al.* [164], that relates the time delay between the absorption of a photon and emission of a photoelectron with rearrangement of the ionic core. Photoionization time delay is a fundamental aspect of the dynamics of photoionization and can provide information about the electronic structure of a system. In simple terms, photoionization time delay is the time it takes for light to knock an electron off a molecule or atom. For over a century, since the Nobel prize-winning work by Einstein [38], atomic photoionization was thought to be an instantaneous process. With the recent advances in attosecond science, measurements of electron dynamics with attosecond time resolution [165] became possible, which has allowed us to resolve this process in time. Thus, the experimental validation of this prediction was realized, for example, time-resolved measurements of electron dynamics and the delay of photoemission [166, 167, 168], which was observed in Helium [169], noble-gas atoms [170, 171, 172, 173, 174], negative ions [175], and condensed matter systems [176, 177, 178] for the single-photon weak field regime. For more details on the attosecond

physics of photoionization, a few reviews are available [179, 180, 181, 182]. It is worth mentioning that photoionization time delay can be measured using a single attosecond XUV pulse in a streaking experiment [183, 184, 185, 186, 187, 168], or using attosecond XUV pulse train in a RABBITT experiment (Reconstruction of Attosecond Beating by Interference of Two-photon Transitions) [188, 189, 190]. The latter has been used to measure photoionization group delay in various molecules: N_2 [191, 192, 193], N_2O [26], CO_2 [194], NO [195] and CF_4 [196, 197].

Attosecond photoionization delays from molecules, the focus of this chapter, have received surprisingly little attention so far, presumably because of the associated experimental and theoretical complexity. However, it is a subject of growing theoretical and experimental interest, for instance, time delay in the process of single-photon ionization of two-center systems [198, 199, 192, 200, 201, 202]. As compared to atomic ionization, the time delays expected from molecular ionization present a much richer phenomenon, with a strong spatial dependence due to the anisotropic nature of the molecular scattering potential. A very detailed theoretical study by Hockett and coworkers in 2016 targeted photoionization delays in small molecules [25]. Examining the emission delay in CO and N_2 molecules, this work provided the first fully three-dimensional photoionization delay maps in the molecular frame and showed the dependence of the emission delay on the electron kinetic energy, the molecular orientation with respect to the light polarization, and the molecular symmetry. Moreover, recently a few measurements of photoionization delays of N_2O and H_2O [26] molecules have been reported.

Here we discuss the theoretical results of angle and energy-resolved time delays in the photoionization of molecules in two domains. (i) The energy domain, in which we formulate the continuum states using some asymptotic solutions and the outgoing boundary condition and utilize the Johnson renormalized Numerov method [29] in order to calculate bound states and continuum states for the coupled-channel Schrödinger equation. (ii) The time domain, in which we examine the wavepacket perspective to study the partial time delay and the ionized electron far from the center. Note that we are only discussing the time delay, in this chapter but not its measurement.

This chapter is structured as follows. In section 5.2, we have an overview of time delay in a scattering process and derive the phase of the scattering states and the expectation value of the wavepacket at a large distance which behaves as a free particle wavepacket. In section 5.3, the photoionization time delay is considered in a scattering approach in which we consider two asymptotic solutions of the scattering state and apply the outgoing boundary condition in order to form the final wavefunction. Having the final wavefunction and initial

state, we can determine the matrix element. The energy derivative of the phase of the matrix element is the photoionization time delay. An anisotropic potential, two-center system with two dimensions model system, is considered to illustrate the photoionization time delay. In section 5.4, we investigate the time delay in the time domain in which we form the wavepacket and consider the incoming and outgoing wavepacket at a large distance from the scattering potential. Then we try to calculate the expectation value. Specifically, the two-center model system is utilized to study the time delay in order to demonstrate this. Lastly, section 5.5 concludes this chapter.

5.2 Introduction to time delay

Early results on time delay were based on the stationary phase, which was employed to derive the group velocity of a wavepacket. Group velocity is a property of waves that describes the velocity at which the wavepackets or groups of waves propagate through a medium. Having a one-dimensional wavepacket [203, 151],

$$\Psi(x,t) = \frac{1}{\sqrt{2\pi\hbar}} \int \mathrm{d}E\, \phi(E)\, \exp\left\{\mathrm{i}kx - \mathrm{i}Et\right\} \tag{5.1}$$

where $\phi(E) = |\phi(E)| \exp[\mathrm{i}\delta(E)]$, with $|\phi(E)|$ peaked around an energy $E = k_0^2/2$ with a wave number k_0, one might try to answer around what value of x would the wave packet $\Psi(x,t)$ be peaked, at a given point of time t. Here E is energy and k is wave number $k = \sqrt{2E}$.

Concerning Eq. (5.1) as a superposition of monochromatic waves, one argues that rapid phase variation will generally lead to destructive interference so that the most favorable situation will occur when k_0 coincides with a point where the phase is stationary i.e. the derivative of the phase vanishes,

$$\frac{\mathrm{d}}{\mathrm{d}k}\left(\delta(E) + kx - \frac{k^2}{2}t\right)_{k=k_0} = 0, \tag{5.2}$$

thus, the wavepacket peaks at

$$x = v_g t - x_0, \tag{5.3}$$

where

$$x_0 = (\mathrm{d}\delta/\mathrm{d}k)_{k=k_0} = v_g\, (\mathrm{d}\delta/\mathrm{d}E)_{k=k_0}\,, \tag{5.4}$$

and the wavepacket is propagating with the group velocity $v_g = (\mathrm{d}E/\mathrm{d}k)_{k_0} = \sqrt{2E}$. The group velocity can be different from the phase velocity, which is the velocity at which the individual waves of the wave packet propagate.

Equation (5.3) describes the peak position of the wavepacket at different stationary points k_0 with a shift in position x_0. In the case of a free particle wavepacket, the peak position is $x = v_g t$, where the shift in position is zero, $x_0 = 0$. Therefore this shift in the peak position of the wavepacket, i.e., Eq. (5.4), is related to the arrival time at a given point in space compared to a reference arrival time which, by definition, corresponds to a situation with zero delay or, equivalently, zero advance. As a result, we can rewrite Eq. (5.3) as

$$x = \sqrt{2E}\,(t - \tau), \tag{5.5}$$

where the offset τ represents the time delay in the wavepacket's arrival at a given point in space relative to the free particle wavepacket. This offset is given by the expression $\tau = \mathrm{d}\delta(E)/\mathrm{d}E$, which denotes the derivative of the phase shift $\delta(E)$ with respect to energy E.

5.2.1 Time delay in scattering scenario

Quantum scattering is the interaction of quantum particles, such as electrons or photons, with a target, resulting in a change in the particle's direction and energy. The behavior of the scattered particles is described by quantum mechanics and can be different from classical scattering due to the wave-particle duality and other quantum phenomena. In simple terms, quantum scattering is the way in which particles "bounce off" of each other and change their behavior when they collide. Fig. 5.1 shows this process, in which the incoming particle with momentum $\vec{k}_i$ scattered by a target (atomic potential), and the corresponding asymptotic stationary wavefunctions are offset by a phase δ.

The concept of time delay is often being with a narrow wavepacket, which was an inspiration for Wigner to start with a time-dependent wave function composed of two frequencies [27]. He wrote down the wavepacket in an asymptotic region and considered the delay that emerges from the wavepacket due to interaction. At the large distance, the asymptotic behavior of the incoming wavepacket is given by

$$\Psi_{\mathrm{in}}(r,t) \simeq \frac{1}{\sqrt{r}} \int \mathrm{d}E\ |\phi(E)|\ \exp\{-\mathrm{i}kr - \mathrm{i}Et\} \quad r \to \infty, \tag{5.6}$$

where it peaks at $r = -v\,t$, with the group velocity $v \equiv \mathrm{d}E/\mathrm{d}k = k/\mu$. The asymptotic behavior of the outgoing wavepacket at a large distance from the center of scattering, which carries a phase $\delta(E)$, is provided by

$$\Psi_{\mathrm{out}}(r,t) \simeq \frac{1}{\sqrt{r}} \int \mathrm{d}E\ |\phi(E)|\ \mathrm{e}^{2\mathrm{i}\delta(E)}\mathrm{e}^{\mathrm{i}kr - \mathrm{i}Et} \quad r \to \infty, \tag{5.7}$$

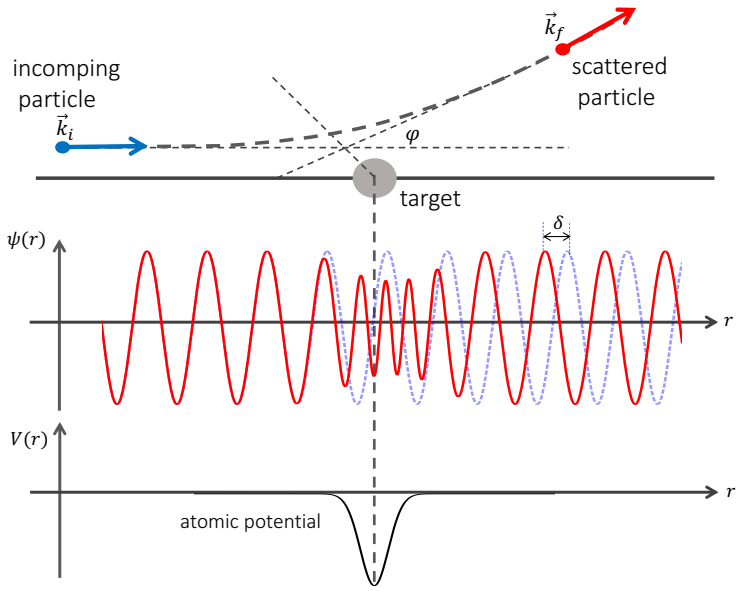

Figure 5.1: Upper part: The incoming particle with momentum $\vec{k}_i$ is deflected by the angle φ. The magnitude of the particle's momentum is unchanged, while the corresponding asymptotic stationary wavefunctions are offset by a phase δ in comparison with the free particle wave function (Middle part). The red solid line wave depicts the scattered wave, while the dashed blue line depicts the free wave without the change of the phase. Lower part: Atomic potential. The idea of this sketch is taken from [204].

where it has a peak at

$$r = v\,t - 2\,\mathrm{d}\delta(E)/\mathrm{d}k, \tag{5.8}$$

which the interaction has delayed the particle by a time

$$\tau = 2\,\frac{\mathrm{d}\delta(E)}{\mathrm{d}E}. \tag{5.9}$$

In 1948 Eisenbud in his Ph.D. dissertation [152] obtained the time delay in a single channel, which is given by the energy derivative of the phase shift as the same in Eq. (5.9). He derived the multichannel generalization by restricting to the case that only waves with angular momentum $m = 0$ (s-wave) participate in the reaction. The relation he found for the matrix time delay [205] is given by

$$\tau_{mm'}^{\text{Eisenbud}} = \frac{\mathrm{d}}{\mathrm{d}E}\,[S-1]_{mm'}\,, \tag{5.10}$$

where **S** describes the scattering matrix, short 'S-matrix' [206]. The scattering matrix **S** describes the transformation of a set of input excitations $|\psi_{\text{in}}\rangle$ on M channels into the set of

outputs $|\psi_{\text{out}}\rangle$ as $|\psi_{\text{out}}\rangle = \mathbf{S}\,|\psi_{\text{in}}\rangle$ [207], which is a unitary matrix, i.e., $\mathbf{S}\mathbf{S}^{\dagger} = \mathbf{I}$. As Eisenbud considered only s-wave scattering, he concluded that, in the case of single-channel scattering, his relation is equivalent to the time delay he defined earlier.

The problem of multichannel time delay was resolved by Smith [28] in 1959, where he defined the lifetime matrix $\mathbf{Q}$, which is Hermitian, and its diagonal element Q_{mm} describes the average lifetime of a collision beginning in the mth channel. In the case that $\mathbf{Q}$ is diagonalized, its proper values, q_{mm}, are the lifetimes of metastable states. The lifetime matrix as a function of energy has some properties [205]. As the first property, it has a relation with the scattering matrix as

$$\mathbf{Q} = \mathrm{i}\hbar\,\mathbf{S}\frac{\mathrm{d}\mathbf{S}^{\dagger}}{\mathrm{d}E} = -\mathrm{i}\hbar\,\frac{\mathrm{d}\mathbf{S}}{\mathrm{d}E}\mathbf{S}^{\dagger} = \mathbf{Q}^{\dagger}, \tag{5.11}$$

where this relation shows that $\mathbf{Q}$ is a Hermitian matrix. The second property shows that one can find $\mathbf{S}$ from $\mathbf{Q}$ as a function of energy that is given by

$$\mathbf{S} = \mathbf{I} - \frac{\mathrm{i}}{\hbar}\int_{E}^{\infty} \mathrm{d}E'\mathbf{Q}(E')\mathbf{S}(E'). \tag{5.12}$$

Smith's lifetime matrix, $\mathbf{Q}$, for a single channel reduced to the time delay relation that is obtained by Eisenbud and Wigner, which is called "Eisenbud-Wigner-Smith" time delay or just the Wigner time delay (both terms are used interchangeably) and is given by

$$\tau_m^{\text{EWS}} = 2\hbar\frac{\mathrm{d}\delta_m(E)}{\mathrm{d}E}. \tag{5.13}$$

5.2.2 Asymptotic behavior of $\langle r\rangle$

It has been proposed by Brenig, and Haag [156] that instead of specifying the scattered wave packet's position by its peak, one can evaluate the expectation value of $r = |\vec{r}|$ at large times outside the interaction range. Under this condition, the scattered wavepacket behaves like a free particle wavepacket. For this matter, let's consider a two-dimensional wavepacket [151] as

$$\Psi(\vec{r},t) = \frac{1}{2\pi}\int \Phi\left(\vec{k}\right)\,\exp\left\{\mathrm{i}\varphi\left(\vec{k}\right)\right\}\,\mathrm{d}^2k, \tag{5.14}$$

where the phase

$$\varphi\left(\vec{k}\right) = \vec{k}\cdot\vec{r} - \frac{\vec{k}^{\,2}}{2\mu}t. \tag{5.15}$$

Note that, Eq. (5.14) is normalized to unity. Therefore $|\Phi\left(\vec{k}\right)|^2$ is the momentum space probability density. The wave number is defined by

$$k \equiv \pm\frac{\sqrt{2\mu E}}{\hbar}. \quad \text{with} \begin{cases} k > 0 \Rightarrow \text{traveling to the right,} \\ k < 0 \Rightarrow \text{traveling to the left.} \end{cases} \tag{5.16}$$

The wavefunction in momentum space $\Phi\left(\vec{k}\right)$ is a relatively slowly varying function of k, where the phase $\varphi\left(\vec{k}\right)$ is generally large and rapidly varying. The rapid oscillations of $\exp\left\{\mathrm{i}\varphi\left(\vec{k}\right)\right\}$ over most of the range of integration means that the integrand averages to almost zero. Exceptions to this cancellation rule occur only at points where $\varphi\left(\vec{k}\right)$ has an extremum. The integral can therefore be estimated by finding all the points in the k-plane where $\varphi\left(\vec{k}\right)$ has a vanishing derivative,

$$\nabla_{\vec{k}}\left(\vec{k}\cdot\vec{r}-\frac{\vec{k}^{\,2}}{2\mu}t\right)=0 \quad \Rightarrow \quad \vec{k}_0=\frac{\mu\vec{r}}{t}, \tag{5.17}$$

evaluating (approximately) the integral in the neighborhood of each of these points, and summing the contributions. This procedure is known as the *method of stationary phase.*

The phase $\varphi\left(\vec{k}\right)$ has a vanishing first derivative at $\vec{k}=\vec{k_0}$. In the neighborhood of this point, $\varphi\left(\vec{k}\right)$ and $\Phi\left(\vec{k}\right)$ can be expanded as a Taylor series. Therefore, the wavepacket in Eq. (5.14) becomes

$$\Psi(\vec{r},t)\approx\exp\left\{\mathrm{i}\left(\frac{\mu\vec{r}^{\,2}}{2t}-\frac{\pi}{2}\right)\right\}\left[\left(\frac{\mu}{t}\right)\Phi\left(\vec{k}_0\right)-\frac{\mathrm{i}}{2}\left(\frac{\mu}{t}\right)^2\nabla^2_{\vec{k}_0}\,\Phi\left(\vec{k}_0\right)+\ldots\right]. \tag{5.18}$$

Appendix B contains the underlying details of this derivation. Using this asymptotic form, Eq. (5.18), we can evaluate the expectation value of $r=|\vec{r}|$ that is given by

$$\langle r\rangle=\langle v\rangle\,t+b+\mathcal{O}(t^{-1}), \quad t\to\infty \tag{5.19}$$

where

$$\langle v\rangle\,t=\frac{\langle k\rangle}{\mu}t=\left(\frac{t}{\mu}\right)\int|\vec{k}|\;\Phi^*\left(\vec{k}\right)\Phi\left(\vec{k}\right)\;\mathrm{d}^2k, \tag{5.20}$$

and

$$b=\frac{\mathrm{i}}{2}\int\left[\Phi^*\left(\vec{k}\right)\right]^2\frac{\partial}{\partial k}\left[\frac{\Phi\left(\vec{k}\right)}{\Phi^*\left(\vec{k}\right)}\right]\mathrm{d}^2k. \tag{5.21}$$

With $\Phi\left(\vec{k}\right)=|\Phi\left(\vec{k}\right)|\exp\left[\mathrm{i}\arg\left(\Phi\left(\vec{k}\right)\right)\right]=|\Phi\left(\vec{k}\right)|\mathrm{e}^{\mathrm{i}2\delta(E)}$, Eq. (5.21) becomes

$$b=-\left\langle\frac{\mathrm{d}}{\mathrm{d}k}\arg\left(\Phi\left(\vec{k}\right)\right)\right\rangle=-2\left\langle v\frac{\mathrm{d}}{\mathrm{d}E}\delta(E)\right\rangle \tag{5.22}$$

where $v=k/\mu$, and if the energy spectrum of the wave packet is sharply peaked, we can replace v by $\langle v\rangle$. Eventually Eq.(5.19) becomes asymptotically

$$\langle r\rangle=\langle v\rangle\,(t-\tau), \quad (t\to\infty) \tag{5.23}$$

where

$$\tau=2\left\langle\frac{\partial\delta(E)}{\partial E}\right\rangle, \tag{5.24}$$

is the s-wave result of Eisenbud-Wigner-Smith's time delay.

Figure 5.2 shows the time delay for a wavepacket, the offset in expectation value of wavepacket Eq. (5.23) away from interaction region and the time delay with considering the energy derivative of the phase shift, which is the limit for an infinite narrow-bandwidth wavepacket. The system is a model two-dimensional spherical potential $V(r) = -\exp\{-(r/r_0)^2\}$, where with $r_0 = 1.73$, it supports a ground state energy of $E_0 = -9.75\,\mathrm{eV}$.

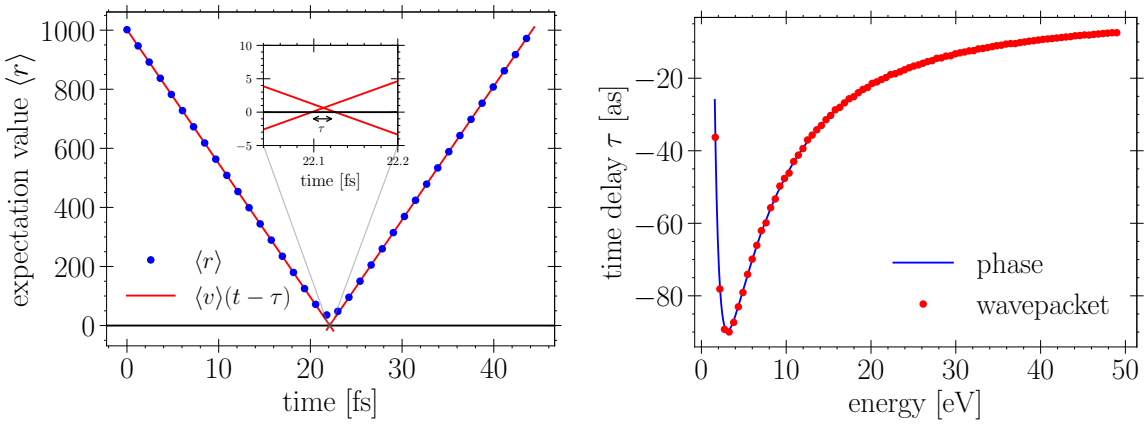

Figure 5.2: Eisenbud-Wigner-Smith time delay process for a 2d system for angular momentum of $m = 1$. The left panel shows the expectation value as a function of time, the blue dot indicates the expectation value during the scattering process, and red lines indicate the asymptotic behavior of $\langle r \rangle$ before and after scattering far from the center, wherewith propagating back from both side, an offset (see inset plot) is obtained which implies the time delay. The right panel represents a comparison of the time delay as a function of energy for the two approaches, the phase (blue line) and the asymptotic expectation value of the wavepacket (red dotted) far from the scattering center.

In the left panel of Fig. 5.2, the expectation value is depicted (blue bullet). We fit a linear function at a large distance far, before and after, the region of the interaction (red line). The slope of the fitted line gives the velocity of the particle, v. The distance between the fitted lines that meet the time axis, before and after the interaction, denotes to be the time delay, τ.

The right panel in Fig. 5.2 indicates the time delay using two methods as mentioned earlier which are the same. An increasing and then decreasing trend observes in the time delay as a function of energy. For higher kinetic energy, the particle hardly feels the potential, thus, the time delay tends to be zero. By decreasing the energy, the particle starts to feel the target, and the time delay increases. For very low energy, $E \approx 3\,\mathrm{eV}$, the particle is trapped

into the centrifugal barrier induced by angular momentum $m = 1$, consequently, the time delay shows a decreasing trend and the advance delay increases.

To sum up this section, we reviewed time delay in scattering systems briefly, but this chapter focuses primarily on photoionization time delay in two-dimensional models with anisotropic potentials, which we analyze analytically from two perspectives: scattering theory, which emphasizes the phase shift of continuum states (energy-domain), and wavepacket theory, which concentrates on the expectation value of wavepackets at a considerable large distance from the center (time-domain).

5.3 Photoionization time delay from a scattering theory perspective

In scattering theory, the phase of the transmitted wave is a direct consequence of the interaction of the incident wave with the scattering potential. For studying the scattering process in two-dimensional systems, we restrict our attention now to solving the time-independent Schrödinger equation, Eq. (2.4) with Hamiltonian in Eq. (2.3) for such systems by beginning with the following ansatz

$$\Phi_j(\vec{r}, E) = \frac{1}{\sqrt{2\pi}} \sum_{m=-M}^{M} \mathrm{e}^{\mathrm{i}m\phi} \frac{\psi_{mj}(r, E)}{\sqrt{r}}, \tag{5.25}$$

where the subscript j indicates the degeneracy of scattering states which are *independent*, *orthogonal* solutions of the Hamiltonian for each energy E [208]

$$\begin{aligned} (H - E)\, \Phi_j(\vec{r}, E) &= 0, \\ \langle \Phi_j(\vec{r}, E) | \Phi_{j'}(\vec{r}, E') \rangle &= \delta_{jj'}\, \delta(E - E'), \end{aligned} \tag{5.26}$$

where $\delta_{jj'}$ is the Kronecker delta, and $\delta(E - E')$ is the Dirac delta function. Here $\vec{r} = r\,(\cos\phi, \sin\phi)$ is the electron coordinate, and a complete orthogonormal set $\mathrm{e}^{\mathrm{i}m\phi}$ that $\left\langle \mathrm{e}^{\mathrm{i}m\phi} \middle| \mathrm{e}^{\mathrm{i}m'\phi} \right\rangle = 2\pi\, \delta_{mm'}$.

Inserting Eq. (5.25), into Schrödinger equation, we obtain

$$\left[\frac{\partial^2}{\partial r^2} - \frac{2\mu}{\hbar^2} \frac{m^2 - 1/4}{2r^2} + \frac{2\mu}{\hbar^2} E \right] \psi_{mj}(r, E) = \frac{2\mu}{\hbar^2} \sum_{m'} V_{mm'}(r) \psi_{m'j}(r, E), \tag{5.27}$$

where $V_{mm'}$ is potential matrix and given by

$$V_{mm'}(r) = \frac{1}{2\pi} \int_0^{2\pi} \mathrm{d}\phi\, \mathrm{e}^{-\mathrm{i}m\phi}\, V(\vec{r})\, \mathrm{e}^{\mathrm{i}m'\phi}, \tag{5.28}$$

which is not necessarily diagonal. The potential, $V(\vec{r})$, vanishes as $r \to \infty$. We compute $V_{mm'}(r)$ by performing the Gauss-Legendre quadrature integration. Because of the high oscillating nature of the integral Eq. (5.28), we use a high-order quadrature. In general, the potential matrix $V_{mm'}$ is a Hermitian matrix, and as $r \to \infty$ becomes diagonal.

As we have $2M+1$ solutions for angular momentum, we expect to find also $2M+1$ linearly-independent solutions, $j = -M, \cdots, M$. Thus we can address $\psi_{mj}(r)$ as representing a $([2M+1] \times [2M+1])$ matrix as a function of r. This is a square matrix, each column of which represents a separate independent solution.

The phases of Φ_j in Eq. (5.25) can be chosen such that Φ_j is real for almost all problems in atomic and molecular physics, for instance, we can choose a real angular basis set instead of that complex we have here chosen. Here the coupled-channel Eq. (5.27) is solved numerically using the Johnson renormalized Numerov method, see Appendix A.

This set of solutions, ψ_{mj}, have a well-defined behavior at a large distance far from the center. In the next subsection, we discuss two asymptotic behaviors of these solutions.

5.3.1 Asymptotic solutions and scattering matrix

In the limit as $r \to \infty$ equation (5.27) becomes uncoupled, and we must impose the following asymptotic boundary conditions on the radial functions

$$\left[\frac{\partial^2}{\partial r^2} - \frac{2\mu}{\hbar^2}\frac{m^2 - 1/4}{2r^2} + \frac{2\mu}{\hbar^2}E\right]\psi_{mj}(r,E)_{r\to\infty} \sim 0. \tag{5.29}$$

From Eq. (5.29), and using the fact that the potential matrix is symmetric we can write

$$\mathbf{\Psi}\mathbf{\Psi}''^{\dagger} - \mathbf{\Psi}''^{\dagger}\mathbf{\Psi} = \frac{\partial}{\partial r}\left(\mathbf{\Psi}^{\dagger}\mathbf{\Psi}' - \mathbf{\Psi}'^{\dagger}\mathbf{\Psi}\right) = 0, \tag{5.30}$$

where $\mathbf{\Psi}''$ is equivalent to $\left(\partial^2/\partial r^2\right)\mathbf{\Psi}(r)$. The boundary condition at the origin $\mathbf{\Psi}(0) = 0$ imposes the constraint

$$\mathbf{\Psi}^{\dagger}\mathbf{\Psi}' - \mathbf{\Psi}'^{\dagger}\mathbf{\Psi} = 0. \tag{5.31}$$

We have yet to impose well-behaved boundary conditions at $\mathbf{\Psi}(r \to \infty)$. The general solution of Eq. (5.29) can be expressed as a linear combination of two independent solutions as

$$\lim_{r\to\infty}\psi_{mj}(r,E) \sim J_m(kr)A_{mj} + Y_m(kr)B_{mj}, \tag{5.32}$$

where J_m and Y_m are the Riccati-Bessel functions of the first and second kinds, respectively, and asymptotically approach *standing* waves. Here $k = \sqrt{2\mu E}/\hbar$ is the wave number. It is worth mentioning that the Wronskian of J_m and Y_m is equal to unity, that is

$$W\{J_m, Y_m\} = Y_m\frac{\partial J_m}{\partial r} - J_m\frac{\partial Y_m}{\partial r} = 1. \tag{5.33}$$

The r-independent matrix coefficients $\mathbf{A}$ and $\mathbf{B}$ are determined by matching Eq. (5.32) with the numerical solutions of Eq. (5.27) where $V(\vec{r}) \approx 0$. Almost all the information regarding the scattering phase is embedded in these two matrices. These matrices are full matrices and in the case of spherical potentials are diagonal.

Applying the condition imposed by Eq. (5.31) to Eq. (5.32) and using Eq. (5.33) we find that the following constraint must be imposed on the matrices $\mathbf{A}$ and $\mathbf{B}$

$$\mathbf{A}^\dagger\mathbf{B} = \mathbf{B}^\dagger\mathbf{A}. \tag{5.34}$$

It is worth mentioning that for long-range potentials, one expects to use Coulomb functions F_m and G_m [209, 210, 211] instead of J_m and Y_m which are related to short-range potentials.

Equation (5.32) can be defined by introducing the alternate set of independent functions as follows

$$\lim_{r\to\infty} \psi_{mj}(r,E) \sim \frac{1}{2}\left[H_m^+(kr)(A-\mathrm{i}B)_{mj} + H_m^-(kr)(A+\mathrm{i}B)_{mj}\right], \tag{5.35}$$

where $H_m^\pm$ are the Riccati-Hankel functions which are specified by

$$\lim_{r\to\infty} H_m^\pm(kr) = J_m(kr) \pm \mathrm{i}Y_m(kr) \sim \mathrm{i}^{\mp m}\mathrm{e}^{\pm \mathrm{i}kr}, \tag{5.36}$$

where these functions approach *running* waves $\mathrm{e}^{\pm \mathrm{i}kr}$ rather than that standing waves $\sin(kr - \pi m/2)$ and $\cos(kr - \pi m/2)$ that are asymptotically associated with J_m and Y_m.

We can always take an arbitrary linear combination of these $2M+1$ solutions and generate a new solution. In other words, if the matrix $\mathbf{\Psi}$ is a set of solutions, then $\mathbf{\Psi} \times \mathbf{C}([2M+1]\times[2M+1])$ is also a set of solutions provided $\mathbf{C}$ has an inverse [208]. Knowing this fact, starting with standing waves solution Eq. (5.32), we have

$$\lim_{r\to\infty} \psi^K_{mm'}(r,E) = \sum_j \psi_{mj}(r,E)A^{-1}_{m'j} \sim J_m(kr)\delta_{mm'} + Y_m(kr)K_{mm'}, \tag{5.37}$$

where superscript 'K' indicates these solutions are in terms of the $\mathbf{K}$ matrix, where the matrix $\mathbf{K}$ is related to the reactance matrix, short "K-matrix", of scattering theory [212, 213] and is given by

$$\mathbf{K} = \mathbf{B}\mathbf{A}^{-1}. \tag{5.38}$$

The K-matrix is a Hermitian matrix, $\mathbf{K}^\dagger = \mathbf{K}$, which can be proved by using Eq. (5.34).

Equation (5.37) is a real representation of the radial functions. Another real representation is the eigenchannel version of the multichannel quantum-defect theory introduced by Fano in 1970 [214], which utilizes the eigenvalues $\tan(\boldsymbol{\delta})$ and eigenvectors $\mathbf{U}$ of the matrix $\mathbf{K}$,

$$\mathbf{K} = \mathbf{U}\tan(\boldsymbol{\delta})\mathbf{U}^\dagger. \tag{5.39}$$

The radial solutions in the Fano representation have the following form outside the reaction volume

$$\lim_{r\to\infty} \psi_{mj}(r,E) \sim U_{mj}\left[J_m(kr)\cos(\delta_m) + Y_m(kr)\sin(\delta_m)\right]. \tag{5.40}$$

Comparing to Eq. (5.32), we can write

$$\mathbf{A} = \mathbf{U}\cos(\boldsymbol{\delta}), \quad \mathbf{B} = \mathbf{U}\sin(\boldsymbol{\delta}). \tag{5.41}$$

The techniques for obtaining physical solutions that remain well-behaved at $r \to \infty$ and for calculating the observables, using the Fano representation, are discussed in numerous papers [215, 216, 217].

In the context that we are considering, the definition of open and closed channels are as follows: Channels with $E > 0$ will support unbound radial wavefunctions, continuous with respect to E, and are termed *open channels*. *Closed channels* are those with $E < \lim_{r\to\infty} V_m(r)$ with m the channel index, and will result in discrete bound wavefunctions. Therefore, the specific set of radial functions, $\psi^K_{mm'}$, in Eq. (5.35) are real and represent physical solutions if all scattering channels are open. In closed channels, the solutions $\psi^K_{mm'}$ are diverging. In the system under consideration, there are no closed channels, therefore, the set of solutions in Eq. (5.37) represents a physical solution.

For the case of running waves solution Eq. (5.35), a set of solutions by a linear combination as the following is given by

$$\lim_{r\to\infty} \psi^S_{mm'}(r,E) = \sum_j \psi_{mj}(r,E)\,(A - \mathrm{i}B)^{-1}_{m'j} \sim \frac{1}{2}\left[H^+_m(kr)\delta_{mm'} + H^-_m(kr)S_{mm'}\right], \tag{5.42}$$

where matrix $\mathbf{S}$ is related to the scattering matrix, short 'S-matrix', of scattering theory and is given by

$$\mathbf{S} = (\mathbf{A} + \mathrm{i}\mathbf{B})(\mathbf{A} - \mathrm{i}\mathbf{B})^{-1}, \tag{5.43}$$

and immediately, we can derive a relation between the K-matrix and the scattering matrix, which reads

$$\mathbf{S} = (\mathbf{I} + \mathrm{i}\mathbf{K})(\mathbf{I} - \mathrm{i}\mathbf{K})^{-1}. \tag{5.44}$$

Using the same technique as in Eq. (5.39), the S-matrix can be decomposed into a product of two matrices according to $\mathbf{S} = \mathbf{U}\mathrm{e}^{\mathrm{i}2\boldsymbol{\delta}}\mathbf{U}^\dagger$. The diagonal matrix, $\boldsymbol{\delta}$ is the phase shift of scattering theory, and is the same as in Eq. (5.39). Moreover, from Eq. (5.44) we can understand that the S-matrix is a unitary matrix

$$\mathbf{S}\mathbf{S}^\dagger = \mathbf{I}. \tag{5.45}$$

The S-matrix in the case of spherical potentials is a diagonal matrix and the diagonal element is $\mathrm{e}^{\mathrm{i}2\delta_m}$, where m is the angular momentum index.

5.3.2 Energy normalization

If $\Phi_j(\vec{r}, E)$ and $\Phi_{j'}(\vec{r}, E')$ are two specific solutions of the total Hamiltonian H, with total energy eigenvalues E and E' respectively, we must evaluate the overlap

$$N_{jj'}(E, E') = \langle \Phi_{j'}(\vec{r}, E') | \Phi_j(\vec{r}, E) \rangle \,, \tag{5.46}$$

to ensure that the solutions yield a proper orthonormal set that satisfies Eq. (5.26). Here $N_{jj'}(E, E')$ denotes the normalization matrix. The wavefunctions expansion in Eq. (5.25) already employ basis sets of angular momentum which are orthonormal. Therefore we must consider the normalization with respect to the total energy E and the degeneracies of the continuum states j. These properties are determined by the radial function $\psi_{mj}(r, E)$ in Eq. (5.25). Consequently, Eq. (5.46) in an integration form is given by

$$\lim_{r\to\infty} N_{jj'}(E, E') \sim \int_0^r \mathrm{d}r' \, \psi^*_{mj'}(r', E')\psi_{mj}(r', E). \tag{5.47}$$

The solutions $\Phi_{j'}(\vec{r}, E')$ and $\Phi_j(\vec{r}, E)$ from Eq. (5.25) must satisfy the condition [208]

$$\langle \Phi_{j'}(\vec{r}, E') | (H - E)\Phi_j(\vec{r}, E) \rangle = \langle (H - E')\Phi_{j'}(\vec{r}, E') | \Phi_j(\vec{r}, E) \rangle = 0. \tag{5.48}$$

Using the fact that the matrix potential is symmetric, Eq. (5.48) yields the following result as $r \to \infty$

$$\begin{aligned} \int_0^r \mathrm{d}r' \left[\psi^*_{mj'}(r', E') \frac{\partial^2}{\partial r'^2} \psi_{mj}(r', E) - \frac{\partial^2}{\partial r'^2} \psi^*_{mj'}(r', E') \, \psi_{mj}(r', E) \right] \\ = \int_0^r \mathrm{d}r' \, \frac{2\mu}{\hbar^2} (E - E') \psi^*_{mj'}(r', E')\psi_{mj}(r', E) \end{aligned} \tag{5.49}$$

Since we can write the bracketed term as a total differential, we can integrate the left-hand side of Eq. (5.49) using the boundary condition $\psi_{mj}(0, E) = \psi_{mj'}(0, E') = 0$ that becomes as follows

$$\begin{aligned} \int_0^r \mathrm{d}r' \, \psi^*_{mj'}(r', E')\psi_{mj}(r', E) = \frac{\hbar^2}{2\mu(E - E')} \Big[\psi^*_{mj'}(r, E') \frac{\partial}{\partial r} \psi_{mj}(r, E) \\ - \frac{\partial}{\partial r} \psi^*_{mj'}(r, E') \, \psi_{mj}(r, E) \Big]. \end{aligned} \tag{5.50}$$

This result allows us to determine the normalization matrix $\mathbf{N}$ entirely in terms of the *asymptotic* analytic properties of the radial functions

$$\lim_{r\to\infty} N_{jj'}(E, E') \sim \frac{\hbar^2}{2\mu(E - E')} \left[\psi^*_{mj'}(r, E') \frac{\partial}{\partial r} \psi_{mj}(r, E) - \frac{\partial}{\partial r} \psi^*_{mj'}(r, E') \, \psi_{mj}(r, E) \right], \tag{5.51}$$

The set of functions in Eq. (5.42) are complex and represent physical solutions. Therefore, introducing Eq. (5.42) into Eq. (5.51) leads to the result

$$N^S_{mm'}(E, E') = \left(\frac{\hbar^2 \pi}{2\mu} \right) \delta(E - E') \left[\delta_{mm'} + (SS^\dagger)_{mm'} \right], \tag{5.52}$$

Note that in Eq. (5.52), we have used the asymptotic behavior of Hankel functions which are defined in Eq. (5.36). The unitarity of **S** in Eq. (5.45) assures that the continuum states, expressed in terms of radial function with asymptotic properties prescribed by $\psi^S_{mm'}$ in Eq. (5.42), form an orthogonal set of solutions that is $N^S_{mm'}(E,E') = \left(\frac{\hbar^2\pi}{\mu}\right)\delta_{mm'}\,\delta(E-E')$. Consequently, if each radial function $\psi^S_{mm'}$ is multiplied by $\sqrt{\mu/\hbar^2\pi}$, we obtain the complete energy-normalized set of continuum states implied in Eq. (5.25)

$$\boxed{\Phi^S_m(\vec{r},E) = \sqrt{\frac{\mu}{2\hbar^2\pi^2}}\sum_{m'} \mathrm{e}^{\mathrm{i}m'\phi}\,\frac{\psi^S_{m'm}(r,E)}{\sqrt{r}}.} \tag{5.53}$$

For many purposes, it is preferable to form an orthonormal set of continuum states with *real* radial function. In Eq. (5.37) we presented a particular set of solutions $\psi^K_{mm'}$ which have the virtue of yielding real radial functions which are expressed in terms of the standing waves rather than the complex running waves. In the special case that all channels are open, these sets of solutions represent a physical solution, therefore the normalization matrix for these functions may also be evaluated, that is

$$N^K_{mm'}(E,E') = \left(\frac{\hbar^2\pi}{\mu}\right)\delta(E-E')\left[\delta_{mm'} + (KK^\dagger)_{mm'}\right]. \tag{5.54}$$

Using the results of Eq. (5.54), a real orthonormal set of energy-normalized radial functions can be defined.

In this section, we examined two asymptotic solutions and determined a way to make continuum states energy-normalized; now in order to study the photoionization process, we must generate the total molecular wave function.

5.3.3 Boundary condition and final molecular wavefunction

Two wavefunctions involve in the scattering scenario: incoming and outgoing. The photoionization time delay corresponds to a half-scattering process in which a matter wavepacket exists in the continuum only in the exit channel. In contrast, in the entrance channel, the wave function represents a bound rather than a continuum state [218]. Therefore, we consider only the outgoing wavefunction.

The molecular wavefunction can be formed as

$$\Psi_f(\vec{r},\vec{k}) = \sum_m a_m(\varphi)\Phi^S_m(\vec{r},E), \tag{5.55}$$

where $\vec{k} = k(\cos\varphi, \sin\varphi)$ is the wave vector in which φ denotes the emission direction of the photoelectron with the asymptotic momentum k. The subscript 'f' signifies the final wave

function. The coefficient a_m is to be determined, and Φ_m^S is defined in Eq. (5.53), which are energy-normalized.

The wavefunction calculated in Eq. (5.55) contains both incoming and outgoing wavefunctions. To separate them and choose the outgoing part, we have to calculate the coefficient a_m in such a way as to only keep the outgoing part. For this matter, we employ the well-defined boundary condition of the asymptotic behavior of the outgoing wavefunction as $r \to \infty$ in terms of plane waves

$$\Psi_f^{(-)}(\vec{r},\vec{k})_{r\to\infty} \sim \mathrm{e}^{\mathrm{i}kr\cos(\phi-\varphi)} + f^{(-)}(\vec{k},\phi)\frac{\mathrm{e}^{-\mathrm{i}kr}}{\sqrt{r}}, \tag{5.56}$$

where the second term signifies the spherical wave along with its scattering amplitude of $f^{(-)}$. The first term in Eq. (5.56) indicates the incident plane wave, which has a partial wave expansion [219]

$$\mathrm{e}^{\mathrm{i}kr\cos(\phi-\varphi)} = \sqrt{\frac{1}{2\pi}}\frac{1}{\sqrt{kr}}\sum_m \mathrm{i}^m \mathrm{e}^{\mathrm{i}m(\phi-\varphi)}\left[H_m^-(kr) + H_m^+(kr)\right], \tag{5.57}$$

where $H_m^\pm$ are defined in Eq. (5.36).

It is worth mentioning that the choosing sign '$(-)$' for outgoing or $(+)$' for incoming wavefunction is related to the sign of $\mathrm{e}^{\mp\mathrm{i}kr}$ which is appeared in the asymptotic behavior in Eq. (5.56).

To obtain coefficient $a_m^{(-)}$, from the left side of Eq. (5.56), we insert Eq. (5.53) in which we use the asymptotic solution of Eq. (5.42), and from the right side substitute Eq. (5.57), then we derive

$$\begin{aligned}\sum_m a_m(\varphi)\sqrt{\frac{\mu}{\hbar^2 4\pi}}\sum_{m'}\mathrm{e}^{\mathrm{i}m'\phi}\frac{1}{\sqrt{r}}\left[H_{m'}^+(kr) + H_{m'}^-(kr)S_{m'm}\right] \\ = \sqrt{\frac{1}{2\pi}}\sum_{m'}\mathrm{i}^{m'}\mathrm{e}^{\mathrm{i}m'(\phi-\varphi)}\frac{1}{\sqrt{kr}}\left[H_{m'}^-(kr) + H_{m'}^+(kr)\right] + f^{(-)}(\vec{k},\phi)\frac{\mathrm{e}^{-\mathrm{i}kr}}{\sqrt{r}}.\end{aligned} \tag{5.58}$$

Using the asymptotic behavior of Hankel functions, i.e., Eq. (5.36), and substituting in Eq. (5.58), we have

$$\begin{aligned}&\frac{\mathrm{e}^{ikr}}{\sqrt{r}}\left(\sqrt{\frac{1}{2\pi}}\sum_{m,m'}\left[\sqrt{\frac{\mu}{2\hbar^2}}\,a_m(\varphi)\mathrm{i}^{-m'}\mathrm{e}^{\mathrm{i}m'\phi} - \sqrt{\frac{1}{k}}\mathrm{e}^{\mathrm{i}m'(\phi-\varphi)}\delta_{m'm}\right]\right) \\ &\quad = \frac{\mathrm{e}^{-ikr}}{\sqrt{r}}\left(f^{(-)}(\vec{k},\phi) + \sqrt{\frac{1}{2\pi}}\sum_{m,m'}\left[\sqrt{\frac{1}{k}}\mathrm{i}^{2m'}\mathrm{e}^{\mathrm{i}m'(\phi-\varphi)}\delta_{m'm} - \sqrt{\frac{\mu}{2\hbar^2}}a_m(\varphi)\mathrm{i}^{m'}\mathrm{e}^{\mathrm{i}m'\phi}S_{m'm}\right]\right).\end{aligned} \tag{5.59}$$

Since $e^{\pm ikr}$ are linearly independent, and the two $(\cdots)$ expressions in this equation are independent of r, they must each be identically zero. Therefore, from the left side, we drive

$$a_m(\varphi) = \sqrt{\frac{2\hbar^2}{\mu}}\ \frac{i^m}{\sqrt{k}} e^{-im\varphi}, \tag{5.60}$$

and from the right side, the scattering amplitude determines as

$$f^{(-)}(\vec{k},\phi) = \sqrt{\frac{1}{2\pi k}} \sum_m \sum_{m'} \left[i^{m+m'} e^{i(m\phi - m'\varphi)} S_{mm'} - i^{2m} e^{im(\phi-\varphi)} \delta_{mm'} \right]. \tag{5.61}$$

Substituting Eq. (5.60) into Eq. (5.55), the final outgoing wavefunction can be written as

$$\boxed{\Psi_f^{(-)}\left(\vec{r},\vec{k}\right) = \sqrt{\frac{2\hbar^2}{\mu}} \sum_m \frac{i^m}{\sqrt{k}}\, e^{-im\varphi}\, \Phi_m^S(\vec{r},E),} \tag{5.62}$$

where Φ_m^S is defined in Eq. (5.53).

Using the same technique we can derive the incoming wavefunction, which we do not need here.

Having the final wavefunction and initial state, the dipole matrix element between the bound state and the final state can then be calculated.

5.3.4 Matrix element and photoionization time delay

A complete description of photoionization requires information on the amplitude of the dipole transition matrix elements through the measurement of cross-sections.

The dipole matrix element between the final state and the bound state is thus given by

$$\mathcal{D}^{(-)}(E,\varphi) = \left\langle \Psi_f^{(-)}(\vec{r},\vec{k}) \middle| \vec{r}\cdot\vec{F} \middle| \Psi_i(\vec{r}) \right\rangle = \sqrt{\frac{2}{\pi}} \sum_m \frac{i^{-m}}{\sqrt{k}}\ d_m^{(-)}(E)\ e^{im\varphi}, \tag{5.63}$$

where $\vec{F}$ is the electric field, Eq. (2.11), Ψ_i is the initial state, which here is the ground state and can be calculated by using renormalized Numerov method, see Appendix A. the partial dipole transition matrix element $d_m^{(-)}$ is given by

$$d_m^{(-)}(E) = \sum_j \left((A - iB)^{-1} \right)^\dagger_{mj} d_j(E). \tag{5.64}$$

where $d_j(E)$ is determined by

$$d_j(E) = \left\langle \Phi_j(\vec{r},E) \middle| \vec{r}\cdot\vec{F} \middle| \Psi_i(\vec{r}) \right\rangle. \tag{5.65}$$

Here Φ_j is defined in Eq. (5.25). As we discussed in Eq. (5.25), we can choose the angular basis sets in such a way that Φ_j will be real. Therefore, $d_j(E)$ in Eq. (5.65) is a real vector.

Using Eq. (5.41) we can write

$$(\mathbf{A} - \mathrm{i}\,\mathbf{B})^{-1} = \Big[\mathbf{U}\cos(\boldsymbol{\delta}) - \mathrm{i}\,\mathbf{U}\sin(\boldsymbol{\delta})\Big]^{-1} = \mathrm{e}^{\mathrm{i}\boldsymbol{\delta}}\,\mathbf{U}^{-1}. \tag{5.66}$$

Introducing Eq. (5.66) to Eq. (5.64), we provide a relation between the partial dipole matrix-element and the scattering phase as

$$d_m^{(-)}(E) = \sum_j \mathrm{e}^{-\mathrm{i}\delta_j}\, U_{mj}\, d_j(E), \tag{5.67}$$

where δ_j is the scattering phase related to the eigenvalue and U_{mj} is the eigenvector unitary matrix of the S-matrix.

By having the dipole matrix element, we can simply define the photoionization cross-section as

$$\sigma\left(E,\varphi\right) = \frac{4\pi^2\omega}{3c}\left|\mathcal{D}^{(-)}\left(E,\varphi\right)\right|^2. \tag{5.68}$$

where ω is the photon frequency, and c is the speed of light.

Since we are investigating a system in weak field interaction, we can safely use first-order time-dependent perturbation theory, Eq. (4.17), in order to describe single-photon ionization photoelectron wavepacket as the outgoing wavepacket. As we discussed in Section 5.2.1, the wavefunction in the momentum representation, $\Phi(E)$, in the wavepacket after scattering, see Eq. (5.7) has a phase. In the case of a photoelectron wavepacket, the wavefunction in the momentum representation is the 1st-order perturbation theory, which contains the dipole matrix element. Consequently, in the case of the photoelectron wavepacket, we investigate the phase of the matrix element. Therefore, the single-photon ionization time delay may be defined as an energy derivative of the phase of the matrix element

$$\tau(E,\varphi) = \frac{\mathrm{d}}{\mathrm{d}E}\arg\left[\mathcal{D}^{(-)}\left(E,\varphi\right)\right], \tag{5.69}$$

where photoionization time delay depends on energy and emission angle as well as the field direction, which makes it a rich phenomenon. To avoid the problem of possible jumps of the calculated phase of the matrix element $\mathcal{D}^{(-)}$, entering the time delay definition Eq. (5.69), it is convenient to calculate the phase derivative as the imaginary part of the logarithmic derivative of the matrix element itself, i.e.,

$$\tau(E,\varphi) = \mathrm{Im}\left\{\frac{1}{\mathcal{D}^{(-)}}\frac{\mathrm{d}\mathcal{D}^{(-)}}{\mathrm{d}E}\right\}, \tag{5.70}$$

where Im implies the imaginary part.

In the case of spherical potentials, we can calculate the photoionization time delay and compare it with the Wigner time delay obtain from a full scattering process, see Section 5.2.1.

Since in spherical potentials, the scattering matrix is diagonal; thus, its eigenvector matrix U_{mj} is an identity matrix, we can write the partial matrix element, Eq. (5.67) as

$$d_m^{(-)}(E) = \mathrm{e}^{-\mathrm{i}\delta_m}\, d_m(E). \tag{5.71}$$

Inserting this into Eq. (5.70), we obtain

$$\tau_m(E,\varphi) = \mathrm{Im}\left\{\frac{1}{d_m^{(-)}}\frac{\mathrm{d}d_m^{(-)}}{\mathrm{d}E}\right\} = \frac{\mathrm{d}\delta_m(E)}{\mathrm{d}E}, \tag{5.72}$$

where it is independent of the emission angle, as expected, and δ_m is the partial phase of the partial matrix element. Comparing it with the Eisenbud-Wigner-Smith time delay, which is $\tau_m^{\mathrm{EWS}} = 2\frac{\mathrm{d}\delta_m(E)}{\mathrm{d}E}$, we figure out that in the case of spherical potentials, the photoionization time delay is independent of the initial state and is equal to the Wigner time delay. The factor 2 has not appeared in Eq. (5.72), as the photoionization time delay is a half-scattering process. Figure 5.2 provides an example of Wigner time delay in a spherical potential, the photoionization time delay is the same as in Fig. 5.2 with the difference that the quantity in the right panel, should be divided by factor 2.

It is clear in spherical potentials that scattering time delay (Wigner-Smith) and photoionization time delay are similar since channels have well-defined time delays and there are selection rules. However, this does not apply any longer to anisotropic potentials, and these two time delays are different.

Having an explicit relation for photoionization time delay, we can consider more complicated systems, for instance, a two-center system.

5.3.5 Two-center system

Two-center system is one of the most basic molecular structures for understanding some properties of matter, such as the wave character of matter using two-center interference, as first done in 1801 by Thomas Young with light waves [220] and in 1961 by Claus Jönsson with electrons [221]. With the introduction of attosecond pulses, we can now reveal more properties of matter in their interactions with lasers, namely, two-center interference in the photoionization delays of Kr_2 [222]. Here we consider the angle and energy-resolved time delay in a two-dimensional model two-center system.

A model potential for a two-center system is defined by

$$V(\vec{r}) = -\mathrm{e}^{-\left([x-R/2]^2-y^2\right)/r_0^2} - \mathrm{e}^{-\left([x+R/2]^2-y^2\right)/r_0^2}, \tag{5.73}$$

where R is the intra-atomic distance. We use with $R = 2$, and $r_0 = 1.732$. Here with these values, the potential supports a ground state with an energy of $E_0 = -20.35$ eV. Moreover,

we use a linear polarized pulse, and the direction of the field polarization is parallel to the molecular axis, i.e., $\vec{r} \cdot \vec{F} = \mp r \cos\phi$. The angle ϕ is the angle between the field direction and x-axis which is the molecular axis.

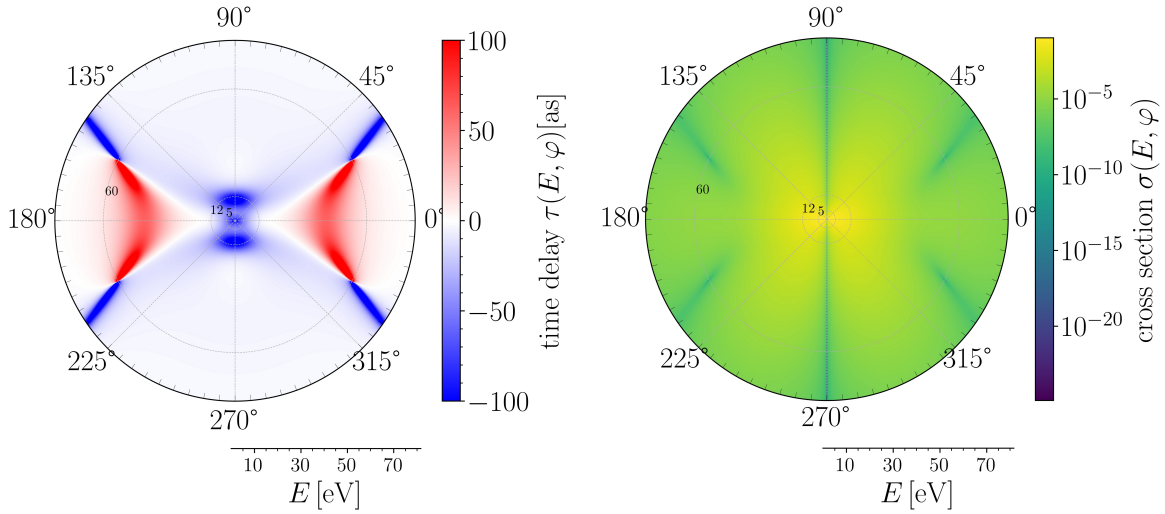

Figure 5.3: Left panel: polar surface photoionization time delay as a function of energy and emission angle. The structure at $E \approx 60$ shows a large positive and negative time delay at certain emission angles. Right panel: polar surface photoionization cross-section as a function of energy and emission angle in logarithmic scale. There are minimums at $E \approx 60$, and at $\varphi \approx \pi/2$, the cross-section is zero, since the field direction is parallel to the molecular axis; thus, the dipole element is zero.

Figure 5.3 shows energy and angular dependence of time delay and cross-section. These results present a complete, but complicated, picture of the molecular photoionization event, and the associated time delay for the outgoing photoelectron wavepacket. It is immediately apparent that there is a significant amount of structure observed, both as a function of energy and angle, with τ values ranging from -100 to $+100$ as. Because of the symmetry of the potential and selection rules, just odd partial dipoles are considerable, and among them, $m = \pm 1$ and ± 3 are dominant, see Fig. 5.5. Physically, the peaks in the cross-section correspond to maxima in the dipole integrals, which define the coupling between initial orbital and final continuum wavefunctions induced by ionizing radiation, with an angular dependence given by the partial-wave interferences. For a two-center system, this peak is the well-known shape-resonance [146, 147]. It corresponds to an enhancement of one of the partial waves, here, in this case, $m = \pm 1$, which can be considered as trapping of this part of the outgoing

wavepacket due to the form of the molecular potential energy surface. Figure 5.4 shows the effective potential, which is given by

$$V_m(r) = \bar{V}(r) + \frac{m^2 - 1/4}{2r^2}, \tag{5.74}$$

where $\bar{V}(r)$ the angular average of $V(\vec{r})$. Among different angular momentum, only $m = 1$

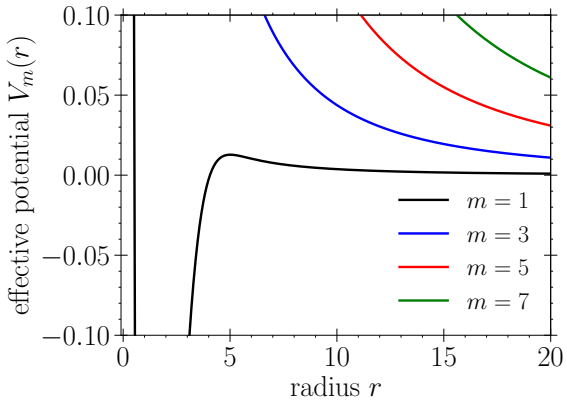

Figure 5.4: potential matrix component for $m = 1$ as a function of radius, we can see a barrier and this case, a large positive time delay

induces a barrier. It is, therefore, not unexpected that the time delay is also large in this region, as it appears as a ring between the energy range of $5 - 12\,\text{eV}$ with a positive time delay, $\tau > 0$, in Fig. 5.3a. However, this effect is not significant, since the barrier here is not too high. For large energy, the particle barely sees the potential, and as a consequence small time delay, and it tends to zero.

For very low energy, the particle can only see the lowest angular momentum, then the behavior of the system is as the spherical case and a large negative time delay in this region is predicted. The reason is that for very low energies, only the lowest angular momentum participates, one can see it from Fig. 5.4. Large negative and positive time delays that are observed in Fig. 5.3, also consider as singularities, at $E_c = 60\,\text{eV}$ are related to being zero in the cross-section. That means the coupling between the initial state and the final continuum state in this energy and emission angle is almost zero. The position of these points depends on the intra-atomic distance (R), in particular, one finds that as increases R they move to lower energies.

As can be seen in Fig. 5.5, at the given energy, the partial dipole matrix for $m = \pm 1$ turns into zero. The situation of a partial amplitude turning into zero at a particular energy value is commonly referred to as Cooper's minimum, in honor of J. W. Cooper, who theoretically

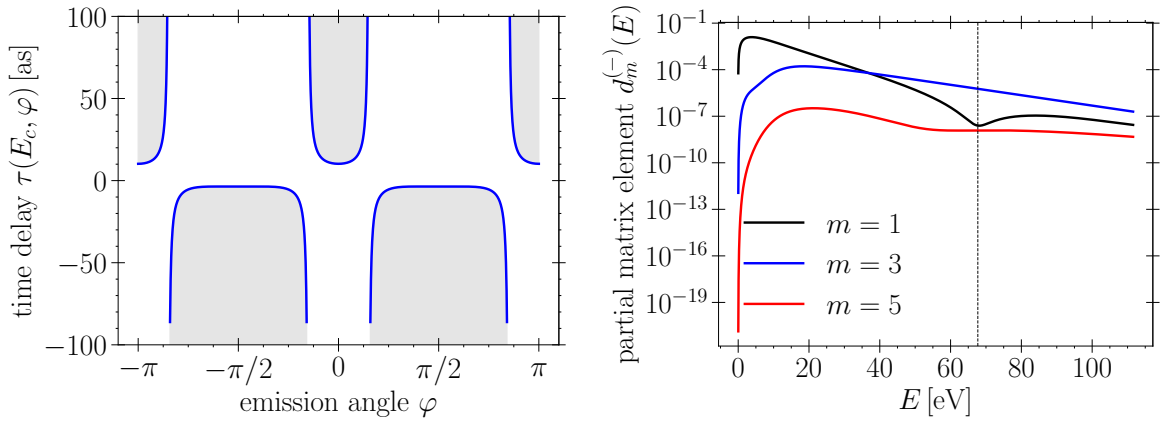

Figure 5.5: Left panel: time delay as a function of the emission angle for the given energy $E_c \approx 67\,\text{eV}$ that implies singularities. Right panel: the partial matrix element as a function of energy in logarithmic scale for $m = 1, 3$, and 5, as can be seen in $m = 1$, the matrix element turns into zero, which is related to Cooper's minimum. Other partial matrix elements are negligible.

predicted this phenomenon for the photoionization of noble gases [223]. Such a situation takes place in the molecular case. We use the two dominant angular momenta to demonstrate singularities, $m = \pm 1$ and ± 3. We write the dipole matrix element, Eq. (5.63), for the dominant angular momentum as

$$\mathcal{D}(E, \varphi) = \mathrm{i}\sqrt{\frac{8}{\pi}} \left(|d_3^{(-)}|^2 \mathrm{e}^{\mathrm{i}\zeta_3} \cos(3\varphi) - |d_1^{(-)}|^2 \mathrm{e}^{\mathrm{i}\zeta_1} \cos(\varphi) \right), \tag{5.75}$$

where ζ_3 and ζ_1 are the corresponding phases of the partial matrix element $d_3^{(-)}$ and $d_3^{(-)}$ respectively. Here we inserted the prefactor $1/\sqrt{k}$ in Eq. (5.63) into $d_m^{(-)}$ for the sake of simplicity. Now we consider Eq. (5.75) for singularities which take place in the vicinity of Cooper's minimum energy $E \approx E_c \approx 67\,\text{eV}$ and then calculate the time delay using Eq. 5.70 as

$$\tau(E_c, \varphi) = \frac{\mathrm{d}\zeta_3}{\mathrm{d}E}|_{E=E_c} - \frac{\left(|d_1^{(-)}(E_c)|^2\right)'}{|d_3^{(-)}(E_c)|^2} \frac{\cos(\varphi)}{\cos(3\varphi)} \sin(\zeta_1 - \zeta_3), \tag{5.76}$$

where $\left(|d_1^{(-)}(E_c)|^2\right)' = \frac{\mathrm{d}}{\mathrm{d}E}|d_1^{(-)}|^2_{E=E_c}$. From Eq. (5.76), it is evident that time delay variation with the ejection angle at the energy E_c has no relation to the phase derivatives of the partial waves but depends on the difference $\zeta_1 - \zeta_3$ of phases themselves. As for the singularities, they arise at the ejection angles φ, for which the function $\cos(3\varphi)$ possesses nodes that do not coincide with the node $\varphi = 90°$ of the function $\cos(\varphi)$. Therefore the position of the

singularities is at $\varphi = \cdots, -\pi/6, \pi/6, 5\pi/6, \cdots$ with a slight shifting in time delay due to the first term in Eq. (5.76).

Last but not least, large negative values of τ, which are observed as the singularities, i.e. $\tau \to -\infty$, contradict the causality principle [27], since, formally, they mean that the electron is ejected by the molecule long before the absorption of the photon. In Ref. [202], by analytical consideration of the emitted electron wavepacket evolution, they demonstrated that large negative values of the phase derivative with respect to energy do not violate the causality principle in which the maximum time delay does not exceed the ionizing laser pulse duration T. Thus, there is no contradiction with the causality principle.

In the conclusion of this section, we studied photoionization time delay using the phase of the scattering state in which we formulated the final wavefunction using the outgoing boundary condition and calculated the dipole matrix element between the ground bound state and the final state. Having the matrix element, we derived the photoionization time delay, which is the energy derivative of the phase of the matrix element.

Time delay can also be studied from the perspective of a wavepacket, which gives us a deeper understanding of its mechanics, this is a query that we wish to address in the next section.

5.4 Photoionization time delay from a wavepacket perspective

The scattering phase shift and associated time delay result in a group delay of the outgoing photoelectron wavepacket, born at a time t_0 within the ionizing laser pulse in a time-domain picture of photoionization [25]. In this case, the advanced wavepacket appears sooner than it would for the $V = 0$ case, while the retarded wavepacket appears later than it would for $V = 0$, where V is the scattering potential.

To demonstrate a wavepacket perspective of time delay, initially, we start with a full scattering process for an anisotropic potential and derive channel delays, then go further and investigate the photoionization time delay.

5.4.1 Partial time delay

Partial time delay is defined as the energy derivatives of the phase of the eigenvalues of the scattering matrix [224, 225, 226]. Using a standard linear-algebra diagonalization technique, the scattering matrix, as discussed in Section 5.3.1, decomposed into a product of two matrices

according to

$$\mathbf{S} = \mathbf{U}\mathrm{e}^{\mathrm{i}2\boldsymbol{\delta}}\mathbf{U}^{\dagger}, \tag{5.77}$$

where the columns of $\mathbf{U}$ are orthogonal and comprise the eigenvectors of $\mathbf{S}$, and the nonzero elements of the diagonal matrix $\mathrm{e}^{\mathrm{i}2\boldsymbol{\delta}}$ are its corresponding eigenvalues. Thus, the partial time delay is defined by

$$\tau_\nu(E) = \frac{\mathrm{d}\delta_\nu(E)}{\mathrm{d}E}. \tag{5.78}$$

In a full scattering process, an incoming free particle wavepacket is scattered by the scattering potential. After scattering at a large distance from the interaction region, we consider the outgoing wavepacket, which should be the same as the incoming wavepacket with slight shifting, and then we can measure the Wigner-Smith time delay. In order to achieve this, we create an initial wavepacket based on the eigenfunction of the scattering matrix for each channel. This guarantees that the outgoing wavepacket is the same as the incoming wavepacket in angular distribution, accordingly, the partial time delay can be measured. To illustrate this, an initial Gaussian wavepacket, which describes the free particle wavepacket, is formed as

$$\Psi_\nu(\vec{r}, k_0; t) = \left(\frac{2}{\pi}\right)^{\frac{1}{4}} \sqrt{\frac{1}{2\alpha(t)}} \sum_{m'} U_{m'\nu}(k_0)\, \mathrm{e}^{\mathrm{i}m'\phi} \exp\left\{-\frac{(r-r_0)^2}{4\alpha^2(t)} + \mathrm{i}k_0 r\right\}, \tag{5.79}$$

where the width of a Gaussian wavepacket evolves as

$$\frac{\mathrm{d}}{\mathrm{d}t}\alpha(t) = -2\mathrm{i}\alpha^2(t) \quad \rightarrow \quad \alpha(t) = \frac{1}{2\mathrm{i}t + c}, \tag{5.80}$$

thus, assuming $t = 0$ being the time of minimal width $\alpha_{\min}$(being real and positive)

$$\alpha(t) = \frac{1}{2\mathrm{i}t + 1/\alpha_{\min}} = \frac{\alpha_{\min}}{1 + 2\mathrm{i}\alpha_{\min}t} \quad \text{with} \quad |a(t)| = \frac{\alpha_{\min}}{\sqrt{1 + (2\alpha_{\min}t)^2}}, \tag{5.81}$$

where here we fix the minimal width with $\alpha_{\min} = 60$. In Eq. (5.79) $U_{m'\nu}$ is the S-matrix's eigenvector. The channel is represented by the index ν, which is the index of the S-matrix's eigenvalues.

Time-dependent wavepacket can be derived using the scattering state basis Φ_j^S, i.e., Eq. (5.53), as

$$\boxed{\Psi_\nu(\vec{r}, k_0; t) = \sum_j \int \mathrm{d}E\, b_{\nu j}(E, k_0, t)\, \Phi_j^S(\vec{r}, E)\, \mathrm{e}^{\mathrm{i}Et},} \tag{5.82}$$

where $b_{\nu j}$ is the coefficient to be determined. At $t = 0$, we assume the wavepacket is far from the center of interaction and described by Eq. (5.79). Therefore, we can calculate the

coefficient $b_{\nu j}$ in such a way that Eq. (5.82) at $t = 0$ be as Eq. (5.79). By multiplying $\left\langle \Phi^S_{j'}(\vec{r}, E') \right|$ from the left of Eq. (5.82), then

$$\left\langle \Phi^S_{j'}(\vec{r}, E', t) \middle| \Psi_\nu(\vec{r}, k_0; t) \right\rangle = \sum_j \int \mathrm{d}E \; b_{\nu j}(E, k_0) \left\langle \Phi^S_{j'}(\vec{r}, E') \middle| \Phi^S_j(\vec{r}, E) \right\rangle . \tag{5.83}$$

In Eq. (5.52), we created the asymptotic solutions such that the final wavefunctions are energy-normalized, thus, $\left\langle \Phi^S_{j'}(\vec{r}, E') \middle| \Phi^S_j(\vec{r}, E) \right\rangle = \delta(E - E')\delta_{jj'}$. Applying this in Eq. (5.83), $b_{\nu j}$ becomes

$$b_{\nu j}(E, k_0, t) = \left\langle \Phi^S_j(\vec{r}, E) \middle| \Psi_\nu(\vec{r}, k_0; t) \right\rangle , \tag{5.84}$$

where $\Psi_\nu(\vec{r}, k_0; t)$ is defined in Eq. (5.79).

Having the time-dependent wavepacket helps to analyze the system each time. To investigate the time delay, we consider the incoming and outgoing wavepacket before and after the interaction, far from the center, where it behaves like a free wavepacket. We then calculate the expectation value, as we discussed in subsection 5.2.2, which is given by

$$\langle r \rangle = \frac{\int \mathrm{d}^2 r \, r |\Psi_\nu(\vec{r}, k_0; t)|^2}{\int \mathrm{d}^2 r \, |\Psi_\nu(\vec{r}, k_0; t)|^2} . \tag{5.85}$$

Once we have the expectation value and also the velocity $\langle v \rangle$, which can be determined using the slope of $\langle r \rangle$, we can calculate time delay using Eq. (5.23), which is the difference between the delay before and after interaction with the scattering potential as was considered in Fig. 5.2.

We begin by generating an incoming wavepacket in such a way that it is not an eigenchannel of the scattering matrix, for example, in Eq. (5.79), the eigenvector $U_{m'\nu}$ has been chosen that is not the eigenvector of the S-matrix, see the left panel in Fig. 5.6. The system here is the two-center model potential in two dimensions, defined in Eq. (5.73). The incoming wavepacket is then scattered by the scattering potential, and after the interaction region far from the canter, we record the outgoing wavepacket, see the right panel in Fig. 5.6. The outgoing wavepacket has a different spatial distribution, and this difference in spatial distribution will not allow us to calculate the partial time delay correctly. Consequently, the time delay cannot be determined in this case.

However, in another situation where we generate an incoming wavepacket that is an eigenchannel of the S-matrix, in Eq. (5.82) the $U_{m'\nu}$ is the eigenvector of the S-matrix, see the left panel in Fig. 5.7. After scattering away from the interaction region we have an outgoing wavepacket. This outgoing wavepacket has the same spatial distribution as the incoming wavepacket, see the right panel in Fig. 5.7. Having the same spatial distribution in both incoming and outgoing wavepackets, we can calculate the partial time delay correctly.

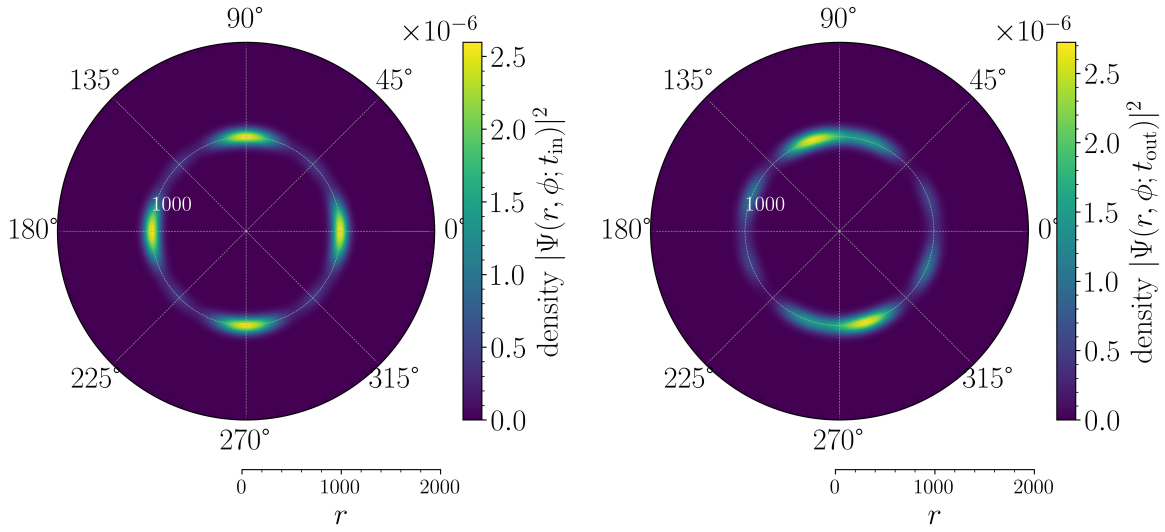

Figure 5.6: Polar surface of a two-dimensional wavepacket, Eq. (5.82), for initial momentum $k_0 = 0.9$ a.u. for the case the incoming wavepacket is not the eigenchannel of the S-matrix. Left panel: a snapshot of the incoming wave packet far away from the scattering center. Right panel: a snapshot of the outgoing wavepacket at a large distance from the center. Here $t_{\rm in}$, and $t_{\rm out}$ indicate the incoming wavepacket at the initial time and the outgoing wavepacket at the final time respectively.

The fringes in the wavepackets in Fig. 5.7 that is observed are due to the interference between the two atomic center; thus, the number of these fringes depends on the intra-atomic distance R. The larger R, the more fringes in the wavepacket will be observed.

Establishing a wavepacket in terms of eigenchannels of the S-matrix in which the incoming and outgoing wavepacket have the same spatial distribution, we can measure the partial time delay appropriately. Figure 5.8 displays the partial time delay using two approaches i.e., Eq. (5.78) where the energy derivative of eigenvalues of the scattering matrix and the offset in the expectation value of wavepackets away from the interaction region Eq. (5.85). In this figure, as an example, we considered the eigenvalue of the S-matrix and the wavepacket perspective for the channel $\nu = 0$, although, we can apply this approach for all channels. As can be seen, both approaches agree with each other. This approach can provide an intuitive picture of partial time delay, which is very helpful and understandable. The same procedure can be applied to the photoionization time delay in which we deal with the photoelectron wavepacket, which we investigate in detail in the next subsection.

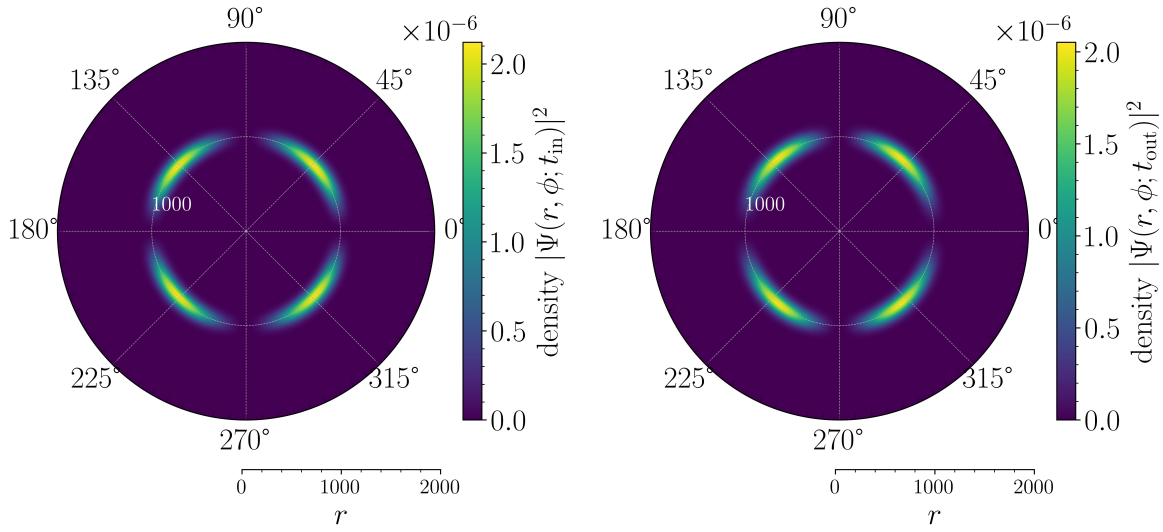

Figure 5.7: Polar surface of a two-dimensional wavepacket, Eq. (5.82), for the case the incoming wavepacket is the eigenchannel of the S-matrix. Left panel: a snapshot of the incoming wave packet far before the scattering center. Right panel: a snapshot of the outgoing wavepacket at a large distance from the center and has identical angular distribution as for the incoming. Here the numeric parameters are the same as Fig. 5.6.

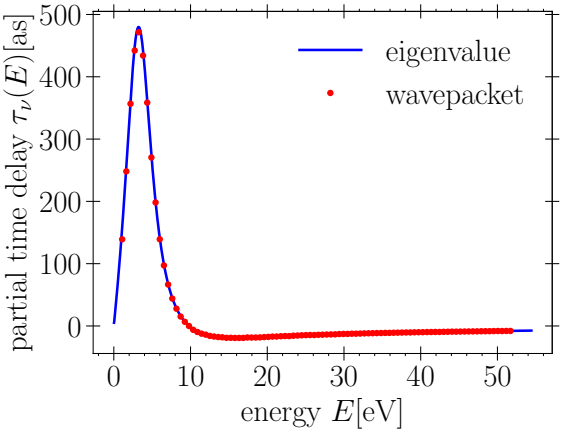

Figure 5.8: Partial time delay as a function of energy for channel $\nu = 0$, for two prospectives, the energy derivative of the phase of eigenvalues of the S-matrix, Eq. (5.78) and the wavepacket propagating.

5.4.2 Photoelectron wavepacket and photoionization time delay

A photoelectron wavepacket is a quantum mechanical entity that describes the behavior of an electron that has been ejected from an atom or molecule by the absorption of a photon. The ejected electron can be described by a wavepacket, which is a superposition of many different energy states. One of the key features of a photoelectron wavepacket is its coherence, which arises from the interference of the different energy states that make up the wavepacket. This coherence can be observed in experiments that measure the properties of the ejected electrons, such as their momentum distributions or their angular distributions. By studying the behavior of a wavepacket, one can gain insights into the underlying quantum mechanical processes that govern the behavior of atoms and molecules such as photoionization time delay.

In the weak field regime, the first-order perturbation theory is sufficient to describe the generation of a photoelectron wavepacket for a certain system. By inserting the 1st-order perturbation, Eq. (4.15), into the photoelectron expression, Eq. (2.19), we obtain

$$\Psi(\vec{r}, E; t) = -\mathrm{i}\sum_m \int \mathrm{d}E'\; d_m^{(-)}(E')\; \mathrm{e}^{-\mathrm{i}E't} \int_{-\infty}^{t} \mathrm{d}t'\; F(t')\; \mathrm{e}^{\mathrm{i}(E'-E)t'}\; \Phi_m^S(\vec{r}, E'), \tag{5.86}$$

where the partial matrix-element $d_m^{(-)}$ defined in Eq. (5.64) and Φ_m^S in Eq. (5.53). The energy E is donated to $E \equiv \hbar\omega + I_p$, where ω is the laser frequency, and I_p is the ionization potential. The laser field is an XUV pulse with a Gaussian envelop defines as $F(t) = \mathcal{E}_0\, \mathrm{e}^{-t^2/T^2} \cos(\omega t)$, where T is the pulse duration, and $\mathcal{E}_0$ the field strength.

To obtain the photoionization time delay using the wavepacket, we consider the wavepacket at a large distance far from the interaction region as $t \to \infty$, then calculate the center of mass for each direction given by

$$\langle r \rangle\,(\phi, t) = \frac{\int r\,|\Psi(\vec{r}, E; t)|^2\, r dr}{\int |\Psi(\vec{r}, E; t)|^2\, r dr}, \tag{5.87}$$

where ϕ indicates the direction. Once we have the expectation value, the time delay can be determined using Eq. (5.23).

Figure 5.9 shows a comparison between the photoionization time delay obtained from the phase of the dipole matrix in Eq. (5.70) and the expectation value of the photoelectron wavepacket in Eq. (5.87) for the Wood-saxon potential given by

$$V(r) = -\frac{1}{1 + \exp\left[\frac{r-L}{a}\right]}, \tag{5.88}$$

with $L = 50$ and $a = 0.01$, it supports a ground state of $E_0 = -27.2$ eV. Parameter L indicates how long the potential extended in space, and a implies the sharpness of the potential.

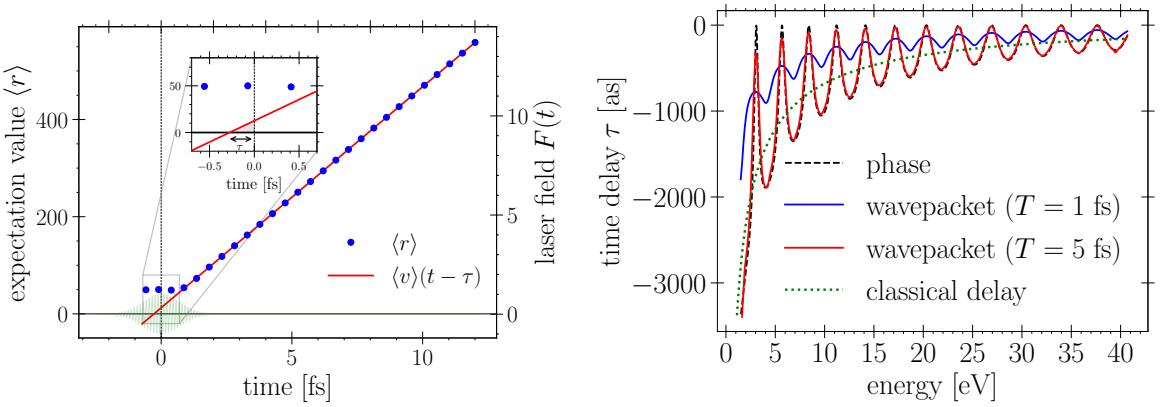

Figure 5.9: Photoionization time delay. Left panel: the expectation value for $E = 16$ eV as a function of time (blue bullet points) and linear fit with the offset τ driven by a Gaussian laser pulse with the duration of $T = 1$ fs. Right panel: time delay calculated from the phase of the dipole (black dashed line), wavepacket for two different pulse duration, and the classical delay (green dotted line).

Photoionization time delay is a half-scattering process; the electron is ejected from atoms or molecules driven by a laser. By means of the photoelectron wavepacket, we can record the expectation value during the evolving wavepacket. Far from the center of the interaction as $t \to \infty$, we project back in the expectation value, the offset (τ) in which the linear fitting meets the time axis denoting the photoionization time delay, see Fig. 5.9. The reference is the free particle which is assumed that originates at $t = 0$.

As can be seen in Fig. 5.9, for long pulse durations, which means a narrow peak in the energy domain, the time delay calculated from the expectation value of the wavepacket matches the one that obtained from the phase. The reason is that this narrow peak in the energy domain eliminates the effect of the structure of the dipole moment and is constant for a long pulse duration. On the other hand, for a short pulse, we observe a broad peak in the energy domain; as a consequence, the effect of the dipole moment is visible and appears in the time delay, as can be seen in the figure.

The oscillations observed in the time delay in Fig. 5.9 are a pure quantum effect that does not occur in the classical delay. Appendix C describes the approach for deriving the classical delay. These oscillations can be interpreted as a resonance in the infinite potential well since the Wood-saxon potential for the selected parameters behaves like an infinite well potential.

The approximate resonance positions are then given by [219, 227]

$$E_n \approx \frac{(n\pi\hbar)^2}{2\mu L^2} + V(0) \tag{5.89}$$

where in Eq. (5.88), $V(0) \sim -1$.

5.4.3 Anisotropic potential and half-collision checking

The two-center system described in Eq. (5.73) is considered here as an anisotropic potential and we calculate the photoionization time delay for this system.

Figure 5.10 shows the photoionization time delay from a wavepacket perspective. In the left panel, the time delay is depicted, which is the same as the time delay calculated from the matrix element's phase in Fig. 5.3. These identities indicate that both approaches produce the same results.

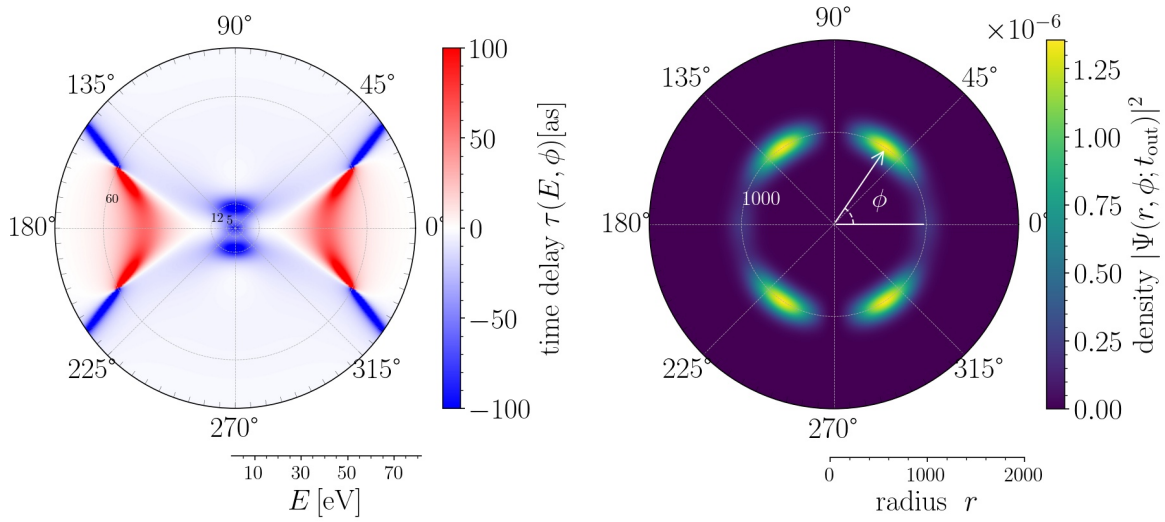

Figure 5.10: Time delay for an anisotropic potential, Eq. (5.73). Left panel: Photoionization time delay as a function of energy and direction driven with a Gaussian pulse with pulse duration of $T = 3\,\text{fs}$. Right panel: a snapshot of the photoelectron wavepacket, Eq. (5.86), away from the center for $E = 38\,\text{eV}$, we calculate the expectation value for each direction, ϕ, of the wavepacket.

The fringes in the photoelectron wavepacket in the right panel of Fig. 5.10 are accounted for the interference between the two atomic centers, which depends on the intra-atomic distance (R) and laser field direction.

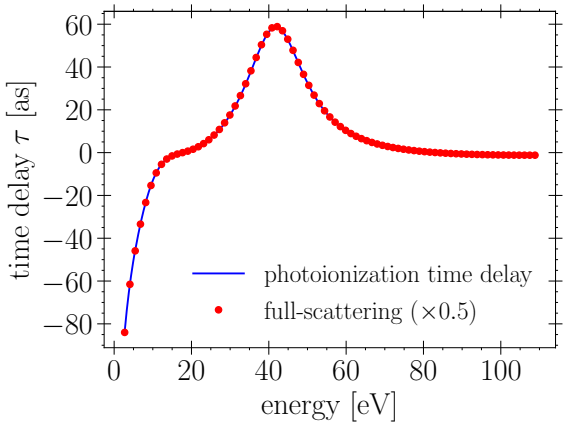

Figure 5.11: A comparison between the half-scattering and full-scattering process photoionization time delay for a specific direction of $\phi = 0$. The system and field parameters are the same as in Fig. 5.10.

As a last point, it is worth checking the half-scattering process in photoionization. For this matter, we keep the photoelectron wavepacket that is generated from Eq. (5.86) at $t \to \infty$. Then use this wavepacket as the initial wavepacket in Eq. (5.82) in order to consider a full scattering process. The photoionization time delay then is determined by investigating the final wavepacket as described in the subsection 5.4.1.

Figure 5.11 demonstrates a full- and half-scattering process for photoionization time delay and both are the same in which the time delay in full-scattering is two times the half-scattering process.

5.5 Summary

As the photoelectron wavepacket leaves the molecule, it experiences a highly anisotropic scattering potential; as a consequence, molecular ionization is a complicated phenomenon. This results in a highly structured time delay as a function of energy and angle in the molecular frame. With the use of scattering calculations, which were formulated using asymptotic solutions and the outgoing boundary condition, the angle-dependent photoionization delay $\tau(E, \varphi)$ was examined from two perspectives. A scattering perspective, the energy domain, and a wavepacket perspective, the time domain. We observed that both approaches produced the same results, with the difference that, in the time domain, we needed a long pulse to match the one obtained in the energy domain.

These two perspectives are two sides of the same coin, which were shown numerically. In

the case of spherical potentials, the Wigner-Smith time delay and the photoionization time delay are the same by a factor of 2, since channels have a well-defined time delay and there are selection rules. However, for anisotropic potentials, things are completely different, in which the photoionization time delay strongly relies on the initial state and dipole matrix elements. The deep link between the photoionization time delay and the photoionization matrix elements was revealed in the correlation of energy-domain photoionization phenomena. In this case, we observed the singularities in time delay, which are related to zeros in matrix elements.

The photoionization delay in molecular photoionization is a particularly promising field. Strong anisotropy of the potential landscape and coupling of the electronic and nuclear degrees of freedom make these studies especially attractive. Undoubtedly, time-resolved studies of atomic and molecular photoionization will continue in the future. The concept of the time delay will remain a strong focal point for these studies.

Chapter 6

Conclusions and Outlook

"The whole strenuous intellectual work of an industrious research worker would appear, after all, in vain and hopeless, if he were not occasionally through some striking facts to find that he had, at the end of all his criss-cross journeys, at last accomplished at least one step which was conclusively nearer the truth."

– Max Planck in his Nobel Lecture in 1920

This thesis primarily discussed atomic and molecular systems in both strong-field ionization and weak-field ionization regimes driven by ultrashort laser pulses. The investigated processes in this thesis include coherent control photoionization of the low-energy process, non-adiabatic photoionization (NAPI), with tailored ultrashort laser pulses, and attosecond photoionization time delay in molecular systems.

The basic concepts and equations that are needed to describe systems in this thesis were considered in chapter 2. Strong and weak field ionization regimes were reviewed, and their corresponding phenomena were explained; throughout the thesis, these phenomena and concepts were referred to many times. The most promising theoretical equation that can successfully describe experimental realizations is the Schrödinger equation. In chapter 2, we described this equation for a single active electron exposed to an external laser pulse and considered the dipole approximation on which this thesis was based.

Ultrashort laser pulse shaping was considered in chapter 2, where has been used in chapters 3, and 4. Ultrashort laser pulse shaping is a powerful tool for manipulating the temporal and spectral properties of ultrashort laser pulses. One of the trained laser pulses that were considered in this thesis is sinusoidal phase modulation, which is routinely investigated in coherent control experiments [78, 79, 80] since it allows for precise control over the properties of the laser pulse, which can lead to the manipulation of quantum systems.

Non-adiabatic photoionization, which is the direct consequence of ultrashort pulses, which are characterized by fast raising and falling of the pulse envelope, is difficult to control as it does not rely on phase details of the short ionizing pulse. It depends only on the laser pulse envelope. A question immediately arose whether it is possible to render NAPI sensitive to phase details of tailored pulses. This question became the motivation of chapter 3. In that chapter, we have investigated how non-adiabatic photo-ionization (NAPI) induced by ultrashort XUV pulses, can be influenced through specific pulse forms to exert coherent control as well-known for standard photo-ionization. We have introduced a catalyzing state, whose presence renders non-adiabatic ionization sensitive to the phase details of pulses. A state qualifies as catalyzing if it forms a resonance with the initial state $E_0 - E_{\text{cat}} \approx \omega$, where E_0 is the electron's binding energy. Moreover, since catalyzing states are easy to create, it opens up new avenues to coherently control ultrashort ionization. Pulse optimization, on the other hand, helped to find a proper pulse train in which we have maximum ionization of NAPI in the presence of this catalyzing state.

Time-dependent perturbation theory (TDPT), although, being an "old" topic, may allow for new insights for ultrashort pulses. In the ultrashort regime, the pulse duration plays a crucial role in controlling diverging terms occurring in TDPT. Chapter 4 covered how the

finite pulse duration can make TDPT work for higher intensities without diverging in higher orders.

Time-dependent perturbation theory showed some applications in the ultrashort regime, such as NAPI and interference stabilization. Non-adiabatic photoionization was considered in the frequency domain using second-order PT, which is the zero-photon process followed by one-photon absorption and emission. In this domain, we could have insight into NAPI and reveal some general properties. These properties include that it requires a weakly-bound initial state is required, and a deeply-bound state does not work. As another property, it relies on the Fourier transform of the squared pulse envelope. Furthermore, an oscillation pattern that appears in single-photon ionization when exposed to an intense ultrashort pulse has been explained using third-order PT. These structures that result in interference between different electron pathways reaching the same final energy in the continuum are the onsets of stabilization. With the help of the slowly varying envelope approximation, we could find a relation for the critical field strength point, where at this point the ionization probability decreases despite an increasing intensity.

A natural question with the availability of attosecond pulses is to measure the time it takes for a photoelectron to be ionized. In Chapter 5 we considered photoionization time delay in molecular systems with anisotropic potentials. In the case of spherical potentials there is a connection between the scattering time delay, Wigner-Smaith time delay [27, 28], and the photoionization time delay. The reason is that in these cases, the selection rules are applied and channels have a well-behaved time delay. Nevertheless, this is different in the case of anisotropic potentials, and the selection rule does not apply in molecular systems. Consequently, there is no trivial connection between scattering and photoionization time delay, we investigated this connection in Chapter 5.

The photoionization time delay was investigated from two perspectives: scattering and wavepacket. In the scattering approach, we studied the connection between the scattering time delay and photoionization time in which it is the energy derivative of the phase of the dipole matrix element. Moreover, from the wavepacket approach, we considered the photoelectron wavepacket far from the interaction region and computed its expectation value. The photoionization time delay was then defined as an offset in the expectation value.

The time delay was considered in this thesis, although some questions are still open to discussion. The formulation that has been used is based on asymptomatic solutions of the plane wave and the outgoing boundary condition to define the final molecular wave function and matrix element. There is, though, another approach that considers a particle in a “box”, known as the box solution. In this approach, the boundary condition is that the state should

reach zero in space at the edge of the box simulation. Since time delay is an attosecond quantity and is very sensitive to the errors caused by calculating bound and continuum states, comparing results from these two approaches would be recommended. However, in this thesis, we have used the Numerov method, Appendix A, which is very accurate in calculating state. As the last point, in chapter 5 we compared numerically the photoionization time delay from the two-mentioned perspectives. An analytical comparison is also possible to do.

Dealing with simple atomic systems to more complicated molecular structures while still trying to answer some basic questions was the goal of this thesis. However, there are plenty of basic questions that should be discussed, as we have already mentioned some of them.

Appendix A

Renormalized Numerov Method

Time-independent Schrödinger equation (TISE) is a partial differential equation that describes the wave function of a quantum system in a stationary state, where the energy and wave function are constant in time and has been solved many times as an ordinary differential equation [228, 229] or as a set of coupled equations [230, 29]. The numerical solution of the TISE is a common approach to finding approximate solutions to the wave function and energy levels of a quantum system. There are several numerical methods that can be used to solve the TISE, including the finite difference method [231, 232], matrix diagonalization [233], shooting method [234], variational method [235, 236], and Monte Carlo methods [237, 238]. Each of these methods has its own advantages and disadvantages, and the choice of method depends on the specific problem being solved and the desired accuracy. Numerical methods are widely used in quantum mechanics to study the properties of quantum systems and to make predictions about the behavior of atoms, molecules, and materials.

Finite difference approximations for derivatives are one of the simplest and oldest methods to solve differential equations. It was already known by L. Euler (1707-1783) in one dimension of space and was probably extended to dimension two by C. Runge (1856-1927). The advent of finite difference techniques in numerical applications began in the early 1950s, and their development was stimulated by the emergence of computers that offered a convenient framework for dealing with complex problems in science and technology. Today, finite difference approximation continues to be an essential tool for solving differential equations in a wide range of fields, including physics, engineering, finance, and biology. Its simplicity and versatility make it a popular choice for solving complex problems, and ongoing research continues to refine and improve the method.

The finite difference method (FDM) is a numerical method in which the partial differential equation is approximated using finite difference approximations. The wave function is discretized on a grid, and the differential equation is converted into a set of algebraic equations that can be solved iteratively. In the early 20th century, the method was further developed and applied by physicists and mathematicians such as Max Born, Robert S. Mulliken, and John von Neumann. There are several techniques for implementing the method, including, the central, forward, and backward difference method, alternating direction implicit (ADI) [239], Runge-Kutta [240], and Numerov method [241].

The Numerov method has many advantages, such as high accuracy, stability, efficient computation, and simplicity, making it a powerful and efficient numerical method for solving second-order differential equations. However, it has some drawbacks in coupled equations. Coupled equations are a set of two or more equations that are interconnected with one another. In other words, the solution to one equation is dependent on the solution of the other

equations in the system. These drawbacks include node-counting, which is generally a difficult task, and the coupled state has to be linearly independent solutions during Numerov propagation, but due to instability, it leads to dependent solutions. In 1978 Johnson [29] eliminated these flaws in the Numerov method by introducing a ratio matrix in which solutions remained linearly independent and redefining node-counting; this method is known as the Johnson renormalized Numerov method (JNM).

In the chapter 5 we treated anisotropic potentials, and for considering systems with these potentials we need to take advantage of JNM. In this chapter, we introduce JNM and resolve the matching point problem in continuum states by keeping the eigenvector corresponding to the minimum eigenvalue of the ratio matrix at the end of the box and using that eigenvector to backpropagate and calculate states. Furthermore, in JNM, the initial start is well-defined, but in some extreme cases, a proper initialization at the origin is needed in order to calculate eigenvalues precisely. For that matter, we find a way to modify some elements of the ratio matrix at the origin in order to reduce the error in calculating eigenvalues and eigenfunctions.

This chapter is structured as follows: In section A.1, we review the Numerov method and introduce the node-counting and bisection algorithms to calculate the Hamiltonian's eigenvalues. In section A.2, we review the Jonson renormalized Numerov method, in which we provide some modifications in the boundary condition at origin, resolve the matching point in the continuum state in the box solution, and finally offer some algorithms to calculate bound states and coupled-channel wavefunctions.

A.1 Introduction to Numerov method

The Numerov method was developed by Boris Numerov, a Russian astronomer and mathematician, in the early 20th century [242]. It is a numerical integration method used to solve second-order differential equations, especially those arising in problems of wave propagation. It is particularly suited for problems involving stiff differential equations and offers improved accuracy compared to other numerical methods like the Euler method. The Numerov method approximates the solution at each time step by a Taylor series expansion, making it highly effective for problems with small stepsizes. The radial Schrödinger equation is a second-order differential equation that in a compact form is given by

$$\left[\frac{\mathrm{d}^2}{\mathrm{d}r^2} + Q(r)\right]\psi(r) = 0, \tag{A.1}$$

where $\psi(r)$ is the wavefunction

$$Q(r) = \frac{2\mu}{\hbar^2}\left[E - \widetilde{V}(r)\right]. \tag{A.2}$$

The potential $\widetilde{V}(r)$ is assumed to be capable of supporting bound states and vanishes as $r \to \infty$, and the centrifugal potential is assumed to be included in $\widetilde{V}(r)$. The wavefunctions are required to be continuous together with their first derivatives and must satisfy the boundary conditions as

$$\begin{aligned} \psi(r=0) &= 0, \\ \lim_{r\to\infty} \psi(r) &\sim 0. \end{aligned} \tag{A.3}$$

We now describe the Numerov method (see also Landau and Páez [243]). By $\psi_n \equiv \psi(r_n)$ we suppose that the r_n are uniformly spaced with a separation of $\delta r = r_{n+1} - r_n$. A Taylor series for ψ_{n+1} gives

$$\psi_{n+1} = \psi_n + \delta r \psi_n' + \frac{\delta r^2}{2}\psi_n^{(2)} + \frac{\delta r^3}{6}\psi_n^{(3)} + \frac{\delta r^4}{24}\psi_n^{(4)} + \cdots, \tag{A.4}$$

where $\psi_n^{(k)}$ signifies the kth derivative $\mathrm{d}^k\psi/\mathrm{d}r^k$. Adding Eq. (A.4) to the series for ψ_{n-1} all the odd powers of δr vanish as

$$\psi_{n+1} + \psi_{n-1} = 2\psi_n + \delta r^2 \psi_n^{(2)} + \frac{\delta r^4}{24}\psi_n^{(4)} + \mathcal{O}(\delta r^6), \tag{A.5}$$

whereas $\psi_n^{(2)}$ follows exactly from Eq. (A.1) as $\psi_n^{(2)} = -Q_n\,\psi_n$, we have to consider $\frac{\mathrm{d}^4}{\mathrm{d}r^4}\psi(r) = -\frac{\mathrm{d}^2}{\mathrm{d}r^2}Q(r)\,\psi(r)$ to get

$$\psi_n^{(4)} = \frac{-Q_{n+1}\psi_{n+1} + Q_{n-1}\psi_{n-1} - 2Q_n\psi_n}{\delta r^2}. \tag{A.6}$$

where $Q_n \equiv Q(r_n)$. Plugging $\psi_n^{(2)}$ and $\psi_n^{(4)}$ into Eq. (A.5) and eliminating terms of order $\mathcal{O}(\delta r^6)$ and collecting terms contain ψ_n, ψ_{n-1}, and ψ_{n+1} one gets

$$(1 - T_{n+1})\,\psi_{n+1} - (2 + 10\,T_n)\,\psi_n + (1 - T_{n-1})\,\psi_{n-1} = 0 \tag{A.7}$$

which is the Numerov algorithm, where

$$T_n = -\frac{\delta r^2}{12}Q_n. \tag{A.8}$$

Using this algorithm, we can compute ψ_n from the values of ψ_{n-1} and ψ_{n-2}. This means, we either need to know the values of ψ_0 and ψ_1 and go forward through the lattice or know the values of ψ_N and ψ_{N-1} and go backward through the lattice. From the boundary condition, Eq. (A.3), $\psi_0 = 0$, but ψ_1 has to be determined. In most cases, we can replace ψ_1 with a small value, but it is a problem if the potential diverges at the boundary, e.g, $V(r) = -\frac{1}{r}$, $V(r) \sim \frac{\ell(\ell+1)}{r^2}$, etc, where ℓ is the angular momentum. In these cases, ψ_1 needs to be properly chosen by considering the physical system at hand.

The most straightforward procedure to deal with the initial start is using the power series expansion of the wavefunction about the origin. In the power series expansion, terms through the cubic should be retained in order to be compatible in accuracy with the Numerov method. Expanding the wavefunction in a power series as

$$\psi(r) = r^k \left(1 + br + cr^2 + \cdots\right). \tag{A.9}$$

Substituting Eq. (A.9) into Eq. (A.1) and evaluate the parameters k, b and c. The error in the computed eigenvalues is greatly reduced when correct values of the initial start are calculated.

Once we have the initial start, we can then calculate eigenvalues of Eq. (A.1) using the node-counting and the Numerov forward and backward integration in Eq. (A.7) with high precision, which we explain in the next subsection.

A.1.1 Eigenvalue calculation

The Numerov method requires the initial conditions ψ_0, ψ_1, and the energy E. However, for a bound state problem, the energy is the observable one wants to calculate. Remember that for a bound state with negative energy, it follows that the physical solution has to vanish as $r \to \infty$. Clearly, it is not possible to calculate all steps up to infinity, but since the wave function has an exponential decrease, it is sufficient to set the $r_{\max}$ such that $\psi(r_{\max}) \approx 0$. Thus one has to solve Eq. (A.1) for all energies in a given energy interval $[E_{\mathrm{L}}, E_{\mathrm{H}}]$ and pick out the energy satisfying the $\psi(r_{\max}) \approx 0$. The endpoint $r_{\max}$ is located inside the classically forbidden region. There are two regions, (i) classically forbidden region for both $r = 0$ and $r = r_{\max}$ and (ii) classically allowed region on either $r = 0$ ($\ell = 0$, 3D) or $r = r_{\max}$ (continuum states). A trial energy E is chosen, and Eq. (A.7) is integrated numerically. This solution is done in two parts, a forward integration starting at $r_0 = 0$ and a backward integration starting at $r_{\max}$. They meet at a common matching point r_{match} located within the classically allowed region. The matching point can be anywhere inside the region, but it should not be close to a node of the wavefunction. This procedure is iterated and usually converges rapidly to the eigenvalue E_n nearest in value to the initial guess. A bisection procedure can be used initially to isolate a single eigenvalue within a small energy interval with a specified node count. Let us assume we know two energies, E_{L}, and E_{H}, such that the desired eigenvalue lies between them $E_{\mathrm{L}} < E_n < E_{\mathrm{H}}$. The initial value for E_{L} can be the minimum value of the potential since the ground state can not be less than the potential's minimum.

In order to compute eigenvalues, we can count nodes by applying the oscillation theorem [244, 245], which states that if the eigenvalues are arranged in ascending order, then the

eigenfunction $\psi_n(x)(n = 0, 1, 2, \cdots)$ corresponding to the $(n+1)$th eigenvalue E_n has n nodes. The node-counting process is as follows:

1. set the energy parameter in the Schrödinger equation, Eq. (A.1), equal to
$$E = \frac{E_{\mathrm{L}} + E_{\mathrm{H}}}{2}. \tag{A.10}$$
2. do forward and backward integration and count the nodes.
3. if the node count is greater than n, set $E_{\mathrm{H}} = E$ and if it is less than or equal to n set $E_{\mathrm{L}} = E$
4. calculate new trial energy using Eq. (A.10) and repeat the process.
5. when $|E_{\mathrm{H}} - E_{\mathrm{L}}| < \epsilon$ the iteration is stopped, where ϵ, the tolerance factor, is a small positive number that here we fix it with $\epsilon \sim 10^{-12}$.

This method will converge linearly to the desired eigenvalue.

We can compute the continuum state $(E > 0)$ inside a box $[0, r_{\max}]$ as a box solution by forcing the wavefunction to reach zero at $r_{\max}$, in this case, continuum states will be discrete, and we can calculate eigenvalues through the node-counting as we did for bound states. The matching point for calculating the continuum state can be anywhere as long as not close to a node.

In summary of this section, the Numerov method is a highly accurate, computationally efficient, and stable method for solving differential equations. It is well suited for a variety of scientific and engineering applications, including solving problems in quantum mechanics, celestial mechanics, and numerical weather prediction [246]. However, this method is not suitable for coupled-channel equations since the definition of a node changes in this method, and traditional wavefunction node counting does not work. Moreover, without taking special precautions, this procedure would have severe overflow and linear dependence problems. Notwithstanding, there is a technique in which these difficulties do not occur that we introduce in the next section, which is known as renormalized Numerov method.

A.2 Johnson renormalized Numerov method

This section describes the renormalized Numerov method [228, 29, 247, 248], an efficient integration scheme for solving coupled equations. The formalism below is also applicable to single-channel problems following a trivial reduction from matrix to functional form. The coupled-channel Schrödinger equation is a matrix differential equation form of Eq. (A.1), in

which the M columns of a single $M \times M$ square matrix wavefunction $\mathbf{\Psi}(r)$, which the columns of $\mathbf{\Psi}(r)$ are linearly independent, satisfies

$$\left[\mathbf{I}\frac{\mathrm{d}^2}{\mathrm{d}r^2} + \mathbf{Q}(r)\right]\mathbf{\Psi}(r) = 0, \tag{A.11}$$

where $\mathbf{I}$ is the identity matrix and the boundary conditions at the origin is $\mathbf{\Psi}(r=0) = 0$. Here M is the size of the matrix. In Eq. (A.11) the matrix $\mathbf{Q}$ is given by

$$\mathbf{Q}(r) = \frac{2\mu}{\hbar^2}\left[E\mathbf{I} - \widetilde{\mathbf{V}}(r)\right], \tag{A.12}$$

with the matrix potential $\widetilde{\mathbf{V}}(r)$. Note that the centrifugal potential is assumed to be included in $\widetilde{\mathbf{V}}(r)$.

The matrix form of the Numerov algorithm in Eq. (A.7) is then given by

$$(\mathbf{I} - \mathbf{T}_{n+1})\,\mathbf{\Psi}_{n+1} - (2 + 10\mathbf{T}_n)\,\mathbf{\Psi}_n + (\mathbf{I} - \mathbf{T}_{n-1})\,\mathbf{\Psi}_{n-1} = 0. \tag{A.13}$$

where $\mathbf{T}$ is the matrix form of Eq. (A.8), and $\mathbf{\Psi}_n \equiv \mathbf{\Psi}(r_n)$.

In order to obtain the *renormalized Numerov* algorithm, two transformations are made to Eq. (A.13). First a convenient matrix defines as

$$\mathbf{F}_n = [\mathbf{I} - \mathbf{T}_n]\,\mathbf{\Psi}_n. \tag{A.14}$$

Substituting Eq. (A.14) into Eq. (A.13), we obtain in 3-step recurrence formula that is given by

$$\mathbf{F}_{n+1} - \mathbf{U}_n\mathbf{F}_n + \mathbf{F}_{n-1} = 0, \tag{A.15}$$

where

$$\mathbf{U}_n = (\mathbf{I} - \mathbf{T}_n)^{-1}\,(2\mathbf{I} + 10\mathbf{T}_n)\,. \tag{A.16}$$

Then defining ratio matrix as

$$\mathbf{R}_n = \mathbf{F}_{n+1}\mathbf{F}_n^{-1}. \tag{A.17}$$

By replacing Eq. (A.15) into Eq. (A.17), we obtain a 2-step forward recurrence relation given by

$$\mathbf{R}_n = \mathbf{U}_n - \mathbf{R}_{n-1}^{-1}. \tag{A.18}$$

The same procedure can be applied to obtain a backward recurrence relation as

$$\widetilde{\mathbf{R}}_n = \mathbf{U}_n - \widetilde{\mathbf{R}}_{n+1}^{-1}, \tag{A.19}$$

where $\widetilde{\mathbf{R}}_n = \mathbf{F}_{n-1}\mathbf{F}_n^{-1}$.

Physically, $\mathbf{F}_n$ is very similar in form to $\mathbf{\Psi}_n$, being *renormalized* by $\mathbf{I} - \mathbf{T}_n$. The ratio matrix $\mathbf{R}_n$ is then closly related to the ratio $\mathbf{\Psi}_{n+1}/\mathbf{\Psi}_n$. Iteration of Eq. (A.18) requires fewer matrix multiplications at each step than Eq. (A.13), and this makes calculations faster.

Equation (A.18) can be solved with the initial starting term $\mathbf{R}_0^{-1} = 0$ for forward and $\widetilde{\mathbf{R}}_N^{-1} = 0$ for backward propagation. The matrix $\mathbf{U}_n$, defined by Eq. (A.16), is symmetric since the matrix potential $\widetilde{\mathbf{V}}(r)$ is symmetric. It follows from this that the matrix $\mathbf{R}_n$ is also symmetric.

The definition of "nodes" in coupled equations is different. Johnson discovered a definition for a node in these equations, which is the zero of the determinant function $|\mathbf{\Psi}(r)|$. Nodes occur when the wavefunction's determinant changes between two adjacent points and can be implemented by the renormalized Numerov formalism. It follows from Eqs. (A.14) and (A.18) with requirement of $|\mathbf{I} - \mathbf{T}_n| > 0$ that $|\mathbf{R}_n| < 0$ only if $|\mathbf{\Psi}_n|$ changes sign between two point in a sequence, r_n and r_{n+1}. The node-counting method, which has been described in the previous section, also applies here with the difference that we monitor eigenvalues of the matrix $\mathbf{R}_n$ and increasing the count by one every time one of them is less than zero. Using node-counting and bisection algorithms, we can then calculate bound state energies, see Section A.1.1, with a slight difference that in the renormalized Numerov method, we only need to perform Eq. (A.18).

A.2.1 Proper initialization for extreme values of potential

The initial start of the JNM at $n = 0$, where the wavefunction is zero, in Eq. (A.18) is $\mathbf{R}_0^{-1} = 0$. However, in some cases where the wavefunction experiences a rapid onset, we observe a significant error in the calculation of energies, for example, in a two-dimensional system, the wavefunction for angular momentum $m = 0$ has a rapid onset at the origin $\psi(r)_{r\to 0} \sim \sqrt{r}$, and the reason is that the centrifugal potential for $m = 0$ proportional to $\sim -\frac{1}{8r^2}$. The error appears even in a very small grid spacing, see the second column of Fig. A.1. Therefore, we need an appropriate initialization at the origin. For this, we consider a single-channel renormalized Numerov for a free particle in one-, two- and three-dimensional in which the corresponding centrifugal potentials in Eq. (A.12) are given by

$$\begin{aligned} \widetilde{V}(r) &= 0, && \text{(1D)} \\ \widetilde{V}(r) &= \frac{m^2 - 1/4}{2r^2}, && \text{(2D)} \\ \widetilde{V}(r) &= \frac{\ell(\ell+1)}{2r^2}. && \text{(3D)} \end{aligned} \tag{A.20}$$

We choose potential zero, as an example since its solutions are known, and it can be extended to a general case. The exact solutions for the free particle in different dimensions are known

$$\begin{aligned} \psi(k,r) &\sim \{\sin(kr), \cos(kr)\} \quad \text{(1D)} \\ \psi(k,r) &\sim J_m(kr), \quad \text{(2D)} \\ \psi(k,r) &\sim j_\ell(kr), \quad \text{(3D)} \end{aligned} \tag{A.21}$$

where J_m and j_ℓ are Riccati-cylindrical-Bessel and Riccati-spherical-Bessel function respectively, and $k = \sqrt{2E}$. In the case of 1D, there are two channels, symmetric and antisymmetric. Thus the solutions are $\cos(kr)$ and $\sin(kr)$.

We solved TISE numerically using forward JNM and compared the solutions with the exact solutions in Eq. (A.21) by means of the earth mover's distance [249], which is easy to calculate for (normalized) one-dimensional distributions, $\rho(r)$. The error is then defined by

$$\varepsilon \equiv \int_0^R \mathrm{d}r \left| \int_0^r \mathrm{d}r' \left[\rho_{\text{exact}}(r') - \rho_{\text{numeric}}(r') \right] \right| \tag{A.22}$$

We examined this error in 1-, 2- and 3-dimensional systems for a free particle, and results

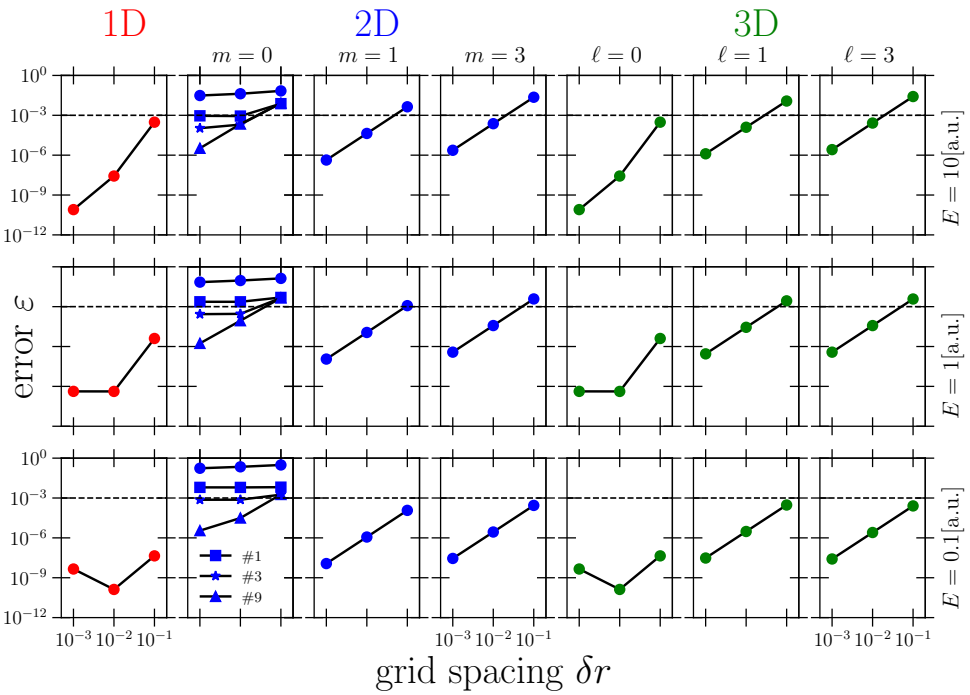

Figure A.1: Error calculation Eq. (A.22) for 1-, 2-, and 3-dimensional systems as a function of grid spacing δr for three different energies, and modifying a ratio matrix element in 2D leads to an increase in accuracy, as shown in the second column for different correction terms. The dashed line is the target error.

are shown in Fig. A.1 for three different energies. A reasonable target error distance is 10^{-3} (dashed line in Fig. A.1). As can be seen in Fig. A.1, for 1- and 3-dimensional, we can achieve the target error simply by choosing the grid spacing $\delta r = 0.01$ and no initialization is needed, but in the case of 2-dimensional for $m = 0$, a large error is observed which causes inaccuracy in calculating eigenvalues. A proper way to overcome this issue is that we can correct the element of the $\mathbf{R}_n$ matrix corresponding to $m = 0$ for a few grid points (# in Fig. A.1) according to the correct solution. We can do this using Eq. (A.14) and Eq. (A.17) as follows

$$\begin{aligned} F_{m,m}(r_n) &= [\delta_{m,m} - T_{m,m}(r_n)]\, \psi_m(k, r_n), \\ R_{m,m}(r_n) &= \frac{F_{m,m}(r_{n+1})}{F_{m,m}(r_n)} \end{aligned} \tag{A.23}$$

where $\psi_m(k, r)$ is defined in Eq. (A.21). By means of these corrections, even up to 3 grid points, we achieve the target error, as shown in the second column of Fig. A.1 and for higher correction terms the accuracy increases. This initialization works also for potentials with $k = \sqrt{2\,[E - V_0]}$ for $E > V_0$ or $k = \mathrm{i}\sqrt{2\,[V_0 - E]}$ for $E < V_0$. For the case that k is imaginary, one can use the modified Riccati-Bessel function of the first kind.

As the last point, one is able to achieve extreme accuracies with this method and these corrections.

A.2.2 Matching point and bound states solutions

Once we set a proper initialization and determine eigenvalues using node-counting and bisection algorithms, we can calculate eigenstates with the corresponding eigenvalues. In the bound state region, i.e., $E < V(r)$, we have classically allowed regions where the solutions have an oscillating behavior, and classically forbidden regions where the solutions exponentially decay as e^{-kr}. The border between these two regions is known as the "classical turning point". Since we can not avoid ending up an exponentially exploding branch in a classically forbidden region in numerics, a proper matching point where the forward and backward solutions meet is necessary. Given that in coupled equations, the definition of a node is different, thus, finding the correct position of the matching point is essential. To find the correct position, Johnson defined a matrix which is the difference between the forward and inverse of the backward propagation given by

$$\mathbf{D}(r_n) \equiv \mathbf{R}_n - \widetilde{\mathbf{R}}_{n+1}^{-1}, \tag{A.24}$$

the matching point happens when the determinant of this difference matrix turns to zero, i.e., $|\mathbf{D}(r_{\mathrm{match}})| \sim 0$ for a given eigenvalue. Finally, the bound state solutions can be calculated using the following steps:

1. calculate the potential matrix $\widetilde{\mathbf{V}}_n$
2. modify the necessary elements of $\mathbf{R}_1, \mathbf{R}_2, \cdots, \mathbf{R}_p$ according the system under investigation, see Section A.2.1, where p is the number of steps that needs to modify.
3. compute the bound state energy using node-counting and bisection algorithm in which the forward propagation in Eq. (A.18) should be performed
4. determine the matching point position r_{match} by means of the difference-matrix $\mathbf{D}(r)$
5. calculate the eigenvector corresponding to the minimum eigenvalue of $\mathbf{D}(r_{\text{match}})$ which is denoted as f_m
6. use the eigenvector in step (5), f_m, as the initial starting vector for forward and backward propagation using $f_n = \mathbf{R}_n^{-1} f_{n-1}$ and $f_n = \widetilde{\mathbf{R}}_n^{-1} f_{n+1}$ respectively.
7. calculate the bound state vector wavefunction through $\psi_n = (\mathbf{I} - \mathbf{T}_n) f_n$
8. normalize the wavefunction

These steps help to compute the solutions of the bound states with $E < 0$, and for continuum state with $E > 0$, we can use a "box" solution in which we force solutions to be zero at endpoint (r_{max}) of the box.

A.2.3 Discretized continuum states solutions

For $n \in A$ with A the asymptotic region where $V(r) \approx 0$, the matrix $\mathbf{Q}_n$ becomes diagonal, then from the matrix form of Eq. (A.8) and Eq. (A.14) we can write

$$\begin{aligned} \mathbf{T}_n &\sim -\mathbf{I}\frac{\delta r^2}{6}E, \\ \mathbf{F}_n &\sim \left(\mathbf{I} + \mathbf{I}\frac{\delta r^2}{6}E\right)\mathbf{\Psi}_n. \end{aligned} \tag{A.25}$$

Therefore, the ratio matrix in Eq. (A.17) becomes

$$\mathbf{R}_n \sim \frac{\mathbf{\Psi}_{n+1}}{\mathbf{\Psi}_n} \tag{A.26}$$

where for grid spacing $\delta r \to 0$, this matrix becomes identity

$$\mathbf{R}_n \sim \begin{pmatrix} 1 & 0 & \cdots & 0 \\ 0 & 1 & \cdots & 0 \\ \vdots & \vdots & \ddots & \vdots \\ 0 & 0 & \cdots & 1 \end{pmatrix}, \tag{A.27}$$

that means for decaying states $R_n \sim \mathrm{e}^{-k\delta r} \approx 1$ and for oscillating $R_n \sim \cos(k\delta r) \approx 1$. However, there is an exception in which the wavefunction for a given energy turns into zero at $n = N$. In this case, some components of $\mathbf{\Psi}_{n+1}$ become zero; subsequently, the corresponding components of the ratio matrix also become zero, and other components remain 1. Those elements of the ratio matrix, which are zero, correspond to the box solution's continuum eigenvalues. The case in which more than one element turns into zero indicates that the energy is degenerate, and the degree of degeneration is determined by the number of zeros in the ratio matrix.

The box continuum stats can thus be computed using the algorithm described in the previous subsection A.2.2, but with some modification in which we do not need to calculate the matching point and backward propagation. We only need to calculate the eigenvector corresponding to the minimum eigenvalue of $\mathbf{R}_n$ matrix, f_N, as the initial start vector and using $f_n = \mathbf{R}_n^{-1} f_{n+1}$. Then we follow steps 7 and 8 in algorithm A.2.2. This algorithm works for coupled and uncoupled equations, and eigenvalues and eigenfunctions can be accurately calculated.

A.2.4 Continuum states solutions

So far the JNM has been used to calculate bound states or discretized continuum states in a box. It is, however, also useful in calculating continuum states without a box. Here, any energy $E > 0$ is possible and states are calculated up to the asymptotic region, where analytic solutions are available.

A possible recipe for obtaining the coupled-channels solutions is as follows:

1. specify $\widetilde{\mathbf{V}}_n$ and E
2. modify the necessary elements of $\mathbf{R}_1, \mathbf{R}_2, \cdots, \mathbf{R}_p$ according the system under investigation, see Section A.2.1
3. calculate $\mathbf{T}_n$, $\mathbf{U}_n$ and $\mathbf{W}_n = \mathbf{I} - \mathbf{T}_n$, then $\mathbf{R}_n$ using Eq. (A.18), where $n = p+1, p+2, \cdots, N$ and the initial term is $\mathbf{R}_p^{-1}$ which is calculated in step (2).
4. record columns of the last term of the matrix $\mathbf{W}_N$ which are w_N^j, where index j specifies the independent solution (column index)
5. use backward propagating for each solution j

$$\begin{aligned} f_n &= \mathbf{R}_n^{-1} f_{n+1}, \\ \psi_n^j &= \mathbf{W}^{-1} f_n, \end{aligned} \tag{A.28}$$

where the initial starting vector is $f_N = w_N^j$.

6. determine the matrix wavefunction $\mathbf{\Psi}_n$ in which each column of this matrix specifies with ψ_n^j.

Using these 6 steps, the coupled-channels wavefunction is obtained.

In conclusion of this appendix, we considered the Johnson renormalized Numerov method, which is a suitable method for single- and coupled-channel equations. In addition, we provided some techniques for properly initializing the ratio matrix, resulting in an increase in the accuracy of calculating eigenvalues. Having accurate eigenvalues and eigenfunctions is a vital key to computing some sensitive quantities, namely time delay (see Chapter 5), which is an attosecond quantity.

Appendix B

Derivation of the Asymptotic Behavior of $\langle r \rangle$

For evaluating $\langle r \rangle$, we consider a two-dimensional free-particle wave packet,

$$\Psi(\vec{r}, t) = \frac{1}{2\pi} \int \Phi\left(\vec{k}\right) \exp\left\{\mathrm{i}\varphi\left(\vec{k}\right)\right\} \mathrm{d}^2 k, \tag{B.1}$$

where the phase

$$\varphi\left(\vec{k}\right) = \vec{k} \cdot \vec{r} - \frac{\vec{k}^{\,2}}{2\mu} t. \tag{B.2}$$

Note that, Eq. (B.1) is normalized to unity. Therefore $|\Phi(\vec{k})|^2$ is the momentum space probability density.

The wavefunction in momentum space $\Phi(\vec{k})$ is a relatively slowly varying function of k, where the phase $\varphi\left(\vec{k}\right)$ is generally large and rapidly varying. The rapid oscillations of $\exp\left\{\mathrm{i}\varphi\left(\vec{k}\right)\right\}$ over most of the range of integration means that the integrand averages to almost zero. Exceptions to this cancellation rule occur only at points where $\varphi\left(\vec{k}\right)$ has an extremum. The integral can therefore be estimated by finding all the points in the k-plane

where $\varphi\left(\vec{k}\right)$ has a vanishing derivative,

$$\nabla_{\vec{k}}\left(\vec{k}\cdot\vec{r}-\frac{\vec{k}^{\,2}}{2\mu}t\right)=0 \quad \Rightarrow \quad \vec{k}_0=\frac{\mu\vec{r}}{t}, \tag{B.3}$$

evaluating (approximately) the integral in the neighborhood of each of these points, and summing the contributions. This procedure is known as the *method of stationary phase.*

The phase $\varphi\left(\vec{k}\right)$ has a vanishing first derivative at $\vec{k}=\vec{k_0}$. In the neighborhood of this point, $\Phi\left(\vec{k}\right)$ can be expanded as a Taylor series,

$$\Phi\left(\vec{k}\right)=\Phi\left(\vec{k}_0\right)+\nabla_{\vec{k}}\,\Phi\left(\vec{k}\right)\Big|_{\vec{k}=\vec{k}_0}\left(\vec{k}-\vec{k}_0\right)+\frac{1}{2!}\nabla^2_{\vec{k}}\,\Phi\left(\vec{k}\right)\Big|_{\vec{k}=\vec{k}_0}\left(\vec{k}-\vec{k}_0\right)^2+.... \tag{B.4}$$

We also can rewrite $\varphi\left(\vec{k}\right)$ around $\vec{k}=\vec{k_0}$ as

$$\varphi\left(\vec{k}\right)=\frac{\mu\,\vec{r}^{\,2}}{2t}-\frac{1}{2}\left(\frac{t}{\mu}\right)\left(\vec{k}-\vec{k}_0\right)^2. \tag{B.5}$$

Inserting Eqs. (B.5) and (B.4) into Eq. (B.1), we obtain

$$\begin{aligned}\Psi(\vec{r},t)=&\frac{1}{2\pi}\exp\left\{\mathrm{i}\frac{\mu\vec{r}^{\,2}}{2t}\right\}\left[\Phi\left(\vec{k}_0\right)\int\exp\left\{-\frac{\mathrm{i}}{2}\left(\frac{t}{\mu}\right)\left(\vec{k}-\vec{k}_0\right)^2\right\}\mathrm{d}^2k\right.\\&+\nabla_{\vec{k}}\,\Phi\left(\vec{k}\right)\Big|_{\vec{k}=\vec{k}_0}\int\left(\vec{k}-\vec{k}_0\right)\exp\left\{-\frac{\mathrm{i}}{2}\left(\frac{t}{\mu}\right)\left(\vec{k}-\vec{k}_0\right)^2\right\}\mathrm{d}^2k\\&\left.+\frac{1}{2!}\nabla^2_{\vec{k}}\,\Phi\left(\vec{k}\right)\Big|_{\vec{k}=\vec{k}_0}\int\left(\vec{k}-\vec{k}_0\right)^2\exp\left\{-\frac{\mathrm{i}}{2}\left(\frac{t}{\mu}\right)\left(\vec{k}-\vec{k}_0\right)^2\right\}\mathrm{d}^2k+...\right],\end{aligned} \tag{B.6}$$

where integrating in the second term gives zero since $\int_{-\infty}^{\infty}x\,\mathrm{e}^{-\alpha x^2}\mathrm{d}x=0$. In addition, using the following integral relations

$$\begin{aligned}\int_{-\infty}^{\infty}\mathrm{e}^{-\mathrm{i}\alpha\vec{x}^{\,2}}\mathrm{d}^2x&=-\mathrm{i}\frac{\pi}{\alpha}=\frac{\pi}{\alpha}\,\mathrm{e}^{-\mathrm{i}\pi/2},\\\int_{-\infty}^{\infty}\vec{x}^{\,2}\,\mathrm{e}^{-\mathrm{i}\alpha\vec{x}^{\,2}}\mathrm{d}^2x&=\frac{\pi}{(\mathrm{i}\alpha)^2}=\frac{\mathrm{i}\pi}{\alpha^2}\mathrm{e}^{-\mathrm{i}\pi/2},\end{aligned} \tag{B.7}$$

Eq.(B.6) becomes

$$\Psi(\vec{r},t)\approx\exp\left\{\mathrm{i}\left(\frac{\mu\vec{r}^{\,2}}{2t}-\frac{\pi}{2}\right)\right\}\left[\left(\frac{\mu}{t}\right)\Phi\left(\vec{k}_0\right)-\frac{\mathrm{i}}{2}\left(\frac{\mu}{t}\right)^2\nabla^2_{\vec{k}_0}\,\Phi\left(\vec{k}_0\right)+...\right]. \tag{B.8}$$

The expectation value of $r=|\vec{r}|$ can be evaluated using the following equation

$$\langle r\rangle=\int\mathrm{d}^2r\;\Psi^*(\vec{r},t)\;|\vec{r}|\;\Psi(\vec{r},t). \tag{B.9}$$

By substituting the asymptotic form of $\Psi(\vec{r},t)$ in Eq. (B.8) into Eq. (B.9), we have

$$\begin{aligned}\langle r\rangle &= \left(\frac{t}{\mu}\right)^2 \int \mathrm{d}^2k_0\, |\vec{k}_0|\, \Phi^*\left(\vec{k}_0\right) \Phi\left(\vec{k}_0\right) - \frac{\mathrm{i}}{2}\int \mathrm{d}^2k_0\, |\vec{k}_0|\, \Phi^*\left(\vec{k}_0\right) \nabla^2_{\vec{k}_0}\, \Phi\left(\vec{k}_0\right) \\ &+ \frac{\mathrm{i}}{2}\int \mathrm{d}^2k_0\, |\vec{k}_0|\, \Phi\left(\vec{k}_0\right) \nabla^2_{\vec{k}_0}\, \Phi^*\left(\vec{k}_0\right) + \ldots \\ &= \langle v\rangle\, t + b + \mathcal{O}(t^{-1}), \quad (t\to\infty)\end{aligned} \tag{B.10}$$

where (for simplicity $\vec{k} = \vec{k}_0$)

$$\begin{aligned}\langle v\rangle\, t = \frac{\langle k\rangle}{\mu} t &= \left(\frac{t}{\mu}\right)\int |\vec{k}|\, \Phi^*\left(\vec{k}\right) \Phi\left(\vec{k}\right)\, \mathrm{d}^2k, \\ b &= -\frac{\mathrm{i}}{2}\int \vec{k}\left[\Phi^*\left(\vec{k}\right) \nabla^2_{\vec{k}}\Phi\left(\vec{k}\right) - \Phi\left(\vec{k}\right) \nabla^2_{\vec{k}}\Phi^*\left(\vec{k}\right)\right] \mathrm{d}^2k.\end{aligned} \tag{B.11}$$

By means of partial integration, we have

$$\Phi^*\left(\vec{k}\right) \nabla^2_{\vec{k}}\Phi\left(\vec{k}\right) - \Phi\left(\vec{k}\right) \nabla^2_{\vec{k}}\Phi^*\left(\vec{k}\right) = \nabla_{\vec{k}} \cdot \left[\Phi^*\left(\vec{k}\right) \nabla_{\vec{k}}\Phi\left(\vec{k}\right) - \Phi\left(\vec{k}\right) \nabla_{\vec{k}}\Phi^*\left(\vec{k}\right)\right], \tag{B.12}$$

Inserting Eq. (B.12) into Eq. (B.11), we then obtain

$$\begin{aligned}b = -\frac{\mathrm{i}}{2}\vec{k}\Big[\Phi^*\left(\vec{k}\right) \nabla_{\vec{k}}\, \Phi\left(\vec{k}\right) - \Phi\left(\vec{k}\right) \nabla_{\vec{k}}\Phi^*\left(\vec{k}\right)\Big]\Big|_{-\infty}^{\infty} \\ + \frac{\mathrm{i}}{2}\int \left[\Phi^*\left(\vec{k}\right) \nabla_{\vec{k}}\, \Phi\left(\vec{k}\right) - \Phi\left(\vec{k}\right) \nabla_{\vec{k}}\, \Phi^*\left(\vec{k}\right)\right] \mathrm{d}^2k,\end{aligned} \tag{B.13}$$

where the first term is zero and we can write b as

$$b = \frac{\mathrm{i}}{2}\int \left[\Phi^*\left(\vec{k}\right) \nabla_{\vec{k}}\, \Phi\left(\vec{k}\right) - \Phi\left(\vec{k}\right) \nabla_{\vec{k}}\, \Phi^*\left(\vec{k}\right)\right] \mathrm{d}^2k = \frac{\mathrm{i}}{2}\int \left[\Phi^*\left(\vec{k}\right)\right]^2 \frac{\partial}{\partial k}\left[\frac{\Phi\left(\vec{k}\right)}{\Phi^*\left(\vec{k}\right)}\right] \mathrm{d}^2k. \tag{B.14}$$

With $\Phi(\vec{k}) = |\Phi\left(\vec{k}\right)|\mathrm{e}^{\mathrm{i}2\delta(E)}$, Eq. (B.14) becomes

$$b = -2\int \left|\Phi^*\left(\vec{k}\right)\right|^2 \frac{\partial\delta(E)}{\partial k}\mathrm{d}\vec{k} = -2\left\langle\frac{\partial\delta(E)}{\partial k}\right\rangle = -2\left\langle\frac{k}{\mu}\frac{\partial\delta(E)}{\partial E}\right\rangle = -2\left\langle v\frac{\partial\delta(E)}{\partial E}\right\rangle, \tag{B.15}$$

where $v = p/\mu$, and $E = p^2/2\mu$.

If the energy spectrum of the wave packet is sharply peaked, we can replace v by $\langle v\rangle$. Therefore Eq. (B.10) becomes asymptotically

$$\langle r\rangle = \langle v\rangle\,(t-\tau), \quad (t\to\infty) \tag{B.16}$$

where

$$\tau = 2\left\langle\frac{\partial\delta(E)}{\partial E}\right\rangle, \tag{B.17}$$

is the s-wave result.

Appendix C

Classical Time Delay

In this appendix we consider classical time delay for a 2D *spherical* potential. However, one can try considering the time delay for an anisotropic potential, but since the initial condition is challenging to determine, we confine ourselves to a spherical potential.

The Hamiltonian for a 2D system is given by

$$\hat{H} = \frac{p_x^2}{2\mu} + \frac{p_y^2}{2\mu} + V(x, y). \tag{C.1}$$

Assuming the particle is initially located at the following boundary conditions

$$\begin{aligned} p_x(0) = a, \quad p_y(0) = 0 \\ y_0 = b, \quad x_0 = 0, \end{aligned} \tag{C.2}$$

and let it fly. Since the potential is spherical, for an arbitrary value of E, the parameters a and b can be determined using

$$E = \frac{a^2}{2} + V(b). \tag{C.3}$$

On the other hand, we have the angular momentum in 2D that is given by

$$M = \vec{r} \times \vec{p} = xp_y - yp_x, \tag{C.4}$$

where $r = \sqrt{x^2 + y^2}$ and $p = \sqrt{p_x^2 + p_y^2}$. Substituting condition in Eq. (C.2) into Eq. (C.4) then we obtain

$$M = ab. \tag{C.5}$$

Inserting Eq. (C.5) into Eq. (C.3), we obtain an equation of

$$\frac{a^2}{2} + V(M/a) - E = 0, \tag{C.6}$$

which should be solved for arbitrary energy E.

Once we have initial conditions, we can solve the following set of coupled equations simultaneously

$$\begin{aligned} \dot{p}_x &= -\frac{\partial H}{\partial x} = -\partial_x V(x,y), & \dot{p}_y &= -\frac{\partial H}{\partial y} = -\partial_y V(x,y), \\ \dot{x} &= \frac{\partial H}{\partial p_x} = \frac{p_x}{\mu}, & \dot{y} &= \frac{\partial H}{\partial p_y} = \frac{p_y}{\mu}. \end{aligned} \tag{C.7}$$

We can then calculate the trajectory as $t \to \infty$ where the particle behaves as the free particle

$$r(t) = v(t - \tau) \tag{C.8}$$

where $r(t) = \sqrt{x^2(t) + y^2(t)}$ from Eq. (C.7), and $v = \sqrt{2E}$. The time delay, τ, for a specific angular momentum, m, can be determined by comparing to the free particle trajectory which obtains using the above initial conditions as

$$x(t) = \frac{\sqrt{2E}}{\mu} t, \quad y(t) = b. \tag{C.9}$$

In general, if $\tau < 0$, then the particle spends less time near $x = 0$, because the potential is attractive and the particle speeds up. If $\tau > 0$, then the particle spends more time near $x = 0$, typically because it slows down or gets temporarily trapped in the potential.

Appendix D

Temporal Airy Pulse

In ultrashort laser shaping, a temporal Airy pulse is a specific type of laser pulse that has a unique and distinctive temporal profile. It is named after the Airy function, which describes the shape of the pulse's intensity profile over time. The temporal Airy pulse is characterized by a central peak with multiple surrounding lobes, similar to the shape of an Airy function in space [250].

This unique temporal profile of the Airy pulse has several applications in ultrashort laser shaping, including the ability to create ultrafast optical needles for high-resolution imaging and the ability to control the propagation of the pulse through complex media [250, 251, 252].

The temporal Airy pulse is created through a spectral phase with $\varphi(\omega' - \omega) = \alpha(\omega' - \omega)^3 T^3/6$, where α is the "airy parameter". The vector potential for this spectral phase in the frequency domain is given by

$$\underline{\tilde{A}}(\omega') = \mathcal{N}\mathcal{A}_0 \exp\left[-(\omega' - \omega)^2 T^2/8 \ln 2 + \mathrm{i}\alpha(\omega' - \omega)^3 T^3/6\right] \tag{D.1}$$

Fourier transform of the vector potential

$$A(t) = \frac{\mathcal{A}_0}{2} \mathcal{F}\left[\underline{\tilde{A}}(\omega') + \underline{\tilde{A}}^*(-\omega')\right]. \tag{D.2}$$

In order to get the Fourier-Transform, we take advantage of a variable as $u = (\omega' - \omega)T/2 + \mathrm{i}/a$, where $a = 9\alpha/2$, therefore

$$A(t) = \mathcal{N}\mathcal{A}_0 \mathrm{e}^{-\mathrm{i}\omega t + \frac{2}{a}(\frac{1}{3a} - \frac{t}{T})} \int_{-\infty}^{\infty} \mathrm{e}^{\mathrm{i}\frac{a}{3}u^3 + \mathrm{i}(\frac{1}{a} - \frac{2t}{T})u} \mathrm{d}u. \tag{D.3}$$

This integral is similar to the Airy function with the relation of

$$\mathrm{Ai}(z) = \frac{1}{2\pi} \int_{-\infty}^{\infty} \exp\left[\mathrm{i}\eta^3/3 + \mathrm{i}z\eta\right] \mathrm{d}\eta, \tag{D.4}$$

as a result using the Airy function Eq. (D.3) becomes ($T \to T/\sqrt{2\ln 2}$)

$$A(t) = \mathcal{N}\mathcal{A}_0 2\pi (\frac{2}{9\alpha})^{\frac{1}{3}} \mathrm{e}^{\frac{4}{9\alpha}(\frac{2}{27\alpha} - \frac{\sqrt{2\ln 2}\, t}{T})} \mathrm{Ai}\left(\left[\frac{2}{9\alpha} - \frac{\sqrt{8\ln 2}\, t}{T}\right](\frac{2}{9\alpha})^{\frac{1}{3}}\right) \cos(\omega t) \tag{D.5}$$

where Ai describes the Airy function. Reformulating Eq. (D.5) as

$$A(t) = \mathcal{A}_\alpha \, \mathrm{e}^{(\frac{2}{9\alpha})^{2/3}(\frac{2/3\tau - t}{\Delta\tau})} \mathrm{Ai}\left(\frac{\tau - t}{\Delta\tau}\right) \cos(\omega t), \tag{D.6}$$

where $\mathcal{A}_\alpha = \mathcal{A}_0 \sqrt{4\pi}\, \tau$. Equation (D.6) shows that the temporal pulse shape exponentially decay and the Airy function shifted by $\tau = \left(\frac{2}{9\alpha}\right)^{1/3} T/\sqrt{8\ln 2}$ and stretched by $\Delta\tau = \left(\frac{9\alpha}{2}\right)^{1/3} T/\sqrt{8\ln 2}$. Figure D.1 shows the pulse in Eq.(D.6) for different sing of the cubic parameter (α).

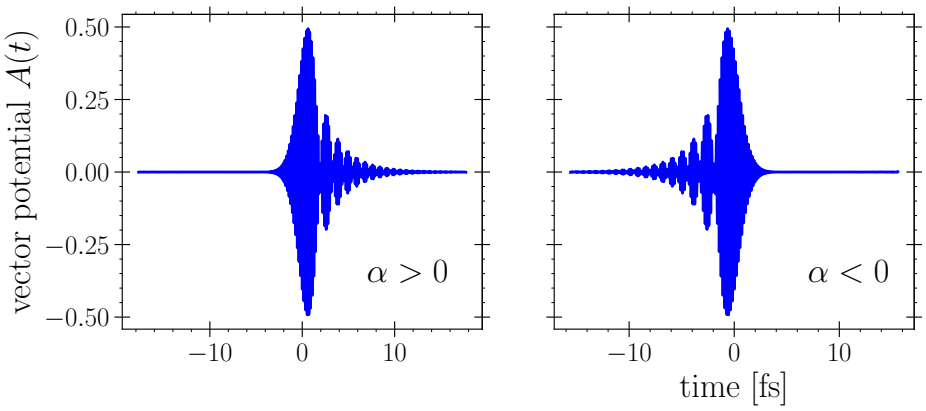

Figure D.1: An example of the temporal Airy pulse Eq.(D.6) with the fundamental pulse parameters of the pulse duration $T = 1\,\mathrm{fs}$, carrier frequency $\omega = 23.13\,\mathrm{eV}$, intensity $I = 10^{16}\,\mathrm{W/cm^2}$, and airy parameters $\alpha = \pm 0.6$.

For the limit of $\alpha \to 0$, we take advantage of the asymptotic behavior of the Airy functions at infinity as

$$\lim_{z\to\infty} A(z) = \frac{1}{2\sqrt{\pi}\sqrt[4]{z}} \mathrm{e}^{-\frac{2}{3}z^{3/2}}, \tag{D.7}$$

where $z = [\frac{2}{9\alpha} - \frac{2t}{T}](\frac{2}{9\alpha})^{\frac{1}{3}} = [1 - \frac{9\alpha t}{T}](\frac{2}{9\alpha})^{\frac{4}{3}}$, using Taylor expansion

$$\begin{aligned} z^{3/2} &= \left(\frac{2}{9\alpha}\right)^2 \left[1 - \frac{3}{2}\frac{9\alpha}{T}t + \frac{3}{8}(\frac{9\alpha}{T})^2 t^2 + \cdots\right], \\ z^{1/4} &= \left(\frac{2}{9\alpha}\right)^{1/3} \left[1 - \frac{1}{4}\frac{9\alpha}{T}t - \frac{3}{32}(\frac{9\alpha}{T})^2 t^2 + \cdots\right]. \end{aligned} \tag{D.8}$$

Substituting Eq. (D.8) into Eq. (D.7), one can write

$$\lim_{z\to\infty} A(z) = \frac{1}{2\sqrt{\pi}(\frac{2}{9\alpha})^{1/3}[1 + \cdots]} \mathrm{e}^{[-\frac{4}{9\alpha}\frac{2}{27\alpha} + \frac{4}{9\alpha T}t - (\frac{1}{T})^2 t^2 + \cdots]}, \tag{D.9}$$

by inserting Eq. (D.9) into Eq. (D.5), we get the Fourier-limited pulse, which is given by

$$A(t) = \frac{T}{\sqrt{8\ln 2}} \mathcal{A}_0 \ \mathrm{e}^{-2\ln(2)t^2/T^2} \cos(\omega t), \tag{D.10}$$

where there is an extra prefactor compared to Eq. (2.41) since we picked an unnormalized asymptotic behavior.

Appendix E

Numerical Details of Perturbation Theory

The Finite Difference Method (FDM) is utilized to solve Eq. (4.15) as

$$\dot{a}^{[n]}_{\ell j}(t_i) = \frac{a^{[n]}_{\ell j,i+1} - a^{[n]}_{\ell j,i-1}}{2\delta t}, \tag{E.1}$$

where index i runs over time, ℓ over angular momentum, j over states, and n over perturbation orders. δt is the time step in the simulation.

Inserting Eq.(E.1) into Eq. (4.15), we obtain

$$a^{[n]}_{\ell j,i+1} = a^{[n]}_{\ell j,i-1} - 2\delta t \frac{\mathrm{i}}{\hbar} \sum_k d_{\ell jk}\, \mathrm{e}^{\mathrm{i}\omega_{\ell jk} t_i} A(t_i)\, a^{[n-1]}_{\ell k,i}, \tag{E.2}$$

where the initial start $a^{[0]}_{\ell k,0} = \delta_{k0}$. The matrix element $d_{\ell jk}$, Eq. (2.22), is determined by taking advantage of the Numerov technique (see Appendix A) to solve the time-independent Schrödinger equation.

Appendix F

Atomic Units

In this thesis, some equations are written in a unit system different from the canonical SI units. In atomic physics, the quantities are often expressed in terms of another system of units which helps simplify the numerics and the analytic expressions. This system is called "atomic units", short "a.u.". It is built on the introduction of four independent quantities in atomic units given in Table F.1

atomic unit of mass	m_e	$\approx 9.1 \times 10^{-31}$ [kg]	electron mass
atomic unit of electric charge	e	$\approx 1.6 \times 10^{-19}$ [C]	absolute value of electron charge
atomic unit of action	$\hbar$	$\approx 1.05 \times 10^{-34}$ [Js]	reduced Planck's constant
atomic unit of permittivity	$4\pi\epsilon_0$	$\approx 1.1 \times 10^{-10}$ [F/m]	inverse of Coulomb's constant

Table F.1: Fundamental atomic units.

Using combinations of powers of these units, one can construct atomic units for other

observables, as can be seen by looking at Table F.2, where SI and atomic units are given for some frequently occurring physical quantities.

Physical Quantity	Expression	Value (a.u.)	Value (SI)
Bohr constant	a_0	1	$\approx 5.29 \times 10^{-11}$ [m]
Coulomb's constant	$k_e = 1/4\pi\epsilon_0$	1	$\approx 8.988 \times 10^{9}$ [N $\cdot$ m^2/C^2]
energy	$E = m_e e^4/(4\pi\epsilon_0\hbar)^2$	1	$\approx 4.36 \times 10^{-18}$ [J]
time	$t = \hbar/E$	1	$\approx 2.419 \times 10^{-17}$ [s]
velocity	$v = a_0/t$	1	$\approx 2.188 \times 10^{6}$ [m/s]
electric field	$\varepsilon = E/ea_0$	1	$\approx 5.142 \times 10^{11}$ [V/m]

Table F.2: Some physical quantities in atomic units.

There are two quantities that it is worth mentioning, which are 1[eV] = 27.211369[a.u.] and the relations between the laser intensity in SI units and the electric field in atomic units

$$\mathcal{E}_0 \text{ [a.u.]} = \sqrt{\frac{I \text{ [W/cm}^2\text{]}}{I_0}}, \tag{F.1}$$

where $I_0 = 3.5095 \times 10^{16}$ [W/cm^2].

References

[1] Donna Strickland and Gerard Mourou. Compression of amplified chirped optical pulses. *Optics Communications*, **56**(3):219–221, 1985.

[2] Gérard Mourou Arthur Ashkin and Donna Strickland. Nobel Prize in Physics. https://www.nobelprize.org/prizes/physics/2018/summary/, (2018).

[3] Thomas Brabec and Ferenc Krausz. Intense few-cycle laser fields: Frontiers of nonlinear optics. *Rev. Mod. Phys.*, **72**:545–591, Apr 2000.

[4] P. Agostini, F. Fabre, G. Mainfray, G. Petite, and N. K. Rahman. Free-Free Transitions Following Six-Photon Ionization of Xenon Atoms. *Phys. Rev. Lett.*, **42**:1127–1130, Apr 1979.

[5] G Petite, P Agostini, and H G Muller. Intensity dependence of non-perturbative above-threshold ionisation spectra: experimental study. *Journal of Physics B: Atomic, Molecular and Optical Physics*, **21**(24):4097, dec 1988.

[6] A. Baltuška, T. Udem, M. Uiberacker, M. Hentschel, E. Goulielmakis, C. Gohle, R. Holzwarth, V. S. Yakovlev, A. Scrinzi, T. W. Hänsch, and F. Krausz. Attosecond control of electronic processes by intense light fields - Nature. **421**:611, feb 6 2003.

[7] David Gauthier, Primož Rebernik Ribič, Giovanni De Ninno, Enrico Allaria, Paolo Cinquegrana, Miltcho Bojanov Danailov, Alexander Demidovich, Eugenio Ferrari, Luca Giannessi, Benoˆit Mahieu, and Giuseppe Penco. Spectrotemporal Shaping of Seeded Free-Electron Laser Pulses. *Phys. Rev. Lett.*, **115**:114801, Sep 2015.

[8] Giovanni De Ninno, David Gauthier, Benoˆit Mahieu, Primož Rebernik Ribič, Enrico Allaria, Paolo Cinquegrana, Miltcho Bojanov Danailov, Alexander Demidovich, Eugenio Ferrari, Luca Giannessi, Giuseppe Penco, Paolo Sigalotti, and Matija Stupar.

Single-shot spectro-temporal characterization of XUV pulses from a seeded free-electron laser. *Nature Communications*, **6**, 08 2015.

[9] Ferenc Krausz and Misha Ivanov. Attosecond physics. *Rev. Mod. Phys.*, **81**:163–234, Feb 2009.

[10] Shapiro M and Brumer. *Quantum Control of Molecular Processes*. John Wiley Sons, Ltd, second edition edition, 2011.

[11] Warren S. Warren, Herschel Rabitz, and Mohammed Dahleh. Coherent Control of Quantum Dynamics: The Dream Is Alive. *Science*, **259**(5101):1581–1589, 1993.

[12] Koudai Toyota, Oleg I. Tolstikhin, Toru Morishita, and Shinichi Watanabe. Slow Electrons Generated by Intense High-Frequency Laser Pulses. *Phys. Rev. Lett.*, **103**:153003, Oct 2009.

[13] Koudai Toyota, Ulf Saalmann, and Jan M Rost. The envelope Hamiltonian for electron interaction with ultrashort pulses. *New Journal of Physics*, **17**(7):073005, jul 2015.

[14] Qi-Cheng Ning, Ulf Saalmann, and Jan M. Rost. Electron Dynamics Driven by Light-Pulse Derivatives. *Phys. Rev. Lett.*, **120**:033203, 2018.

[15] Sajad Azizi, Ulf Saalmann, and Jan M Rost. Non-adiabatic ionization with tailored laser pulses. *Journal of Physics B: Atomic, Molecular and Optical Physics*, **54**(13):134001, aug 2021.

[16] M. Born, W. Heisenberg, and P. Jordan. Zur Quantenmechanik. II. *Zeitschrift für Physik*, **35**(8-9):557–615, 1926.

[17] Paul Adrien Maurice Dirac. On the theory of quantum mechanics. *Proc. R. Soc. Lond. A*, 112(762):661–677, 1926.

[18] Paul A. M. Dirac. Quantum theory of emission and absorption of radiation. *Proc. Roy. Soc. Lond. A*, **114**:243, 1927.

[19] Mikhail V. Fedorov, Nikolai P. Poluektov, Alexander M. Popov, Olga V. Tikhonova, Vasily Yu. Kharin, and Ekaterina A. Volkova. Interference Stabilization Revisited. *IEEE Journal of Selected Topics in Quantum Electronics*, **18**(1):42–53, 2012.

[20] N B Delone and Vladimir P Krainov. Atomic stabilisation in a laser field. *Physics-Uspekhi*, **38**(11):1247, nov 1995.

[21] Wolfgang Pauli. *General Principles of Quantum Mechanics*. Springer Berlin Heidelberg, Berlin, Heidelberg, 1980.

[22] J. J. Sakurai. *Modern Quantum Mechanics*. Addison Wesley, 1 edition, September 1993.

[23] Utkarsh R. Patel and Eric Michielssen. Wigner-Smith Time Delay Matrix for Electromagnetics: Computational Aspects for Radiation and Scattering Analysis. *IEEE Transactions on Antennas and Propagation*, 69(7):3995–4010, 2021.

[24] Anatoli S Kheifets. Wigner time delay in atomic photoionization. *Journal of Physics B: Atomic, Molecular and Optical Physics*, **56**(2):022001, jan 2023.

[25] P Hockett, E Frumker, D M Villeneuve, and P B Corkum. Time delay in molecular photoionization. *Journal of Physics B: Atomic, Molecular and Optical Physics*, **49**(9):095602, apr 2016.

[26] Martin Huppert, Inga Jordan, Denitsa Baykusheva, Aaron von Conta, and Hans Jakob Wörner. Attosecond Delays in Molecular Photoionization. *Phys. Rev. Lett.*, **117**:093001, Aug 2016.

[27] Eugene P. Wigner. Lower Limit for the Energy Derivative of the Scattering Phase Shift. *Phys. Rev.*, **98**:145–147, Apr 1955.

[28] Felix T. Smith. Lifetime Matrix in Collision Theory. *Phys. Rev.*, **118**:349–356, Apr 1960.

[29] B. R. Johnson. The renormalized Numerov method applied to calculating bound states of the coupled-channel Schrödinger equation. *The Journal of Chemical Physics*, **69**(10):4678–4688, 1978.

[30] Thomas Brabec, editor. *Strong Field Laser Physics*. Springer New York, 2009.

[31] T.F. HEINZ. Chapter 5 - Second-Order Nonlinear Optical Effects at Surfaces and Interfaces. In H.-E. PONATH and G.I. STEGEMAN, editors, *Nonlinear Surface Electromagnetic Phenomena*, volume **29** of *Modern Problems in Condensed Matter Sciences*, pages 353–416. Elsevier, 1991.

[32] Sergei V. Bulanov, Timur Esirkepov, and Toshiki Tajima. Light Intensification towards the Schwinger Limit. *Phys. Rev. Lett.*, **91**:085001, Aug 2003.

[33] Maxim V. Shugaev, Chengping Wu, Oskar Armbruster, Aida Naghilou, Nils Brouwer, Dmitry S. Ivanov, Thibault J.-Y. Derrien, Nadezhda M. Bulgakova, Wolfgang Kautek, Baerbel Rethfeld, and *et al.* Fundamentals of ultrafast laserâ€“material interaction. *MRS Bulletin*, **41**(12):960–968, 2016.

[34] Adam D. Smith, Tadas Balčiūnas, Yi-Ping Chang, Cédric Schmidt, Kristina Zinchenko, Fernanda B. Nunes, Emanuele Rossi, VÍt Svoboda, Zhong Yin, Jean-Pierre Wolf, and Hans Jakob Wörner. Femtosecond Soft-X-ray Absorption Spectroscopy of Liquids with a Water-Window High-Harmonic Source. *The Journal of Physical Chemistry Letters*, **11**(6):1981–1988, 2020. PMID: 32073862.

[35] Villy Sundström. Femtobiology. *Annual Review of Physical Chemistry*, **59**(1):53–77, 2008. PMID: 17892434.

[36] M. Braun, P. Gilch, and W. Zinth. *Ultrashort Laser Pulses in Biology and Medicine*. Springer Berlin Heidelberg, Berlin, Heidelberg, 2008.

[37] L. Gallmann, I. Jordan, H. J. Wörner, L. Castiglioni, M. Hengsberger, J. Osterwalder, C. A. Arrell, M. Chergui, E. Liberatore, U. Rothlisberger, and U. Keller. Photoemission and photoionization time delays and rates. *Structural Dynamics*, **4**(6):061502, 2017.

[38] A. Einstein. Über einen die Erzeugung und Verwandlung des Lichtes betreffenden heuristischen Gesichtspunkt. (German)[On a heuristic point of view concerning the production and transformation of light]. *Annalen der Physik*, **322**(6):132–148, 1905.

[39] Carsten Müller. Lecture on Multiphoton Physics. https://www.mpi-hd.mpg.de/imprs-qd/fileadmin/user_upload/Internal_School_2013/IMPRS_2013_CMueller.pdf, (2013).

[40] Maria Göppert-Mayer. Über Elementarakte mit zwei Quantensprüngen. (German)[About elementary acts with two quantum leaps]. *Annalen der Physik*, **401**(3):273–294, 1931.

[41] P. A. Franken, A. E. Hill, C. W. Peters, and G. Weinreich. Generation of Optical Harmonics. *Phys. Rev. Lett.*, **7**:118–119, Aug 1961.

[42] W. Kaiser and C. G. B. Garrett. Two-Photon Excitation in CaF_2: Eu^{2+}. *Phys. Rev. Lett.*, **7**:229–231, Sep 1961.

[43] Misha Yu Ivanov, Michael Spanner, and Olga Smirnova. Anatomy of strong field ionization. *Journal of Modern Optics*, **52**(2-3):165–184, 2005.

[44] P.AGOSTINI. *The simple Rahman's Theory*, pages 1–6. 2004.

[45] C. J. Joachain, N. J. Kylstra, and R. M. Potvliege. *Atoms in Intense Laser Fields*. Cambridge University Press, 2011.

[46] P. Kruit, J. Kimman, H. G. Muller, and M. J. van der Wiel. Electron spectra from multiphoton ionization of xenon at 1064, 532, and 355 nm. *Phys. Rev. A*, **28**:248–255, Jul 1983.

[47] H G Muller, A Tip, and M J van der Wiel. Ponderomotive force and AC Stark shift in multiphoton ionisation. *Journal of Physics B: Atomic and Molecular Physics*, **16**(22):L679, nov 1983.

[48] S. H. Autler and C. H. Townes. Stark Effect in Rapidly Varying Fields. *Phys. Rev.*, **100**:703–722, 1955.

[49] N B Delone and Vladimir P Krainov. AC Stark shift of atomic energy levels. *Physics-Uspekhi*, **42**(7):669, jul 1999.

[50] Mehrdad Baghery, Ulf Saalmann, and Jan M. Rost. Essential Conditions for Dynamic Interference. *Phys. Rev. Lett.*, **118**:143202, 2017.

[51] M. P. M. de Souza, A. A. C. de Almeida, and S. S. Vianna. Dynamic Stark shift in Doppler-broadened four-wave mixing. *Phys. Rev. A*, **105**:053128, May 2022.

[52] Benjamin J. Sussman. Five ways to the nonresonant dynamic Stark effect. *American Journal of Physics*, **79**(5):477–484, 2011.

[53] P. Mulser, S. Uryupin, R. Sauerbrey, and B. Wellegehausen. Ponderomotive potential and dynamical Stark shift in multiphoton ionization. *Phys. Rev. A*, **48**:4547–4550, Dec 1993.

[54] P.Agostini and G.Petite. Photoelectric effect under strong irradiation. *Contemporary Physics*, **29**(1):57–77, 1988.

[55] T. S. Luk, T. Graber, H. Jara, U. Johann, K. Boyer, and C. K. Rhodes. Subpicosecond ultraviolet multiphoton electron spectroscopy of rare gases. *J. Opt. Soc. Am. B*, **4**(5):847–852, May 1987.

[56] R. R. Freeman, P. H. Bucksbaum, H. Milchberg, S. Darack, D. Schumacher, and M. E. Geusic. Above-threshold ionization with subpicosecond laser pulses. *Phys. Rev. Lett.*, **59**:1092–1095, Sep 1987.

[57] L. V. Keldysh. Ionization in the Field of a Strong Electromagnetic Wave. *J. Exp. Theor. Phys.*, **20**(5):1307–1314, 1965.

[58] S. Augst, D. Strickland, D. D. Meyerhofer, S. L. Chin, and J. H. Eberly. Tunneling ionization of noble gases in a high-intensity laser field. *Phys. Rev. Lett.*, **63**:2212–2215, Nov 1989.

[59] Eric Mevel, Pierre Breger, Rusty Trainham, Guillaume Petite, Pierre Agostini, Arnold Migus, Jean-Paul Chambaret, and Andre Antonetti. Atoms in strong optical fields: Evolution from multiphoton to tunnel ionization. *Phys. Rev. Lett.*, **70**:406–409, Jan 1993.

[60] Christopher Gerry and Peter Knight. *Introductory Quantum Optics*. Cambridge University Press, 2004.

[61] Emilio Pisanty, Daniel D Hickstein, Benjamin R Galloway, Charles G Durfee, Henry C Kapteyn, Margaret M Murnane, and Misha Ivanov. High harmonic interferometry of the Lorentz force in strong mid-infrared laser fields. *New Journal of Physics*, **20**(5):053036, may 2018.

[62] M. Førre, J. P. Hansen, L. Kocbach, S. Selstø, and L. B. Madsen. Nondipole Ionization Dynamics of Atoms in Superintense High-Frequency Attosecond Pulses. *Phys. Rev. Lett.*, **97**:043601, Jul 2006.

[63] A. Ludwig, J. Maurer, B. W. Mayer, C. R. Phillips, L. Gallmann, and U. Keller. Breakdown of the Dipole Approximation in Strong-Field Ionization. *Phys. Rev. Lett.*, **113**:243001, Dec 2014.

[64] Tianzhe Xu, Manoel Conde, Gwanghui Ha, Philippe Piot, and John Power. Ultrashort Laser Pulse Shaping and Characterization for Tailored Electron Bunch Generation. 10 2020.

[65] Antoine Monmayrant, Sébastien Weber, and Béatrice Chatel. A newcomer's guide to ultrashort pulse shaping and characterization. *Journal of Physics B: Atomic, Molecular and Optical Physics*, **43**(10):103001, may 2010.

[66] Rick Trebino. Ultrashort Laser Pulses I . https://www.brown.edu/research/labs/mittleman/sites/brown.edu.research.labs.mittleman/files/uploads/lecture6_0.pdf.

[67] A. M. Weiner. Femtosecond pulse shaping using spatial light modulators. *Review of Scientific Instruments*, **71**(5):1929–1960, 2000.

[68] K Eickhoff, L Feld, D Köhnke, L Englert, T Bayer, and M Wollenhaupt. Coherent control mechanisms in bichromatic multiphoton ionization. *Journal of Physics B: Atomic, Molecular and Optical Physics*, **54**(16):164002, sep 2021.

[69] Franz Hagemann, Oliver Gause, Ludger Wöste, and Torsten Siebert. Supercontinuum pulse shaping in the few-cycle regime. *Opt. Express*, **21**(5):5536–5549, Mar 2013.

[70] A. Assion M. Wollenhaupt and Th. Baumert. *Springer Handbook of Lasers and Optics*. Springer, Berlin, Heidelberg, 2012.

[71] R. Jason Jones and Jun Ye. Femtosecond pulse amplification by coherent addition in a passive optical cavity. *Opt. Lett.*, **27**(20):1848–1850, Oct 2002.

[72] Govind Agrawal. *Nonlinear Fiber Optics*. Academic Press, fifth edition edition, 2013.

[73] Esben Ravn Andresen, John M. Dudley, Dan Oron, Christophe Finot, and Hervé Rigneault. Nonlinear pulse shaping by coherent addition of multiple red-shifted solutions. *J. Opt. Soc. Am. B*, **28**(7):1716–1723, Jul 2011.

[74] Tiejun Zhang and Motoki Yonemura. Pulse Shaping of Ultrashort Laser Pulses with Nonlinear Optical Crystals. *Japanese Journal of Applied Physics*, **38**(11R):6351, nov 1999.

[75] Franklin D. Fuller, Daniel E. Wilcox, and Jennifer P. Ogilvie. Pulse shaping based two-dimensional electronic spectroscopy in a background free geometry. *Opt. Express*, **22**(1):1018–1027, Jan 2014.

[76] K. Sala, G. Kenney-Wallace, and G. Hall. CW autocorrelation measurements of picosecond laser pulses. *IEEE Journal of Quantum Electronics*, **16**(9):990–996, 1980.

[77] M. Wollenhaupt, A. Präkelt, C. Sarpe-Tudoran, D. Liese, T. Bayer, and T. Baumert. Femtosecond strong-field quantum control with sinusoidally phase-modulated pulses. *Phys. Rev. A*, **73**:063409, Jun 2006.

[78] Doron Meshulach and Yaron Silberberg. Coherent quantum control of two-photon transitions by a femtosecond laser pulse. *Nature*, **396**(6708):239–242, 11 1998.

[79] Tim Bayer, Matthias Wollenhaupt, and Thomas Baumert. Strong-field control landscapes of coherent electronic excitation. *Journal of Physics B: Atomic, Molecular and Optical Physics*, **41**(7):074007, mar 2008.

[80] M. Wollenhaupt, A. Präkelt, C. Sarpe-Tudoran, D. Liese, and T. Baumert. Quantum control and quantum control landscapes using intense shaped femtosecond pulses. *Journal of Modern Optics*, **52**(16):2187–2195, 2005.

[81] M. Shapiro and P. Brumer. *Quantum Control of Molecular Processes*. John Wiley and Sons, Ltd, 2011.

[82] H. Eichmann, A. Egbert, S. Nolte, C. Momma, B. Wellegehausen, W. Becker, S. Long, and J. K. McIver. Polarization-dependent high-order two-color mixing. *Phys. Rev. A*, **51**:R3414–R3417, May 1995.

[83] Fritz Ehlotzky. Atomic phenomena in bichromatic laser fields. *Physics Reports*, **345**(4):175–264, 2001.

[84] Manfred Lein and Matthias Wollenhaupt. Special Issue: Dynamics in Tailored Ultrashort Light Fields. *Journal of Modern Optics*, **64**(10-11):949–951, 2017.

[85] Doron Meshulach and Yaron Silberberg. Coherent quantum control of multiphoton transitions by shaped ultrashort optical pulses. *Phys. Rev. A*, **60**:1287–1292, Aug 1999.

[86] J. G. Story, D. I. Duncan, and T. F. Gallagher. Resonant inhibition of multiphoton ionization. *Phys. Rev. Lett.*, **70**:3012–3015, May 1993.

[87] Jie Li, Xiaoming Ren, Yanchun Yin, Kun Zhao, Andrew Chew, Yan Cheng, Eric Cunningham, Yang Wang, Shuyuan Hu, Yi Wu, Michael Chini, and Zenghu Chang. 53-attosecond X-ray pulses reach the carbon K-edge. *Nature Communications*, **8**(1), aug 4 2017.

[88] Thomas Gaumnitz, Arohi Jain, Yoann Pertot, Martin Huppert, Inga Jordan, Fernando Ardana-Lamas, and Hans Jakob Wörner. Streaking of 43-attosecond soft-X-ray pulses generated by a passively CEP-stable mid-infrared driver. *Opt. Express*, **25**(22):27506–27518, Oct 2017.

[89] N. Hartmann, G. Hartmann, R. Heider, M. S. Wagner, M. Ilchen, J. Buck, A. O. Lindahl, C. Benko, J. Grünert, J. Krzywinski, J. Liu, A. A. Lutman, A. Marinelli, T. Maxwell, A. A. Miahnahri, S. P. Moeller, M. Planas, J. Robinson, A. K. Kazansky, N. M. Kabachnik, J. Viefhaus, T. Feurer, R. Kienberger, R. N. Coffee, and W. Helml. Attosecond time–energy structure of X-ray free-electron laser pulses. *Nature Photonics*, **12**(4):215–220, mar 5 2018.

[90] S Serkez, G Geloni, S Tomin, G Feng, E V Gryzlova, A N Grum-Grzhimailo, and M Meyer. Overview of options for generating high-brightness attosecond x-ray pulses at free-electron lasers and applications at the European XFEL. *Journal of Optics*, **20**(2):024005, jan 2018.

[91] Andreas Wituschek, Lukas Bruder, Enrico Allaria, Ulrich Bangert, Marcel Binz, Roberto Borghes, Carlo Callegari, Giulio Cerullo, Paolo Cinquegrana, Luca Giannessi, Miltcho Danailov, Alexander Demidovich, Michele Di Fraia, Marcel Drabbels, Raimund Feifel, Tim Laarmann, Rupert Michiels, Najmeh Sadat Mirian, Marcel Mudrich, Ivaylo Nikolov, Finn H. O'Shea, Giuseppe Penco, Paolo Piseri, Oksana Plekan, Kevin Charles Prince, Andreas Przystawik, Primož Rebernik Ribič, Giuseppe Sansone, Paolo Sigalotti, Simone Spampinati, Carlo Spezzani, Richard James Squibb, Stefano Stranges, Daniel Uhl, and Frank Stienkemeier. Tracking attosecond electronic coherences using phase-manipulated extreme ultraviolet pulses. *Nature Communications*, **11**(1), feb 14 2020.

[92] Y. Hikosaka, T. Kaneyasu, M. Fujimoto, H. Iwayama, and M. Katoh. Coherent control in the extreme ultraviolet and attosecond regime by synchrotron radiation. *Nature Communications*, **10**(1), nov 1 2019.

[93] H. A. Kramers. The Collected Scientific Papers . *North Holland*, 1956.

[94] Walter C. Henneberger. Perturbation Method for Atoms in Intense Light Beams. *Phys. Rev. Lett.*, **21**:838–841, Sep 1968.

[95] Felipe Morales, Maria Richter, Serguei Patchkovskii, and Olga Smirnova. Imaging the Kramers-Henneberger atom. *Proceedings of the National Academy of Sciences*, **108**(41):16906–16911, 2011.

[96] M. Wollenhaupt, A. Präkelt, C. Sarpe-Tudoran, D. Liese, T. Bayer, and T. Baumert. Femtosecond strong-field quantum control with sinusoidally phase-modulated pulses. *Phys. Rev. A*, **73**:063409, Jun 2006.

[97] Alejandro Zielinski. Fully differential photo-electron spectra of hydrogen and helium atoms, January 2016.

[98] Armin Scrinzi. Accurate bound-state energies of helium in a strong magnetic field. *Phys. Rev. A*, **58**:3879–3883, Nov 1998.

[99] J M Rost. Analytical total photo cross section for atoms. *Journal of Physics B: Atomic, Molecular and Optical Physics*, **28**(19):L601, oct 1995.

[100] Ulf Saalmann, Sajal Kumar Giri, and Jan M. Rost. Adiabatic Passage to the Continuum: Controlling Ionization with Chirped Laser Pulses. *Phys. Rev. Lett.*, **121**:153203, Oct 2018.

[101] T. Baumert, T. Brixner, V. Seyfried, M. Strehle, and G. Gerber. Femtosecond pulse shaping by an evolutionary algorithm with feedback. *Applied Physics B: Lasers and Optics*, **65**(6):779–782, dec 1 1997.

[102] E. Kuprikov, A. Kokhanovskiy, K. Serebrennikov, and S. Turitsyn. Deep reinforcement learning for self-tuning laser source of dissipative solitons. *Scientific Reports*, **12**(1), may 3 2022.

[103] Everitt-P. van den Hengel A. et al Wigley, P. Fast machine-learning online optimization of ultra-cold-atom experiments. *Scientific Reports*, **6**:25890, 2016.

[104] Everitt-P. van den Hengel A. et al Wigley, P. Machine-Learning Online Optimization Package. https://m-loop.readthedocs.io/en/stable/, (2016).

[105] P. B. Corkum and Ferenc Krausz. Attosecond science. *Nature Physics*, **3**(6):381–387, 6 2007.

[106] B. A. Lippmann and Julian Schwinger. Variational Principles for Scattering Processes. I. *Phys. Rev.*, **79**:469–480, Aug 1950.

[107] R. B. Bird. The Feynman lectures on physics, Richard P. Feynman, Robert B. Leighton, and Matthew Sands, Addison-Wesley, Reading, Mass, Volume I, II (1964); Volume III (1965). *AIChE Journal*, **10**(6):794–794, 1964.

[108] A. Zee. *Quantum field theory in a nutshell.* 2003.

[109] Farhad H. M. Faisal. *Theory of Multiphoton Processes.* Physics of Atoms and Molecules Ser. may 31 1987.

[110] Nikolai B. Delone and Vladimir P. Krainov. *Multiple Ionization of Atoms*, pages 185–253. Springer Berlin Heidelberg, Berlin, Heidelberg, 1994.

[111] P. W. Langhoff, S. T. Epstein, and M. Karplus. Aspects of Time-Dependent Perturbation Theory. *Rev. Mod. Phys.*, **44**:602–644, Jul 1972.

[112] J. K. Bhattacharjee and D. S. Ray. Time-dependent perturbation theory in quantum mechanics and the renormalization group. *American Journal of Physics*, **84**(6):434–442, 2016.

[113] Q.H. Liu, Z. Li, M.N. Zhang, Q. Li, and B.J. Chen. Exponential functions of perturbative series and elimination of secular divergences in time-dependent perturbation theory in quantum mechanics. *Results in Physics*, **7**:890–894, 2017.

[114] Klaus Renziehausen, Philipp Marquetand, and Volker Engel. On the divergence of time-dependent perturbation theory applied to laser-induced molecular transitions. *Journal of Physics B: Atomic, Molecular and Optical Physics*, **42**(19):195402, sep 2009.

[115] D. Daems, S. Guérin, H. R. Jauslin, A. Keller, and O. Atabek. Optimized time-dependent perturbation theory for pulse-driven quantum dynamics in atomic or molecular systems. *Phys. Rev. A*, **68**:051402, Nov 2003.

[116] G. Petite, F. Fabre, P. Agostini, M. Crance, and M. Aymar. Nonresonant multiphoton ionization of cesium in strong fields: Angular distributions and above-threshold ionization. *Phys. Rev. A*, **29**:2677–2689, May 1984.

[117] Henrik Stapelfeldt and Tamar Seideman. Colloquium: Aligning molecules with strong laser pulses. *Rev. Mod. Phys.*, **75**:543–557, Apr 2003.

[118] Mihai Gavrila. Atomic stabilization in superintense laser fields. *Journal of Physics B: Atomic, Molecular and Optical Physics*, **35**(18):R147, sep 2002.

[119] Yong Zhao, Yueming Zhou, Jintai Liang, Qinghua Ke, Yijie Liao, Min Li, and Peixiang Lu. Dynamic interference in strong-field multiphoton excitation and ionization. *Phys. Rev. A*, **106**:063103, Dec 2022.

[120] F. Arecchi and R. Bonifacio. Theory of optical maser amplifiers. *IEEE Journal of Quantum Electronics*, **1**(4):169–178, 1965.

[121] R. Bonifacio, R.M. Caloi, and C. Maroli. The slowly varying envelope approximation revisited. *Optics Communications*, **101**(3):185–187, 1993.

[122] F. J. Dyson. The S Matrix in Quantum Electrodynamics. *Phys. Rev.*, **75**:1736–1755, Jun 1949.

[123] Richard P. Feynman. An Operator Calculus Having Applications in Quantum Electrodynamics. *Phys. Rev.*, **84**:108–128, Oct 1951.

[124] H. Primas. Generalized perturbation theory in operator form. *Rev. Mod. Phys.*, **35**:710–711, Jul 1963.

[125] Albert Messiah. *Quantum Mechanics, Volume II.* John Wiley and sons, inc. New York - London - Sydney, 1966.

[126] A. W. van der Vaart. *Asymptotic Statistics.* Cambridge Series in Statistical and Probabilistic Mathematics. Cambridge University Press, 1998.

[127] Koudai Toyota, Oleg I. Tolstikhin, Toru Morishita, and Shinichi Watanabe. Interference substructure of above-threshold ionization peaks in the stabilization regime. *Phys. Rev. A*, **78**:033432, Sep 2008.

[128] M. Wickenhauser, X. M. Tong, and C. D. Lin. Laser-induced substructures in above-threshold-ionization spectra from intense few-cycle laser pulses. *Phys. Rev. A*, **73**:011401, Jan 2006.

[129] M V Fedorov and A M Movsesian. Field-induced effects of narrowing of photoelectron spectra and stabilisation of Rydberg atoms. *Journal of Physics B: Atomic, Molecular and Optical Physics*, **21**(7):L155, apr 1988.

[130] M. Pont and M. Gavrila. Stabilization of atomic hydrogen in superintense, high-frequency laser fields of circular polarization. *Phys. Rev. Lett.*, **65**:2362–2365, Nov 1990.

[131] Oleg I. Tolstikhin. Siegert-state expansion for nonstationary systems. III. Generalized Born-Fock equations and adiabatic approximation for transitions to the continuum. *Phys. Rev. A*, **77**:032711, Mar 2008.

[132] R. Grobe and J. H. Eberly. Intense-field scattering and capture of an electron by a model atom. *Phys. Rev. A*, **47**:719–722, 1993.

[133] Philipp V. Demekhin and Lorenz S. Cederbaum. Dynamic Interference of Photoelectrons Produced by High-Frequency Laser Pulses. *Phys. Rev. Lett.*, **108**:253001, Jun 2012.

[134] Chuan Yu, Ning Fu, Tian Hu, Guizhong Zhang, and Jianquan Yao. Dynamic Stark effect and interference photoelectron spectra of $H_2{}^+$. *Phys. Rev. A*, **88**:043408, Oct 2013.

[135] Lun Yue and Lars Bojer Madsen. Dissociative ionization of $H_2{}^+$ using intense femtosecond XUV laser pulses. *Phys. Rev. A*, **90**:063408, Dec 2014.

[136] M. P. de Boer, J. H. Hoogenraad, R. B. Vrijen, L. D. Noordam, and H. G. Muller. Indications of high-intensity adiabatic stabilization in neon. *Phys. Rev. Lett.*, **71**:3263–3266, Nov 1993.

[137] R. R. Jones, D. W. Schumacher, and P. H. Bucksbaum. Population trapping in Kr and Xe in intense laser fields. *Phys. Rev. A*, **47**:R49–R52, Jan 1993.

[138] M. P. de Boer, J. H. Hoogenraad, R. B. Vrijen, R. C. Constantinescu, L. D. Noordam, and H. G. Muller. Adiabatic stabilization against photoionization: An experimental study. *Phys. Rev. A*, **50**:4085–4098, Nov 1994.

[139] N. J. van Druten, R. C. Constantinescu, J. M. Schins, H. Nieuwenhuize, and H. G. Muller. Adiabatic stabilization: Observation of the surviving population. *Phys. Rev. A*, **55**:622–629, Jan 1997.

[140] M. Førre, S. Selstø, J. P. Hansen, and L. B. Madsen. Exact Nondipole Kramers-Henneberger Form of the Light-Atom Hamiltonian: An Application to Atomic Stabilization and Photoelectron Energy Spectra. *Phys. Rev. Lett.*, **95**:043601, Jul 2005.

[141] L. Landau and E.M. Lifshitz. *Quantum Mechanics. Non-relativistic Theory.* Addison-Wesley, Reading, MA, 2nd edition edition, 1965.

[142] Wolfgang Pauli. *Writings on Physics and Philosophy*, pages 13–26. Springer Berlin Heidelberg, Berlin, Heidelberg, 1994.

[143] H. Salecker and E. P. Wigner. Quantum Limitations of the Measurement of Space-Time Distances. *Phys. Rev.*, **109**:571–577, Jan 1958.

[144] Aharon Casher and Benni Reznik. Back reaction of clocks and limitations on observability in closed systems. *Physical Review A*, **62**(4):042104–042101, 2000.

[145] Massimiliano Sassoli de Bianchi. Time-delay of classical and quantum scattering processes: a conceptual overview and a general definition. *Open Physics*, **10**(2):282–319, 2012.

[146] E. Shigemasa, J. Adachi, M. Oura, and A. Yagishita. Angular Distributions of $1s\sigma$ Photoelectrons from Fixed-in-Space N_2 Molecules. *Phys. Rev. Lett.*, **74**:359–362, Jan 1995.

[147] Y Hikosaka and J H D Eland. Molecular-frame photoelectron angular distributions in inner-valence photoionization of N_2. *Journal of Physics B: Atomic, Molecular and Optical Physics*, **33**(16):3137, aug 2000.

[148] Lei Chen, Steven M. Anlage, and Yan V. Fyodorov. Statistics of Complex Wigner Time Delays as a Counter of S-Matrix Poles: Theory and Experiment. *Phys. Rev. Lett.*, **127**:204101, Nov 2021.

[149] H. Lamb. *Hydrodynamics*. Cambridge University Press, Cambridge, p. 395, 6th edition edition, 1953.

[150] J. C. COOKE. Note on the Principle of Stationary Phase. *IMA Journal of Applied Mathematics*, **22**(3):297–303, 11 1978.

[151] C.A.A. de Carvalho and H.M. Nussenzveig. Time delay. *Physics Reports*, **364**(2):83–174, 2002.

[152] Leonard Eisenbud. *The formal properties of nuclear collisions*. PhD thesis, 1948.

[153] M. Froissart, M. L. Goldberger, and K. M. Watson. Spatial Separation of Events in S-Matrix Theory. *Phys. Rev.*, **131**:2820–2826, Sep 1963.

[154] David Bohm. *Quantum theory*. Prentice-Hall, Englewood Cliffs, N. J., 1951.

[155] A. M. Lane and R. G. Thomas. R-Matrix Theory of Nuclear Reactions. *Rev. Mod. Phys.*, **30**:257–353, Apr 1958.

[156] W. Brenig and R. Haag. Allgemeine Quantentheorie der Stoßprozesse (German)[General quantum theory of collision processes]. *Fortschritte der Physik*, **7**(4-5):183–242, 1959.

[157] K.M. Watson M.L. Goldberger. *Collision Theory*. Wiley, New York p.485, 1964.

[158] H. M. Nussenzveig. Causality in Nonrelativistic Quantum Scattering. *Phys. Rev.*, **177**:1848–1856, Jan 1969.

[159] H. M. Nussenzveig. Time Delay in Quantum Scattering. *Phys. Rev. D*, **6**:1534–1542, Sep 1972.

[160] E. P. Kanter, Y. Hashimoto, I. Leuca, G. M. Temmer, K. R. Alvar, and W. M. Gibson. Separation of Compound and Direct Reaction Processes by the Crystal Blocking Technique. *Phys. Rev. Lett.*, **35**:1326–1328, Nov 1975.

[161] S. B. Crampton and H. T. M. Wang. Duration of hydrogen-atom spin-exchange collisions. *Phys. Rev. A*, **12**:1305–1312, Oct 1975.

[162] C. Maroni, I. Massa, and G. Vannini. Time delay measurements in a low-energy nuclear reaction from a bremsstrahlung experiment. *Physics Letters B*, 60(4):344–346, 1976.

[163] H. W. van der Hart. When does photoemission begin? *Science*, **328**(5986):1645–1646, 2010.

[164] M. Schultze, M. Fieß, N. Karpowicz, J. Gagnon, M. Korbman, M. Hofstetter, S. Neppl, A. L. Cavalieri, Y. Komninos, Th. Mercouris, C. A. Nicolaides, R. Pazourek, S. Nagele, J. Feist, J. Burgdörfer, A. M. Azzeer, R. Ernstorfer, R. Kienberger, U. Kleineberg, E. Goulielmakis, F. Krausz, and V. S. Yakovlev. Delay in Photoemission. *Science*, **328**(5986):1658–1662, jun 25 2010.

[165] M. Hentschel, R. Kienberger, Ch. Spielmann, G. A. Reider, N. Milosevic, T. Brabec, P. Corkum, U. Heinzmann, M. Drescher, and F. Krausz. Attosecond metrology. *Nature*, **414**(6863):509–513, 11 2001.

[166] M. Uiberacker, Th. Uphues, M. Schultze, A. J. Verhoef, V. Yakovlev, M. F. Kling, J. Rauschenberger, N. M. Kabachnik, H. Schröder, M. Lezius, K. L. Kompa, H.-G. Muller, M. J. J. Vrakking, S. Hendel, U. Kleineberg, U. Heinzmann, M. Drescher, and F. Krausz. Attosecond real-time observation of electron tunnelling in atoms. *Nature*, **446**(7136):627–632, 4 2007.

[167] Eleftherios Goulielmakis, Zhi-Heng Loh, Adrian Wirth, Robin Santra, Nina Rohringer, Vladislav S. Yakovlev, Sergey Zherebtsov, Thomas Pfeifer, Abdallah M. Azzeer, Matthias F. Kling, Stephen R. Leone, and Ferenc Krausz. Real-time observation of valence electron motion. *Nature*, **466**(7307):739–743, 8 2010.

[168] P. Eckle, A. N. Pfeiffer, C. Cirelli, A. Staudte, R. Dörner, H. G. Muller, M. Büttiker, and U. Keller. Attosecond Ionization and Tunneling Delay Time Measurements in Helium. *Science*, **322**(5907):1525–1529, 2008.

[169] M. Ossiander, F. Siegrist, V. Shirvanyan, R. Pazourek, A. Sommer, T. Latka, A. Guggenmos, S. Nagele, J. Feist, J. Burgdörfer, R. Kienberger, and M. Schultze. Attosecond correlation dynamics. *Nature Physics*, **13**(3):280–285, nov 7 2016.

[170] M. Schultze, M. Fieß, N. Karpowicz, J. Gagnon, M. Korbman, M. Hofstetter, S. Neppl, A. L. Cavalieri, Y. Komninos, Th. Mercouris, C. A. Nicolaides, R. Pazourek, S. Nagele, J. Feist, J. Burgdörfer, A. M. Azzeer, R. Ernstorfer, R. Kienberger, U. Kleineberg, E. Goulielmakis, F. Krausz, and V. S. Yakovlev. Delay in Photoemission. *Science*, **328**(5986):1658–1662, 2010.

[171] K. Klünder, J. M. Dahlström, M. Gisselbrecht, T. Fordell, M. Swoboda, D. Guénot, P. Johnsson, J. Caillat, J. Mauritsson, A. Maquet, R. TaÏeb, and A. L'Huillier. Probing Single-Photon Ionization on the Attosecond Time Scale. *Phys. Rev. Lett.*, **106**:143002, Apr 2011.

[172] D. Guénot, K. Klünder, C. L. Arnold, D. Kroon, J. M. Dahlström, M. Miranda, T. Fordell, M. Gisselbrecht, P. Johnsson, J. Mauritsson, E. Lindroth, A. Maquet, R. TaÏeb, A. L'Huillier, and A. S. Kheifets. Photoemission-time-delay measurements and calculations close to the 3s-ionization-cross-section minimum in Ar. *Phys. Rev. A*, **85**:053424, May 2012.

[173] Caryn Palatchi, J M Dahlström, A S Kheifets, I A Ivanov, D M Canaday, P Agostini, and L F DiMauro. Atomic delay in helium, neon, argon and krypton*. *Journal of Physics B: Atomic, Molecular and Optical Physics*, **47**(24):245003, dec 2014.

[174] M. Sabbar, S. Heuser, R. Boge, M. Lucchini, T. Carette, E. Lindroth, L. Gallmann, C. Cirelli, and U. Keller. Resonance Effects in Photoemission Time Delays. *Phys. Rev. Lett.*, **115**:133001, Sep 2015.

[175] Eva Lindroth and Jan Marcus Dahlström. Attosecond delays in laser-assisted photodetachment from closed-shell negative ions. *Phys. Rev. A*, 96:013420, Jul 2017.

[176] Reto Locher, Luca Castiglioni, Matteo Lucchini, Michael Greif, Lukas Gallmann, Jürg Osterwalder, Matthias Hengsberger, and Ursula Keller. Energy-dependent photoemission delays from noble metal surfaces by attosecond interferometry. *Optica*, **2**(5):405–410, May 2015.

[177] Zhensheng Tao, Cong Chen, Tibor Szilvási, Mark Keller, Manos Mavrikakis, Henry Kapteyn, and Margaret Murnane. Direct time-domain observation of attosecond final-state lifetimes in photoemission from solids. *Science*, **353**(6294):62–67, 2016.

[178] A. L. Cavalieri, N. Müller, Th. Uphues, V. S. Yakovlev, A. Baltuška, B. Horvath, B. Schmidt, L. Blümel, R. Holzwarth, S. Hendel, M. Drescher, U. Kleineberg, P. M. Echenique, R. Kienberger, F. Krausz, and U. Heinzmann. Attosecond spectroscopy in condensed matter. *Nature*, **449**(7165):1029–1032, 10 2007.

[179] Renate Pazourek, Stefan Nagele, and Joachim Burgdörfer. Attosecond chronoscopy of photoemission. *Rev. Mod. Phys.*, **87**:765–802, Aug 2015.

[180] Francesca Calegari, Giuseppe Sansone, Salvatore Stagira, Caterina Vozzi, and Mauro Nisoli. Advances in attosecond science. *Journal of Physics B: Atomic, Molecular and Optical Physics*, **49**(6):062001, feb 2016.

[181] Ferenc Krausz. The birth of attosecond physics and its coming of age. *Physica Scripta*, **91**(6):063011, may 2016.

[182] M F Ciappina, J A Pérez-Hernández, A S Landsman, W A Okell, S Zherebtsov, B Förg, J Schötz, L Seiffert, T Fennel, T Shaaran, T Zimmermann, A Chacón, R Guichard, A Zair, J W G Tisch, J P Marangos, T Witting, A Braun, S A Maier, L Roso, M Krüger, P Hommelhoff, M F Kling, F Krausz, and M Lewenstein. Attosecond physics at the nanoscale. *Reports on Progress in Physics*, **80**(5):054401, mar 2017.

[183] Eric Constant, Vladimir D. Taranukhin, Albert Stolow, and P. B. Corkum. Methods for the measurement of the duration of high-harmonic pulses. *Phys. Rev. A*, **56**:3870–3878, Nov 1997.

[184] J. Itatani, F. Quéré, G. L. Yudin, M. Yu. Ivanov, F. Krausz, and P. B. Corkum. Attosecond Streak Camera. *Phys. Rev. Lett.*, **88**:173903, Apr 2002.

[185] Vladislav S. Yakovlev, Ferdinand Bammer, and Armin Scrinzi. Attosecond streaking measurements. *Journal of Modern Optics*, **52**(2-3):395–410, 2005.

[186] Misha Ivanov and Olga Smirnova. How Accurate Is the Attosecond Streak Camera? *Phys. Rev. Lett.*, **107**:213605, Nov 2011.

[187] C.-H. Zhang and U. Thumm. Streaking and Wigner time delays in photoemission from atoms and surfaces. *Phys. Rev. A*, **84**:033401, Sep 2011.

[188] H.G. Muller. Reconstruction of attosecond harmonic beating by interference of two-photon transitions. *Applied Physics B*, **74**(S1):s17–s21, 6 2002.

[189] E S Toma and H G Muller. Calculation of matrix elements for mixed extreme-ultraviolet-infrared two-photon above-threshold ionization of argon. *Journal of Physics B: Atomic, Molecular and Optical Physics*, **35**(16):3435, aug 2002.

[190] J.M. Dahlström, D. Guénot, K. Klünder, M. Gisselbrecht, J. Mauritsson, A. L'Huillier, A. Maquet, and R. TaÏeb. Theory of attosecond delays in laser-assisted photoionization. *Chemical Physics*, **414**:53–64, 2013. Attosecond spectroscopy.

[191] S. Nandi, E. Plésiat, S. Zhong, A. Palacios, D. Busto, M. Isinger, L. Neoričić, C. L. Arnold, R. J. Squibb, R. Feifel, P. Decleva, A. L''Huillier, F. MartÍn, and M. Gisselbrecht. Attosecond timing of electron emission from a molecular shape resonance. *Science Advances*, **6**(31), jul 31 2020.

[192] S. Haessler, B. Fabre, J. Higuet, J. Caillat, T. Ruchon, P. Breger, B. Carré, E. Constant, A. Maquet, E. Mével, P. Salières, R. Ta¨eb, and Y. Mairesse. Phase-resolved attosecond near-threshold photoionization of molecular nitrogen. *Phys. Rev. A*, **80**:011404, Jul 2009.

[193] V. Loriot, A. Marciniak, S. Nandi, G. Karras, M. Hervé, E. Constant, E. Plésiat, A. Palacios, F. MartÍn, and F. Lépine. Attosecond Ionization Time Delay Around a Shape Resonance in Nitrogen Measured by the RABBIT-2ω method. page cg 3 2. Optica Publishing Group, 2021.

[194] Andrei Kamalov, Anna L. Wang, Philip H. Bucksbaum, Daniel J. Haxton, and James P. Cryan. Electron correlation effects in attosecond photoionization of CO_2. *Phys. Rev. A*, **102**:023118, Aug 2020.

[195] Xiaochun Gong, Wenyu Jiang, Jihong Tong, Junjie Qiang, Peifen Lu, Hongcheng Ni, Robert Lucchese, Kiyoshi Ueda, and Jian Wu. Asymmetric Attosecond Photoionization in Molecular Shape Resonance. *Phys. Rev. X*, **12**:011002, Jan 2022.

[196] H. Ahmadi, E. Plésiat, M. Moioli, F. Frassetto, L. Poletto, P. Decleva, C. D. Schröter, T. Pfeifer, R. Moshammer, A. Palacios, F. Martin, and G. Sansone. Attosecond photoionisation time delays reveal the anisotropy of the molecular potential in the recoil frame. *Nature Communications*, **13**(1), mar 10 2022.

[197] Saijoscha Heck, Denitsa Baykusheva, Meng Han, Jia-Bao Ji, Conaill Perry, Xiaochun Gong, and Hans Jakob Wörner. Attosecond interferometry of shape resonances in the recoil frame of CF_4. *Science Advances*, **7**(49):eabj8121, 2021.

[198] G. Sansone, F. Kelkensberg, J. F. Pérez-Torres, F. Morales, M. F. Kling, W. Siu, O. Ghafur, P. Johnsson, M. Swoboda, E. Benedetti, F. Ferrari, F. Lépine, J. L. Sanz-Vicario, S. Zherebtsov, I. Znakovskaya, A. L'Huillier, M. Yu. Ivanov, M. Nisoli, F. Mart´in, and M. J. J. Vrakking. Electron localization following attosecond molecular photoionization. *Nature*, **465**(7299):763–766, 6 2010.

[199] F. Kelkensberg, W. Siu, J. F. Pérez-Torres, F. Morales, G. Gademann, A. Rouzée, P. Johnsson, M. Lucchini, F. Calegari, J. L. Sanz-Vicario, F. Mart´in, and M. J. J.

Vrakking. Attosecond Control in Photoionization of Hydrogen Molecules. *Phys. Rev. Lett.*, **107**:043002, Jul 2011.

[200] Jérémie Caillat, Alfred Maquet, Stefan Haessler, Baptiste Fabre, Thierry Ruchon, Pascal Salières, Yann Mairesse, and Richard TaÏeb. Attosecond Resolved Electron Release in Two-Color Near-Threshold Photoionization of N_2. *Phys. Rev. Lett.*, **106**:093002, Mar 2011.

[201] I. A. Ivanov, A. S. Kheifets, and Vladislav V. Serov. Attosecond time-delay spectroscopy of the hydrogen molecule. *Phys. Rev. A*, 86:063422, Dec 2012.

[202] Vladislav V. Serov, Vladimir L. Derbov, and Tatyana A. Sergeeva. Interpretation of time delay in the ionization of two-center systems. *Phys. Rev. A*, **87**:063414, Jun 2013.

[203] D.J. Griffiths and D.F. Schroeter. *Introduction to Quantum Mechanics*. Cambridge University Press, 2018.

[204] B. Fetić, W. Becker, and D. B. Milošević. Can we measure the Wigner time delay in a photoionization experiment? *arXiv.2210.05219*, 2022.

[205] N. G. Kelkar and M. Nowakowski. Analysis of averaged multichannel delay times. *Phys. Rev. A*, **78**:012709, Jul 2008.

[206] John A. Wheeler. On the Mathematical Description of Light Nuclei by the Method of Resonating Group Structure. *Phys. Rev.*, **52**:1107–1122, Dec 1937.

[207] Lei Chen, Steven M. Anlage, and Yan V. Fyodorov. Generalization of Wigner time delay to subunitary scattering systems. *Phys. Rev. E*, **103**:L050203, May 2021.

[208] F.H. Mies. A scattering theory of diatomic molecules. *Molecular Physics*, **41**(5):953–972, 1980.

[209] M J Seaton. Quantum defect theory I. General formulation. *Proceedings of the Physical Society*, **88**(4):801, aug 1966.

[210] M J Seaton. Quantum defect theory. *Reports on Progress in Physics*, **46**(2):167, feb 1983.

[211] M. Abramowitz and I.A. Stegun. *Handbook of mathematical functions*. Washington: National Bureau of Standards., 1964.

[212] A. C. Allison and A. Dalgarno. Continuity at the Dissociation Threshold in Molecular Absorption. *The Journal of Chemical Physics*, **55**(9):4342–4344, 1971.

[213] Allan Laslett Smith. Continuity of the Differential Oscillator Strength through a Dissociation Limit; Application to O_2 Schumann-Runge and Herzberg I Systems. *The Journal of Chemical Physics*, **55**(9):4344–4350, 1971.

[214] U. Fano. Quantum Defect Theory of l Uncoupling in H_2 as an Example of Channel-Interaction Treatment. *Phys. Rev. A*, **2**:353–365, Aug 1970.

[215] K. T. Lu. Spectroscopy and Collision Theory. The Xe Absorption Spectrum. *Phys. Rev. A*, **4**:579–596, Aug 1971.

[216] Chia-Ming Lee and K. T. Lu. Spectroscopy and Collision Theory. II. The Ar Absorption Spectrum. *Phys. Rev. A*, **8**:1241–1257, Sep 1973.

[217] U. Fano and A. R. P. Rau. *Atomic Collisions and Spectra.* Academic, Orlando, 1986.

[218] Renate Pazourek, Stefan Nagele, and Joachim Burgdörfer. Time-resolved photoemission on the attosecond scale: opportunities and challenges. *Faraday Discuss.*, **163**:353–376, 2013.

[219] Eugen Merzbacher. *Quantum mechanics.* J. Wiley, 3d ed chap. 19 edition, 1998.

[220] Thomas Young. The Bakerian Lecture. Experiments and calculations relative to physical optics. *Philosophical Transactions of the Royal Society of London*, **94**:1–16, 1804.

[221] Claus Jönsson. Elektroneninterferenzen an mehreren künstlich hergestellten Feinspalten. *Zeitschrift für Physik*, **161**(4):454–474, 8 1961.

[222] Saijoscha Heck, Meng Han, Denis Jelovina, Jia-Bao Ji, Conaill Perry, Xiaochun Gong, Robert Lucchese, Kiyoshi Ueda, and Hans Jakob Wörner. Two-Center Interference in the Photoionization Delays of Kr_2. *Phys. Rev. Lett.*, **129**:133002, Sep 2022.

[223] John W. Cooper. Photoionization from Outer Atomic Subshells. A Model Study. *Phys. Rev.*, **128**:681–693, Oct 1962.

[224] Yan V. Fyodorov and Hans-Jürgen Sommers. Statistics of resonance poles, phase shifts and time delays in quantum chaotic scattering: Random matrix approach for systems with broken time-reversal invariance. *Journal of Mathematical Physics*, **38**(4):1918–1981, 1997.

[225] Yan V. Fyodorov, Dmitry V. Savin, and Hans-Jürgen Sommers. Parametric correlations of phase shifts and statistics of time delays in quantum chaotic scattering: Crossover between unitary and orthogonal symmetries. *Phys. Rev. E*, **55**:R4857–R4860, May 1997.

[226] Savin, Dmitry V. and Fyodorov, Yan V. and Sommers, Hans-Jürgen. Reducing nonideal to ideal coupling in random matrix description of chaotic scattering: Application to the time-delay problem. *Phys. Rev. E*, **63**:035202, Feb 2001.

[227] Cohen Tannoudji Claude. *Quantum Mechanics*. Wiley-VCH.

[228] B. R. Johnson. New numerical methods applied to solving the one-dimensional eigenvalue problem. *The Journal of Chemical Physics*, **67**(9):4086–4093, 1977.

[229] Bruce W. Shore. Comparison of matrix methods applied to the radial Schrödinger eigenvalue equation: The Morse potential. *The Journal of Chemical Physics*, **59**(12):6450–6463, 1973.

[230] Roy G. Gordon. New Method for Constructing Wavefunctions for Bound States and Scattering. *The Journal of Chemical Physics*, **51**(1):14–25, 1969.

[231] Randall J. LeVeque. *Finite Difference Methods for Ordinary and Partial Differential Equations*. Society for Industrial and Applied Mathematics, 2007.

[232] Vitoriano Ruas. *Numerical Methods for Partial Differential Equations: An Introduction*. Wiley, 2016.

[233] Kevin Randles, Daniel V. Schroeder, and Bruce R. Thomas. Quantum matrix diagonalization visualized. *American Journal of Physics*, **87**(11):857–861, 2019.

[234] William H. Press, Saul A. Teukolsky, William T. Vetterling, and Brian P. Flannery. *Numerical Recipes 3rd Edition: The Art of Scientific Computing*. Cambridge University Press, USA, 3 edition, 2007.

[235] Nouredine Zettili. *Quantum Mechanics: Concepts and Applications*. Wiley, 2 edition, 2009.

[236] Cornelius Lanczos. *The Variational Principles of Mechanics*. University of Toronto Press, Toronto, 1949.

[237] B L Hammond, W A Lester, and P J Reynolds. *Monte Carlo Methods in Ab Initio Quantum Chemistry*. World Scientific, 1994.

[238] W. M. C. Foulkes, L. Mitas, R. J. Needs, and G. Rajagopal. Quantum Monte Carlo simulations of solids. *Rev. Mod. Phys.*, **73**:33–83, Jan 2001.

[239] Yiqiang Xu and Luming Zhang. Alternating direction implicit method for solving two-dimensional cubic nonlinear Schrödinger equation. *Computer Physics Communications*, **183**(5):1082–1093, 2012.

[240] Hans Van de Vyver. Comparison of some special optimized fourth-order Runge-Kutta methods for the numerical solution of the Schrödinger equation. *Computer Physics Communications*, **166**(2):109–122, 2005.

[241] Danny Bennett. Numerical Solutions to the Time-Independent 1-D Schrödinger Equation . https://www.maths.tcd.ie/~dbennett/js/schro.pdf, 2015.

[242] B. V. Noumerov. A Method of Extrapolation of Perturbations. *Monthly Notices of the Royal Astronomical Society*, **84**(8):592–602, 06 1924.

[243] Rubin H. Landau and Manuel J. Páez. *Computational Physics: Problem Solving with Computers*. Wiley-VCH ; John Wiley Distributor, 2nd rev. and enl. ed. edition, 2007.

[244] L.D. Landau and E.M. Lifshitz. *Quantum Mechanics*. Pergamon, New York, 1965.

[245] G. M. Zislin. On the nodes of eigenfunctions of the Schrödinger operator. *Uspehi Mat. Nauk*, **16**(1):149–152, 1961.

[246] Zhaoxia Pu and Eugenia Kalnay. *Numerical Weather Prediction Basics: Models, Numerical Methods, and Data Assimilation*, pages 1–31. Springer Berlin Heidelberg, Berlin, Heidelberg, 2018.

[247] J. P. Leroy and R. Wallace. Renormalized Numerov method applied to eigenvalue equations: extension to include single derivative terms and a variety of boundary conditions. *The Journal of Physical Chemistry*, **89**(10):1928–1932, 1985.

[248] L. Torop, D.G. McCoy, A.J. Blake, J. Wang, and T. Scholz. Effects of the close approach of potential curves in photoabsorption by diatomic molecules-I. Theory and computational procedures. *Journal of Quantitative Spectroscopy and Radiative Transfer*, **38**(1):9–18, 1987.

[249] Yossi Rubner, Carlo Tomasi, and Leonidas J. Guibas. The Earth Mover's Distance as a Metric for Image Retrieval. *International Journal of Computer Vision*, **40**:99–121, 2000.

[250] Matthias Wollenhaupt, Lars Englert, Alexander Horn, and Thomas Baumert. Temporal femtosecond pulse tailoring for nanoscale laser processing of wide-bandgap materials. In Jin-Joo Song, Kong-Thon Tsen, Markus Betz, and Abdulhakem Y. Elezzabi, editors, *Ultrafast Phenomena in Semiconductors and Nanostructure Materials XIV*, volume **7600**, page 76000X. International Society for Optics and Photonics, SPIE, 2010.

[251] Lars Englert, Matthias Wollenhaupt, Cristian Sarpe, Dirk Otto, and Thomas Baumert. Morphology of nanoscale structures on fused silica surfaces from interaction with temporally tailored femtosecond pulses. *Journal of Laser Applications*, **24**(4):042002, 2012.

[252] Nadine Götte, Thomas Winkler, Tamara Meinl, Thomas Kusserow, Bastian Zielinski, Cristian Sarpe, Arne Senftleben, Hartmut Hillmer, and Thomas Baumert. Temporal Airy pulses for controlled high aspect ratio nanomachining of dielectrics. *Optica*, **3**(4):389–395, Apr 2016.